Exchange Bias in Patterned Nanostructures

by

Frank Liu

B.S., Materials Science and Engineering, 2010

University of California, Berkeley

Submitted to the Department of Materials Science and Engineering in partial fulfillment of the requirements for the degree of

Doctor of Philosophy in Materials Science and Engineering

at the

MASSACHUSETTS INSTITUTE OF TECHNOLOGY

February 2016

Author: Signature redacted

Department of Materials Science And Engineering

December 11, 2015

Certifed by: Signature redacted

Caroline Ross

Professor of Materials Science and Engineering

Thesis Supervisor

Accepted by: Signature redacted

Donald Sadoway

Chair, Departmental Committee on Graduate Students

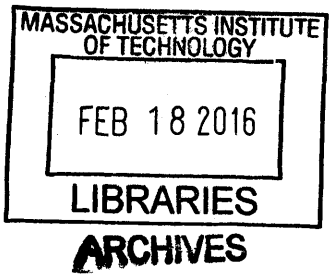

Exchange Bias in Patterned Nanostructures

by

Frank Liu

Submitted to the Department of Materials Science and Engineering on December 11, 2015, in partial fulfillment of the requirements for the degree of Doctor of Philosophy in Materials Science and Engineering

Abstract

Exchange bias between a ferromagnet (FM) and antiferromagnet (AFM), which is utilized to pin the magnetization of a FM into a fixed direction in space, is essential in commonly used electronic components such as magnetic recording heads and magnetic memory cells, as well as novel magnetic logic and memory devices. However, the exchange bias effect has been optimized in materials and used in devices for decades without a good scientific understanding, both due to lack of nanoscale research and conflicted results from differences in fabrication and feature size. In this thesis, we present a special fabrication method that produces exchange bias reliably and consistently. We also show the results of both experimental and simulated investigation of the properties of exchange biased nanostructures such as domain formation, magnetostatic interactions, and response to field-driven switching.

·A fabrication method for creating locally exchange biased nanostructures is first developed. By etching back a predeposited FM film, and regrowing a thin FM layer and then the AFM film, this hybrid method combines the benefits of a clean interface produced using subtractive methods and the scalability produced using additive methods. Its consistency is analyzed through vibrating sample magnetometry (VSM) and scanning electron microscopy (SEM).

Next, the fabrication method is applied to an array of nanodots with varying ion beam etch durations and dot diameters, demonstrating a reduced exchange bias for small diameters, and no significant change in exchange bias unless the ion beam etch duration exceeded 30s. Based on the consistency of this method, new device-like patterns were fabricated both experimentally and by modeling, in which a grating of AFM stripes was exchange biased with a continuous FM film. Competing magnetic interactions were found in the modeling, and produced extraordinary hysteresis loop shapes in the experimental samples. Next, a grating of AFM stripes was exchange biased with a 90° offset grating of FM stripes using the same fabrication method, which simulates an array of individual magnetic devices. A different set of competing magnetic interactions was found, and the feature sizes of the FM and AFM components were demonstrated to tune these interactions and thus the switching behavior of such devices.

Exchange bias of materials with perpendicular magnetic anisotropy (PMA) was attempted by exchange coupling a PMA FM material with an in-plane FM material, which in turn exchange couples with the AFM material. However, the magnitude of the exchange bias was found to be negligible when compared to the coercivity of the PMA material

Thesis Supervisor: Caroline A. Ross
Title: Professor of Materials Science and Engineering

Table of Contents

Chapter 1 Introduction **19**

1.1 Overview and Motivation.....19

1.2 Outline of the Thesis.....22

1.3 Background.....23

1.3.1 Exchange Bias: Phenomenology, and Key Terms.....23

1.3.1.1 Phenomenology: The Intuitive Picture.....23

1.3.1.2 Key Terms and Relations.....24

1.3.2 Magnetic Domains.....29

1.3.3 Interfacial Spins.....30

1.3.4 Models of Exchange Bias.....31

1.4 Exchange Bias in Nanostructured Systems.....36

1.4.1 Fabrication Methods for Optimizing Exchange Bias.....36

1.4.2 Size Effects on Exchange Bias.....38

1.4.2.1 Equal Patterning on FM and AFM.....39

1.4.2.2 Partial Exchange Bias.....40

1.4.2.3 Training Effect and Blocking Temperature.....42

Chapter 2 Experimental and Modelling Methods **44**

2.1 Fabrication.....44

2.1.1 Interference Lithography.....44

2.1.2 Electron Beam Lithography.....47

2.1.3 Deposition.....47

2.1.3.1 DC Magnetron Sputtering.....47

2.1.3.2 Ion Beam Etching.....49

2.1.3.3 Electron Beam Evaporation.....49

2.1.4 Liftoff.....50

2.1.5 Setting Exchange Bias.....51

2.1.6 Hybrid Fabrication Method for Partial Exchange Bias.....52

2.2 Characterization.....54

2.2.1 SEM.....54

2.2.2 VSM.....55

2.2.3 AFM and MFM.....56

2.3 Micromagnetic Simulation.....57

Chapter 3 Arrays of Exchange Biased Nanodots **59**

3.1 The IrMn / $Ni_{80}Fe_{20}$ System.....60

3.2 Effect of Ion Beam Etching on Magnetic Properties.....62

3.3 Effect of Dot Diameter on Exchange Bias.....67

3.3.1 Domain Size.....68

3.3.2 Vortex States.....69

3.3.3 Training Effect and Blocking Temperature.....70

3.4 Summary....72

Chapter 4 AFM Stripe Grating on Continuous FM Film 74

4.1 Exchange Bias Parallel to Grating....75

4.1.1 Experimental Results....76

4.1.1.1 Competing Effects of Feature Size on Exchange Bias....78

4.1.2 Micromagnetic Simulation....79

4.1.2.1 Switching Behavior: Competing Magnetic Interactions....82

4.2 Exchange Bias Perpendicular to Grating....85

4.2.1 Experimental Results....85

4.2.2 Micromagnetic Simulation....87

4.3 Summary....88

Chapter 5 The Double Grating Structure 90

5.1 Fabrication....91

5.2 Experimental Results....92

5.2.1 Exchange Bias Trends....95

5.3 Micromagnetic Simulation....97

5.4 Exchange Bias with Perpendicular Magnetic Anisotropy....102

5.4.1 Interactions between a PMA FM and an IMA FM....102

5.4.1.1 Exchange Bias in CoCrPt / NiFe / IrMn....105

5.5 Summary....107

Chapter 6 Summary, Conclusions, Device Applications, and Future Work **109**

6.1 Summary and Conclusions of Key Results.....109

6.2 Future Works.....112

6.2.1 Experimental Demonstration of a PMA Exchange Bias System.....113

6.2.2 Creating and Pinning Domain Walls Using Exchange Bias.....114

6.2.2.1 Application to Domain Wall Logic Devices.....114

6.2.2.2 Application to Pinning Sites in Magnetic Storage.....116

References **119**

Appendix A Spintronics: Bi_2Se_3 Surface States Near YIG **128**

A.1 Micromagnetic Simulations of YIG.....129

Appendix B Cleaner Liftoff Using a Modified Trilayer Resist **131**

B.1 PMMA Underneath ARC.....131

List of Figures

Fig. 1.1 Different stages of the exchange biased hysteresis loop [12].....24

Fig. 1.2 Exchange bias and coercivity versus AFM thickness for the NiFe/FeMn system [25] 26

Fig. 1.3 Schematic showing that surface roughness can cause a reduced number of spins to pin the FM spin in one direction 26

Fig. 1.4 Coercive fields along the ascending and descending branches of the hysteresis loop as a function of the number of consecutive measurements for a NiFe/FeNiMn bilayer [32] 28

Fig. 1.5 Schematic of the AFM-FM thin film bilayer, and XMCD and XMLD microscopy images, showing that the domain structure of the AFM controls the domain structure of the FM [34].....29

Fig. 1.6 Schematic for compensated and uncompensated AFM surface spins [22].....31

Fig. 1.7 Diagram of the parameters and angles involved in the intuitive model of exchange bias. The AFM sublattice magnetization M_{AFM} has two opposite Directions [22] 33

Fig. 1.8 A schematic depicting the Mauri-Siegmann model of exchange bias [43] 35

Fig. 1.9 Schematic of a subtractive method of fabrication for exchange biased nanostructures. A pattern is made using photolithography on top of a continuous bilayer film. The Ta layer is etched away, and oxide is introduced into the exposed IrMn by annealing [50] 37

Fig. 1.10 Schematic of an additive fabrication method, using a porous alumina mask to selectively deposit Fe dots, along with SEM images [51].....38

Fig. 1.11 Schematic of a structure in which the FM and AFM are patterned equally [12]. SEM image of an example of such a structure containing IrMn-CoFe nanodots [63] and Ni-NiO lines [22].....40

Fig. 1.12 Complex asymmetrical hysteresis loops generated from two magnetically different regions interacting [49].....41

Fig. 2.1 Schematic of the Lloyd's Mirror interference lithography system, along with photograph of the Lloyd's Mirror [69] 45

Fig. 2.2 MATLAB output graph of reflectivity versus ARC thickness [69] 46

Fig. 2.3 A schematic of a DC magnetron sputtering system [70] 48

Fig. 2.4 A schematic of an electron beam evaporation setup [71] 50

Fig. 2.5 Schematic of the two-step hybrid fabrication procedure. A high-quality interface is produced by back etch and redeposition 53

Fig. 2.6 A comparison of hysteresis loops of a continuously-grown NiFe film and a NiFe film grown using the etch and redeposition procedure. Similarities indicate that 3 seconds of ion beam etching has little effect on the magnetic properties.....54

Fig. 2.7 Schematic of a VSM setup [72].....56

Fig. 3.1 Schematic of method used to make nanodots samples, and SEM images of the resist mask and finished sample.....60

Fig. 3.2 Variation of magnetocrystalline anisotropy and magnetostriction coefficients

with Ni content by % weight in FCC NiFe alloys. [30] 61

Fig. 3.3 Optical microscope images showing oxidation-induced stacking faults in samples that were etched with Argon ion milling [45].....63

Fig. 3.4 Coercivity, exchange bias, and thickness versus NiFe ion beam etching duration for an unpatterned film and for an array of 100 nm dots.....64

Fig. 3.5 A comparison between hysteresis loops of 120 nm diameter dots and that of continuous films under different durations of ion beam etch time.....66

Fig. 3.6 Exchange bias versus ion beam etch time for NiFe/IrMn dots of various diameters...67

Fig. 3.7 Exchange bias versus dot diameter for NiFe/IrMn dots subject to different ion beam etch times.....68

Fig. 3.8 Hysteresis loop of an array of unbiased 400 nm dots and exchange biased 300 nm dots. The shape of both loops is characteristic of reversal via a vortex state.....70

Fig. 3.9 Training effect in 100 nm diameter dots made in a one-step process with no ion beam etching. There is no visible training effect in the continuous bilayer film.....71

Fig. 4.1 Schematic and SEM images of the fabrication procedure used to create AFM stripes on top of continuous FM.....75

Fig. 4.2 Experimental phase diagram of the switching behavior, with examples of one-step loops and two-step loops.....77

Fig. 4.3 Measured exchange bias and coercivity versus IrMn stripe width w for four different values of s 79

Fig. 4.4 Schematic of the unit cell for the micromagnetic simulation.....80

Fig. 4.5 Phase diagram for switching behavior of the patterned structure with both exchange bias and applied field parallel to the stripe length, along with example one-step and two-step loops 81

Fig. 4.6 OOMMF micromagnetic images under fields corresponding to Fig. 4.5(c) 83

Fig. 4.7 OOMMF micromagnetic images corresponding to Fig. 4.5(d) at -90 Oe and -45 Oe 83

Fig. 4.8 The values of w for s = 200 nm at the transition T_1 as a function of exchange bias magnitude 84

Fig. 4.9 Experimental phase diagram of the switching behavior in the samples exchange biased and measured perpendicular to the IrMn stripe length, along with examples of one-step and two-step loops 86

Fig. 4.10 Phase diagram for switching behavior of the patterned structure with exchange bias in plane, perpendicular to the wire length. Magnetic configurations just after the switch, along with an intermediate dynamic state.....88

Fig. 5.1 Schematic of the sample fabrication procedure for the double grating structure, along with SEM images of a single grating and a double grating.....91

Fig. 5.2 Experimental map of the switching behavior under various w and s, and example hysteresis loops showing one-step switching and two-step switching.....94

Fig. 5.3 Remanence loop for s = w = 200 nm. High remanence indicates that reversal is mostly irreversible, as opposed to having reversible tilt. Minor loop for a two-step switch with s = w = 500 nm, confirming that reversal is irreversible.....95

Fig. 5.4 Measured exchange bias and coercivity versus IrMn wire width and NiFe wire

width 97

Fig. 5.5 Schematic of the simulation, switching behavior phase map, and location of phase boundary T_1 as a function of simulation exchange bias for w = s 99

Fig. 5.6 Hysteresis loops of one-step switching and of two-step switching with micromagnetic images during the switch.....101

Fig. 5.7 Progression of the two-step switching plateau as dimensions increase 101

Fig. 5.8 Schematic of the exchange-coupled multilayer structure consisting of in-plane NiFe and perpendicular $[Co/Pd]_5$ [92] 103

Fig. 5.9 Micromagnetic simulation of a $[Co/Pd]_5$ /NiFe(x nm) multilayer for various NiFe thicknesses [92].....104

Fig. 5.10 Saturation magnetization versus temperature for CoCrPt. At 520 K, CoCrPt maintains a magnetization of 75 emu cm^{-3}.....105

Fig. 5.11 Hysteresis loop of a continuous film of Ti (10 nm) / CoCrPt (10 nm).....106

Fig. 5.12 Hysteresis loops of a Ti(10 nm)/CoCrPt(10 nm)/IrMn(10 nm) film and a Ti(10 nm)/CoCrPt(10 nm)/NiFe (2 nm)/IrMn(10 nm) film.....107

Fig. 6.1 Schematic and electron beam lithography write pattern of a horseshoe structure with exchange biased ends, used to trap domain walls.....115

Fig. 6.2 Schematic of the domain wall device. An MTJ reads the magnetization state of the FM [24].....116

Fig. 6.3 Schematic of a racetrack memory device [95].....117

Fig. 6.4 Illustration of how the energy landscape may look like for a domain wall if weak exchange bias regions were introduced on into a domain wall device,

creating pinned regions for the domain wall.....118

Fig. A.1 STEM image and schematic of Bi_2Se_3/YIG/GGG [96].....129

Fig. A.2 Polar MOKE measurements of YIG [96] and corresponding hysteresis loop and micromagnetic images generated using OOMMF, showing agreement.....130

Fig. B.1 Schematic of sample fabrication using the modified trilayer resist stack. PMMA dissolves readily during liftoff, unlike ARC.....132

Fig. B.2 SEM images of the trilayer and quadlayer resist masks after RIE, along with the final sample after liftoff.....132

List of Tables

Table 1.1 Néel temperatures of several common oxide and metallic AFMs.....21

Table 2.1 Materials parameters for Permalloy and YIG.....58

Chapter 1

Introduction

1.1 Overview and Motivation

In 1956, Meiklejohn and Bean observed that when partially oxidized Co particles were annealed, then cooled through the Néel temperature of the oxide, a unidirectional anisotropy was induced in the Co, and the particles exhibited hysteresis loops displaced along the magnetic field axis [1]. This unidirectional anisotropy is exchange bias and is one of the phenomena resulting from exchange coupling at the interface between a ferromagnetic (FM) and antiferromagnetic (AFM) material.

Since then, exchange bias was observed in many other systems containing FM-AFM interfaces, including small particles [2, 3, 4], inhomogeneous materials [5, 6], and thin films [7, 8]. In particular, exchange bias in thin films have found their way into many common magnetic devices today, including domain state stabilizers in anisotropic magnetoresistance (AMR) disk drive recording heads [9], pinned reference layers in spin valve readback heads [10], and more recently, devices such as MRAMs that use giant magnetoresistance (GMR) in exchange biased systems [11]. Thin films attracted much research due to a number of desirable properties compared to other structures:

1. A greater number of different FM-AFM thin film combinations were available. This was because in the case of fine particles, the AFM choice was typically limited to a reacted shell resulting from chemical treatment of the surface, for example, by oxidation.
2. Greater control of the FM-AFM interface. The grain size, orientation, crystalline quality, microstructure, and interface could all be controlled in thin films.
3. The demonstration of exchange bias in spin valve devices [12, 13] has sparked much interest in further thin film research.

There have been a wide variety of AFM materials used. After the discovery and early works on oxidized FM particles, much of the early research on thin films involved a number of thin film oxides of common FMs such as NiO, CoO, CoNiO, FeO, etc. [13, 14, 15]. However, in 1964, the first fully metallic exchange bias thin film system was reported [16], and since then, metallic bilayers have been one of the most studied and most applied exchange bias systems; in particular, systems with FeMn [17, 18], which was used in most exchange biased GMR spin valves [19]. However, other metallic systems with more desirable properties [20, 21], which will be summarized below, surfaced and have gained interest.

There are several criteria for an AFM to be interesting from a magnetic device point of view:

1. The AFM should have a high Néel temperature. At the very least, the Néel temperature should be above room temperature, and preferably much higher because devices can potentially heat up. Table 1.1 summarizes the Néel temperatures of several commonly used AFMs [22].
2. The AFM should have a large magnetocrystalline anisotropy to resist switching along with the FM. In general, if the AFM has a large magnetocrystalline anisotropy, the exchange bias is large.

3. Good chemical and structural compatibility with the most common and important FM films; for example, NiFe and Co.

Based on the criteria above, some of the most common oxide AFMs used in study and application include NiO and CoO for good compatibility with Ni and Co respectively, and high exchange bias values. However, the Néel temperature of CoO is rather low, as seen in Table 1.1. For metallic AFMs, the commonly used thin films include rocksalt structures like FeMn and IrMn, which satisfy all three of the above criteria.

AFM	Néel Temperature (K)
NiO	520
CoO	290
FeO	200
FeNiO	200-520
FeMn	490
NiMn	1070
IrMn	690

Table 1.1: Néel temperatures of several common oxide and metallic AFMs

Most of the proposed applications of exchange bias are in thin film form, as mentioned above. In magnetic recording media, exchange bias is locally introduced via selective annealing, selective ion bombardment, or patterning [23]. In recording heads based on AMR, an AFM layer is deposited on the edges of the FM, which reduces the noise of these devices by eliminating closure domains [20]. In GMR spin-valve devices, one of the two FM layers is exchange coupled with an AFM layer. This FM has a shifted hysteresis loop, whereas the other FM has a normal loop, and as a result, there is a field range in which the FM layers have antiparallel magnetizations, and the resistance is high [11]. More recently, there have been novel proposed magnetic storage and logic devices that make use of exchange bias to pin domain walls [24]. However, despite the importance of exchange bias thin films in commonly used magnetic devices, for many years, exchange bias

has just been optimized and used without a solid scientific understanding. Even though magnetic behavior of nanoscale exchange bias systems have been studied to some extent, we will show in sections 4 and 5 that there are interactions on the nanoscale that have not yet been extensively investigated. Some important structures are even completely unexplored. Because the scaling of devices and device density is an important technological goal, the exchange bias of patterned nanostructures is not only a scientific interest, but also an essential component for enabling the next generation of denser magnetic media.

1.2 Outline of the Thesis

Chapter 1 provides a motivation for nanoscale exchange bias and presents a brief overview of the history and phenomenology of exchange bias. Both the scientific and technological impact of scaling down exchange bias are addressed. Chapter 2 describes the experimental and modeling methods used during this study. Chapter 3 summarizes a study on the effects of feature size and etch duration on patterned nanodots using a special hybrid fabrication method that we developed. Chapter 4 extends the study over to a partially exchange biased system and explores the magnetic interaction between two magnetically different regions. Chapter 5 discusses an exchange biased array of device-like systems and the effects of various driving forces that influence switching behavior. Exchange bias in PMA materials and more complicated patterns is also investigated. Chapter 6 summarizes major results, describes ongoing projects, and suggests future work. Appendix A describes a micromagnetic modeling project not related to exchange bias, done in collaboration with other research groups from MIT, UCLA, and Zhejiang University, and Appendix B presents a special fabrication procedure that enables cleaner SEM images of samples, but does not alter magnetic properties.

1.3 Background

First, an intuitive description of exchange bias is given, and key terms, parameters, and factors influencing exchange bias are summarized. Then, a discussion of magnetic domains and interfacial spins, and how they play a role in exchange bias is provided. Lastly, useful models of exchange bias are discussed.

1.3.1 Exchange Bias: Phenomenology, and Key Terms

1.3.1.1 Phenomenology: The Intuitive Picture

The loop shift associated with exchange bias can be understood qualitatively by assuming that the AFM and the FM exchange couple at the interface. If a magnetic field is applied above the Néel temperature of the AFM, but below the Curie temperature of the FM, the AFM spins are oriented randomly, while the FM spins line up with the applied field, as shown in Fig. 1.1(a). As the bilayer is cooled below the Néel temperature with the applied field in place, the AFM interfacial spins couple with the FM interfacial spins and align themselves ferromagnetically. The subsequent layers in the bulk AFM "follow" the AFM order and align themselves antiparallel based on the interfacial layer [Fig. 1.1(b)]. When the field is reversed, the FM spins begin rotating. However, the AFM spins do not rotate, and due to the exchange coupling at the interface, the FM spins align preferentially with the AFM spins to keep them in their original position, resulting in a larger field required to switch the FM [Fig. 1.1(c)]. Once the reversal of the FM does occur, however, the AFM spins still remain unchanged if the anisotropy of the AFM is large enough [Fig. 1.1(d)]. Once the field is switched back to its original direction, the FM spins begin reversing at a smaller field because of the exchange coupling with the AFM spins, which now exert a microscopic torque towards the original direction [Fig. 1.1(e)], resulting in a shifted hysteresis loop.

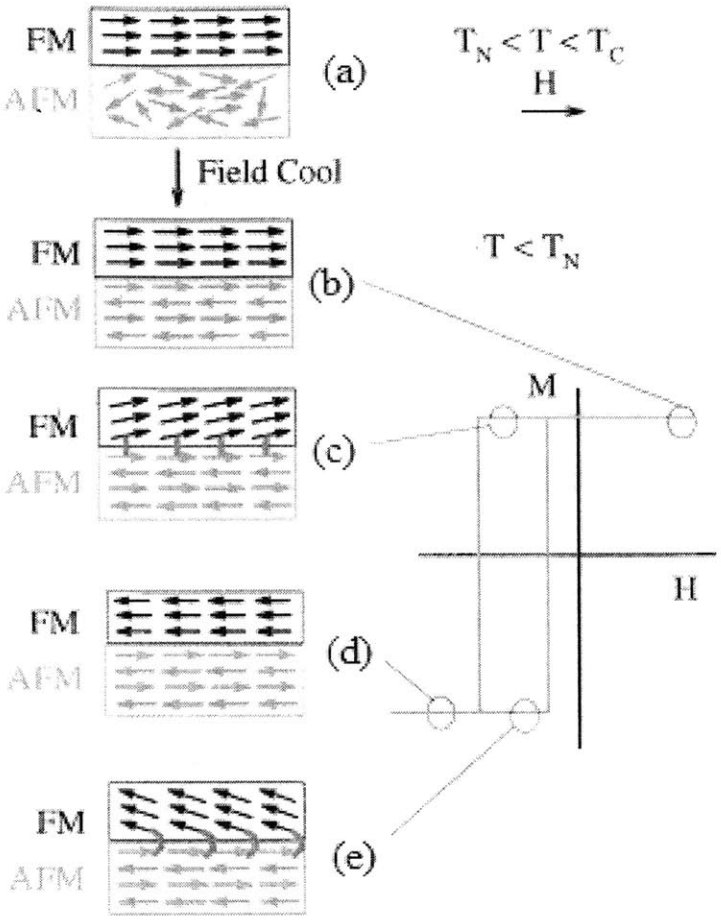

Figure 1.1: (a) FM-AFM bilayer during annealing. The spins in the AFM are random, whereas that of the FM are aligned with the applied field. (b)-(e) Different stages of the exchange biased hysteresis loop. Figure adapted from [12].

1.3.1.2 Key Terms and Relations

The $1/t_{FM}$ Relation

For all FM-AFM systems, it has been reported that exchange bias increases as the thickness of the FM film decreases, in an inverse relationship $H_{EB} \propto 1/t_{FM}$, where H_{EB} is the exchange bias field, and t_{FM} is the FM layer thickness. This makes intuitive sense, as exchange bias is an interface phenomenon [25]. However, if the FM becomes too thin, as will be discussed in chapter 3, the relation no longer holds, probably because the FM layer becomes discontinuous.

The inverse relation can be derived from many common exchange bias models, and an analysis for both the intuitive model presented in section 1.3.1.1 and a more complicated model will be given in section 1.3.4.

AFM Thickness

The relationship between exchange bias and AFM thickness is less intuitive. In continuous films, exchange bias appears to decrease as AFM thickness is decreased, but only for a certain thickness range that depends on the material, microstructure, and temperature. At a thickness greater than this range, exchange bias is independent on AFM thickness, as shown in Fig. 1.2. There are many possible causes for this. Firstly, the Néel temperature of the AFM depends on thickness. Secondly, the AFM domain structure could affect exchange bias if the thickness decreases to the AFM domain wall size. Finally, as will be derived in an analysis of the intuitive model (section 1.3.4), for exchange bias to occur, the condition $K_{AFM}t_{AFM} \geq J_{FM-AFM}$ must be met, where J_{FM-AFM} is the interfacial exchange coupling constant. Lowering the thickness of the AFM will eventually violate this condition.

Because the relationship between exchange bias and AFM thickness relies so heavily on the structure of the AFM, there are many exceptions to the general trend. For example, if the stable orientation changes with thickness, a change in exchange bias for large AFM thicknesses may be observed [25]. In addition, if the AFM domain structure changes at very low thicknesses, the trend may also be broken [26].

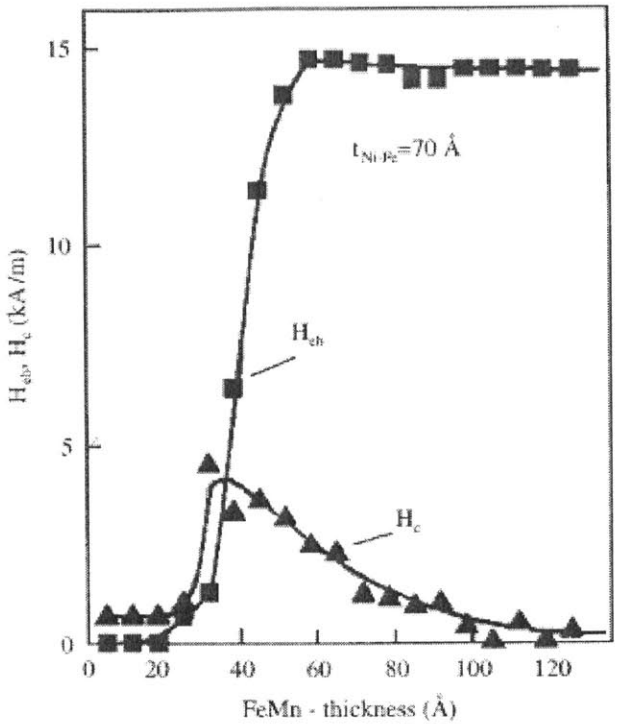

Figure 1.2: Exchange bias (squares) and coercivity (triangles) versus AFM thickness for the NiFe/FeMn system. Figure from [25].

Roughness

Most studies on interface roughness agree that exchange bias weakens with increasing roughness [27, 28], and our study on rough surfaces induced by ion beam etching in chapter 3 supports this. Based on the intuitive model presented in section 1.3.1.1, surface roughness reduces the total number of spins pinning the FM in one direction, as shown in Fig. 1.3. The more surface roughness is introduced, the weaker the exchange bias becomes.

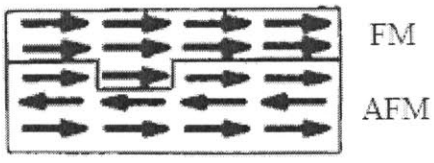

Figure 1.3: Schematic showing that surface roughness can cause a reduced number of spins to pin the FM spin in one direction.

Blocking Temperature

The blocking temperature, T_B, is the temperature above which exchange bias vanishes. T_B always has a maximum equal to the Néel temperature of the AFM; however, in some cases, such as for IrMn, the blocking temperature T_B is much lower than the Néel temperature of the bulk AFM, whereas in other cases, such as for CoO, $T_B \approx T_N$. The cause appears to be related to the grain size of the AFM layer [22], as systems with single crystal or large AFM grains tend to have $T_B \approx T_N$, whereas systems with small grains or very thin films have $T_B < T_N$. In addition, the blocking temperature seems to also depend on the lateral size of the exchange biased structures. It has been reported [29] that the blocking temperature of nanoscale structures show a blocking temperature of up to 30 K lower than that of a continuous film. Similarly, the Néel temperature of AFMs also tend to decrease with size reduction [30], suggesting that temperature effects feature more prominently in nanostructures than in continuous films.

Coercivity

Coercivity measures how big of a magnetic field can be applied to a material before demagnetization occurs and is typically measured as the half width of a hysteresis loop at zero magnetic moment. The hysteresis loop shift in exchange biased systems is often accompanied by an increase in coercivity. However, unlike the bias field, the coercive field is not often studied. Among the systems for which coercivity has been investigated, it was found that coercivity usually increases below the blocking temperature. This was attributed to AFM anisotropy, as AFMs with smaller anisotropy showed larger increases in coercivity [31]. We can use the intuitive model of exchange bias to understand why this is the case. If the AFM has a small magnetocrystalline anisotropy, the AFM spins are twisted irreversibly when the FM reverses, increasing the coercivity

of the FM [22]. On the other hand, if the AFM has a large anisotropy, its spins will not move, and the FM spins are forced to decouple in order to reverse, and the coercivity is reduced.

Training Effect

The training effect is a well-known phenomenon in which the exchange bias magnitude depends on the number of measurements performed. For example, if several hysteresis loops were measured without resetting the exchange bias by field annealing, the measured exchange bias field will decrease according to $H_{EB} - H_{EB\infty} \propto 1/\sqrt{n}$, where n is the number of consecutive loops measured, and $H_{EB\infty}$ represents the exchange bias field after an infinite number of measurements. The coercive field also changes with number of consecutive loops, as shown in Fig. 1.4 [32]. The origin of the training effect is believed to be the reorientation of AFM domains towards energetically favorable configurations each time the FM reverses [32].

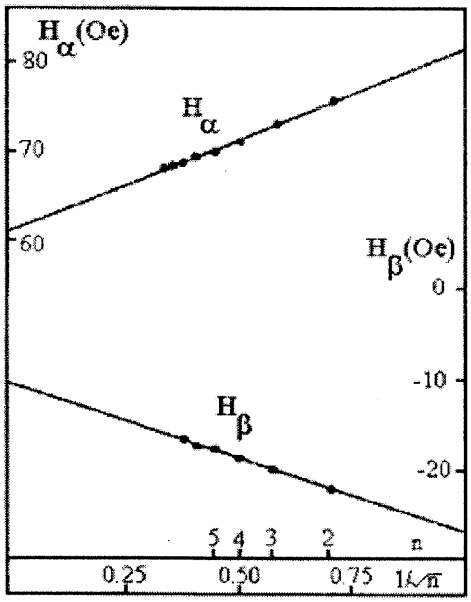

Figure 1.4: Coercive fields along the ascending branch of the hysteresis loop, H_α, and descending branch, H_β, as a function of the number of consecutive measurements for a NiFe/FeNiMn bilayer. Figure from [32].

1.3.2 Magnetic Domains

Until recently, little was known about the domain structure of AFMs in thin films. The AFM domain structure in bulk single crystals was studied via neutron diffraction and x-ray diffraction [33]. However, the typical domain size in well-annealed bulk AFMs was in the 0.1 – 1 mm range, whereas in epitaxial thin films, the domain size could be less than 50 nm—well below the resolution of neutron diffraction and x-ray diffraction [33]. Recently, x-ray polarization control allowed AFM domains to be viewed by means of x-ray magnetic linear dichroism (XMLD), and x-ray magnetic circular dichroism (XMCD) on FMs. The advent of these techniques confirmed long-standing theories, and brought along new insight about the role of the AFM domains.

It is generally accepted in all models of exchange bias that during exchange coupling, the magnetically neutral AFM "talks to" the FM, conforming its anisotropy to that of the FM. From the XMCD and XMLD images shown in Fig. 1.5, it is clear that the AFM domain structure determines the FM domain structure on top of it [34]. The inset suggests that the FM moments are also aligned along the AFM axis.

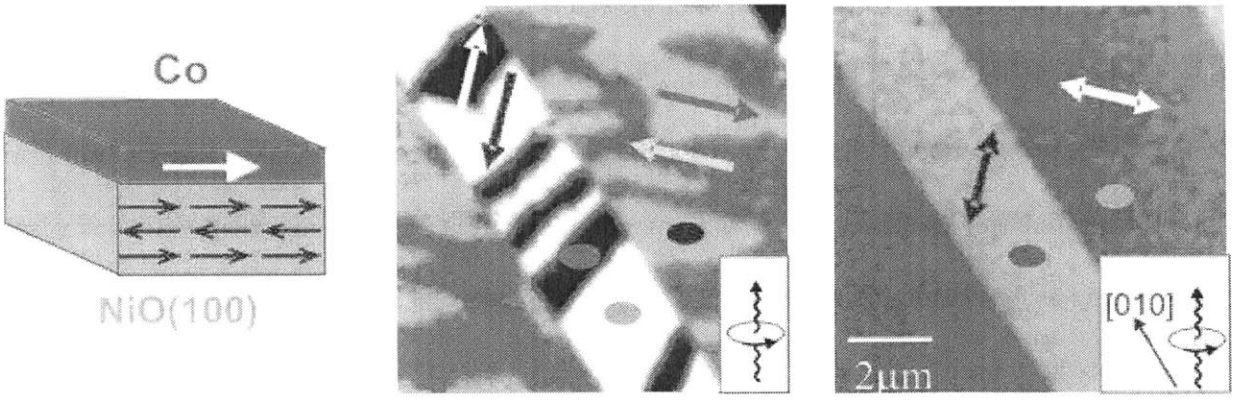

Figure 1.5: Left: Schematic of the AFM-FM thin film bilayer. Right: XMCD and XMLD microscopy images, showing that the domain structure of the AFM controls the domain structure of the FM [34].

XMCD and XMLD also provide insight to the relationship between exchange bias and AFM domain size. It was predicted by Malozemoff [26] using the random field model and statistical treatment of AFM domain size that the exchange bias field should increase as the AFM domain size decreases, $H_{EB} \sim 1/d$. Afterwards, experiments would try to support Malozemoff's prediction by assuming that the grain size in the AFM was equal to the domain size. The assumptions were confirmed when AFM domains were directly imaged using XMLD microscopy, and the *1/d* relationship was solidified.

1.3.3 Interfacial Spins

It is well known that exchange bias is an interface phenomenon, and that the coupling of the spins at the FM-AFM interface govern exchange bias. AFM spins can be categorized into two spin types: compensated and uncompensated. In a compensated AFM, the net spin averaged over a microscopic region is zero, and both AFM spin sublattices are present at the interface. In contrast, in an uncompensated AFM, the spins are arranged such that the surface magnetization is non-zero, and only one AFM spin sublattice is present at the interface, as shown schematically in Fig. 1.6. It has been suggested by many [35, 36, 37] that uncompensated spins play a key role in exchange bias. However, simple models of exchange bias that assumed a direct relationship between number of uncompensated spins and exchange bias magnitude estimated exchange bias values several orders of magnitude larger than that found in experiments. The microscopic origins of this remained a mystery until recently.

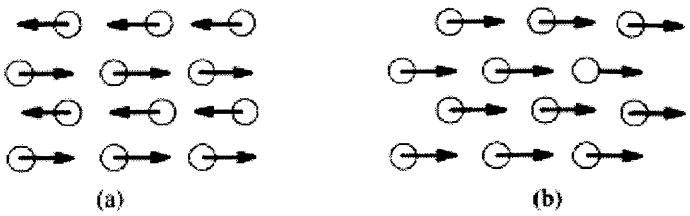

Figure 1.6: Schematic for (a) compensated and (b) uncompensated AFM surface spins [22]

X-ray measurements in the early 2000s showed that not all uncompensated spins contribute towards exchange bias in the same way [38]. In fact, element-specific XMCD analysis showed that only 60% of a monolayer at the interface of Mn are uncompensated, and among those, only 7% are pinned. Thus, the vast majority of the uncompensated interfacial spins contribute towards coercivity [38], while only 4% of the interfacial uncompensated spins are pinned and contribute towards exchange bias. There is one exception, however. In AFM single crystals coated with a thin layer of FM, there seems to be very little dependence of the exchange bias on the type of spin configuration present at the AFM interface [39]. The exact origin is currently unknown, but it has been suggested that reorientation of the spins at the interface or the formation of magnetic domains in the AFM could be the cause [22].

1.3.4 Models of Exchange Bias

There are many models of exchange bias, including macroscopic models that do not take into account the lateral structure of the AFM and FM layers (for example, the intuitive exchange bias model proposed by Meiklejohn and Bean [1, 2]), mesoscopic models that consider differences in the spin configuration in the x-y plane (for example, Malozemoff's random field model [26]), and microscopic models that calculate the detailed spin configuration of every atom or group of atoms in the volume, in all dimensions (for example, micromagnetic simulations or Monte Carlo simulations [40]). However, in this section, only the intuitive model will be discussed in detail to

further understand the phenomenology of exchange bias introduced in section 1.3.1, and the Mauri-Siegmann mesoscopic model, which shows excellent agreement with experimental results.

Intuitive Model of Exchange Bias

Meiklejohn and Bean's intuitive model of exchange bias was introduced in section 1.3.1 to explain the origin of exchange bias. The main assumptions of the model are that the FM and AFM have parallel easy axes, and that rotation of moments is coherent. Fig. 1.7 contains a simple diagram that shows the applied field direction relative to the magnetization direction, the AFM sublattice magnetization, and the anisotropy axes, as well as the relevant parameters. The energy per unit area is given by:

$$E = -HM_{FM}t_{FM}\,cos(\theta - \beta) + K_{FM}t_{FM}sin^2(\beta) + K_{AFM}t_{AFM}sin^2(\alpha) - J_{FM-AFM}cos(\beta - \alpha)$$

where H is the applied field, M_{FM} is the saturation magnetization of the FM, t_{FM} is the thickness of the FM layer, t_{AFM} is the thickness of the AFM layer, K_{FM} and K_{AFM} are the anisotropies of the FM and AFM layer respectively, J_{FM-AFM} is the interface exchange coupling constant, β is the angle between the magnetization and the FM easy axis, α is the angle between the AFM sublattice magnetization and the AFM easy axis, and θ is the angle between the applied field and the easy axes.

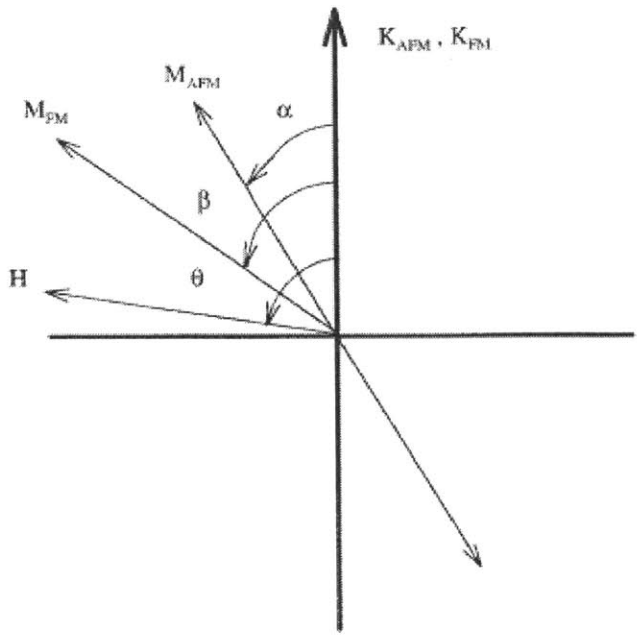

Figure 1.7: Diagram of the parameters and angles involved in the intuitive model of exchange bias. The AFM sublattice magnetization M_{AFM} has two opposite directions. Figure from [22].

The first term in the equation accounts for the effect of the applied field on the FM, the second term accounts for the effect on the AFM, the third term accounts for the AFM anisotropy, and the last term accounts for interface coupling. However, this model does not take into account domains and ferromagnetic coupling at the interface [1].

In the case of NiFe, which was used throughout most of chapters 3, 4, and 5, the FM anisotropy is negligible and the second term drops out. If the energy is minimized with respect to α and β, the exchange bias is calculated to be $H_E = J_{FM-AFM}/(M_{FM}t_{FM})$. This is one of the derivations of the famous $1/t_{FM}$ relation.

In the extreme case that $K_{AFM}t_{AFM} \ll J_{FM-AFM}$, it is energetically favorable for $\alpha \approx \beta$. In other words, the AFM and FM spins rotate together, and if the AFM spins follow the FM spins during reversal, there is only an increase in coercivity without any loop shift. Therefore, based on the model, the AFM should have a high magnetocrystalline anisotropy and thickness, which is

confirmed by experiments [41, 22, 12]. However, there are problems with the intuitive model, the biggest of which is the exchange bias magnitude, predicting exchange bias to be several orders of magnitude larger than the experimental results [22]. Mesoscopic models that account for inhomogeneities in the x-y plane give a more accurate picture.

Mauri-Siegmann Model

Arguably the simplest model that accounts for the domain and interfacial spin observations mentioned in sections 1.3.2 and 1.3.3 is the Mauri-Siegmann model, shown in Fig. 1.8 [42]. According to the model, the AFM spins in the bulk favors alignment towards the magnetocrystalline anisotropy direction in the bulk AFM, labeled x in the figure. The interface depicted in the figure represents an uncompensated spin that is aligned parallel to the AFM spin axis at the interface and has a thickness of ξ. The FM layer on top is exchange coupled parallel to the interface spin. A fraction of the interfacial spins are pinned, which means they are anchored in the bulk of the AFM [42]. A magnetic field H is applied at an angle β with respect to the AFM axis x, and as a result, the spins in the FM will align along H. If the AFM has a high anisotropy, then the axis x will not be twisted, and exchange bias is maximized. However, if the AFM is soft, then the AFM axis will rotate and a domain wall will form in the AFM—in other words, at the interface, the uncompensated AFM spin will align along the AFM axis, but will twist until they are parallel to x in the bulk, and exchange bias is decreased.

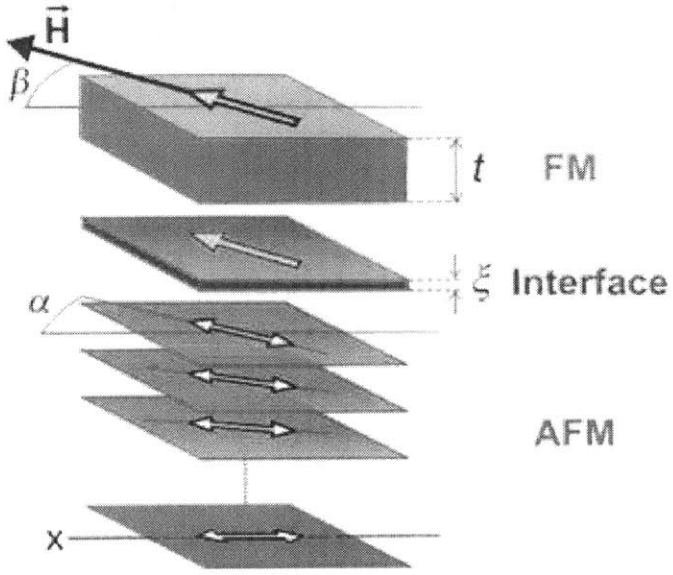

Figure 1.8: A schematic depicting the Mauri-Siegmann model of exchange bias. The uniaxial anisotropy of the AFM is along x. The interface contains an uncompensated interfacial moment and exhibits parallel coupling with the FM moments above. The applied field H makes an angle β with respect to x. As a result, FM moments are aligned parallel to H, and depending on the magnetocrystalline anisotropy of the AFM, the AFM axis may rotate and form a domain wall. [43]

In this model, the pinned interfacial moment density is given by $S_{AFM}/(\zeta a)$, where S_{AFM} is the magnitude of the pinned interfacial spins in the AFM, ζ is the interface thickness, as shown in Fig. 1.8, and a is the in-plane atomic separation. Then, the interfacial coupling energy density is given by $E_{FM-AFM} = J_{FM-AFM}S_{AFM}S_{FM}/(\zeta a)$, where S_{FM} is the magnitude of the spins in the FM, and J_{FM-AFM} is the interfacial exchange coupling constant [42]. If the domain wall energy, E_{DW}, is larger than E_{FM-AFM}, then a domain wall is not energetically favorable, and the system shows maximum exchange bias, given by $H_{EB} = J_{FM-AFM}S_{AFM}S_{FM}/(\zeta aMt)$, where t is the thickness of the FM, and M is the magnetization of the FM. If the opposite is true, then the exchange bias is determined by the formation of a domain wall, $H_{EB} = E_{DW}/(Mt)$ [42].

1.4 Exchange Bias in Nanostructured Systems

The behavior of exchange bias at the nanoscale is drastically different from that of larger samples, and there have been many inconsistencies in the literature about exchange bias trends at the nanoscale. There are many contributions for this, including the choice of fabrication method, the size and shape of the features, the materials used, how much of the FM is exchange biased, and the amplification of temperature effects in nanostructures.

1.4.1 Fabrication Methods for Optimizing Exchange Bias

In many devices, the full stack of FM and AFM layers is deposited and patterned together into the same shape. However, for devices where only a portion of the FM layer must be pinned by an AFM and the rest must be unpinned, it is necessary to develop a fabrication method that preserves the high quality FM/AFM interface required for exchange bias in selected regions of the FM. This can be accomplished either by a subtractive process, i.e., depositing the exchange-biased stack and then removing the AFM from selected regions, or by an additive process, i.e., depositing the FM and then depositing the AFM over selected regions. In the latter case, since the FM surface is coated with resist and exposed to atmosphere between the two steps, it must be cleaned prior to depositing the AFM to ensure a good quality interface. Both processes require etching of the magnetic materials, either to remove the AFM or to clean the FM prior to AFM deposition. Reactive ion etching (RIE) processes are difficult to use because common FM and AFM materials do not form volatile etch products even at elevated temperatures [44]. One solution is the use of a high-density plasma for the ion-assisted desorption of metal chloride etch products, but this requires careful control of etch chemistry and process conditions, and etch rates are relatively slow [44]. An alternative is the use of ion beam etching (or ion milling), but this suffers from the

disadvantages of poor selectivity, sidewall redeposition, ion implantation, and atomic displacements leading to increased magnetic pinning [45, 46]. However, other studies show that even for NiFe feature sizes as small as 100 nm, there was no evidence for magnetic damage caused by ion beam etching [47], and ion beam etching is used industrially for making magnetic random access memories [48].

For subtractive methods, in addition to etching away portions of the AFM, selective exchange bias can also be accomplished using ion bombardment through a resist mask to locally alter magnetic properties [49], or by oxidizing an AFM in select portions of the film to remove exchange bias from that region, as shown schematically in Fig. 1.9 [50]. However, the lateral resolution of these techniques is limited by ion straggle and diffusion, and it has been limited to introducing exchange bias into features larger than 1 μm.

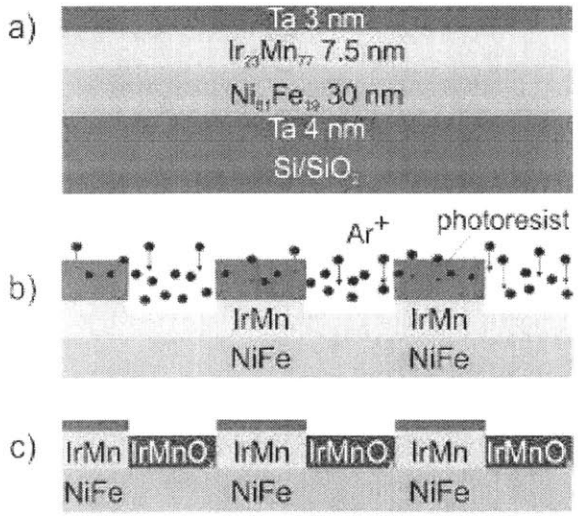

Figure 1.9: Schematic of a subtractive method of fabrication for exchange biased nanostructures. A pattern is made using photolithography on top of a continuous bilayer film. The Ta layer is etched away, and oxide is introduced into the exposed IrMn by annealing. Figure adapted from [50].

For additive methods, the mask used to pattern the AFM layer may be created using a number of techniques including lithography and porous membranes [51]. An example of an additive

method is shown in Fig. 1.10. However, regardless of the shadow mask technique used, contamination of the AFM-FM interface between the two separate deposition steps can degrade exchange bias. In section 2.1.6, we present a hybrid fabrication method that combines the clean interface of the subtractive method with the flexibility and scalability of the additive method.

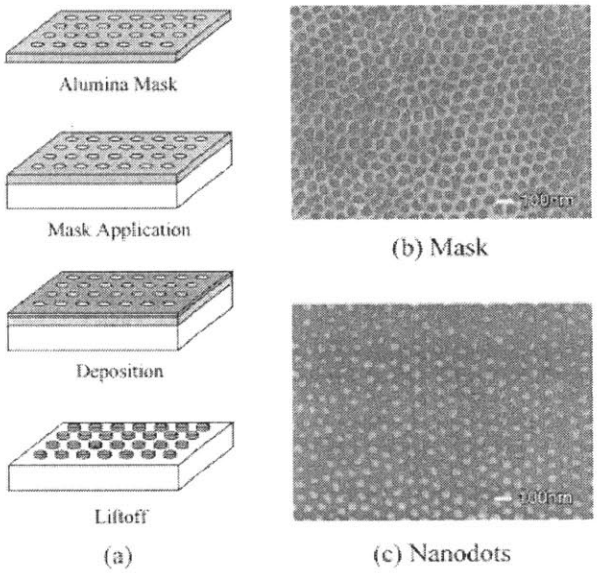

Figure 1.10: (a) Schematic of an additive fabrication method, using a porous alumina mask to selectively deposit Fe dots. (b) SEM image of the membrane mask. (c) SEM image of the array of Fe nanodots. Figure from [51].

1.4.2 Size Effects on Exchange Bias

It is well known that many of the magnetic properties of magnetic structures depend heavily on their size, aspect ratio, and shape [52, 53]. These effects could potentially have an even greater impact in exchange biased nanostructures, because patterning would not only affect the FM and AFM parts individually, but also the coupling between them. Despite the potential impact scaling can have in exchange biased nanostructures, and despite their importance in magnetic recording, memories, and sensors, there have been very little research on the effects of lateral size reduction to the nanoscale. In other words, exchange bias has simply been optimized in devices without fully

understanding the effects of scaling. Unfortunately, there is only a small number of studies on nanoscale exchange bias, and a lot of those are on different FM-AFM systems, different shapes, and different structures. Furthermore, many of those studies are conflicted with one another. As a result, it is difficult to provide a clear general understanding of the effects of size reduction in exchange bias. However, in the following sections, we will highlight the main existing results of miniaturization on exchange bias both for structures in which the FM and AFM are patterned the same, and for structures in which the AFM is patterned differently from the FM, which shows qualitatively different behavior than the former.

1.4.2.1 Equal Patterning on FM and AFM

Structures in which the AFM and FM are patterned simultaneously and deposited in one continuous step, shown in Fig. 1.11, are the most studied structure type. Despite that, there are disagreements present for each material type. For FM-AFM wires with NiO as the AFM, some studies report an increase in exchange bias as wire width is decreased [54, 55], and that the exchange bias is proportional to 1/w, where w is the width of the wire. In contrast, other studies indicate the opposite [56]. There are similar disagreements for CoO-based wires and IrMn-based wires [57, 58, 11]. The direction of exchange bias is extremely important for some systems including the Fe-F_2 system, whose exchange bias magnitude and sign could be tuned by setting the exchange bias and wire axis at different angles [60, 61].

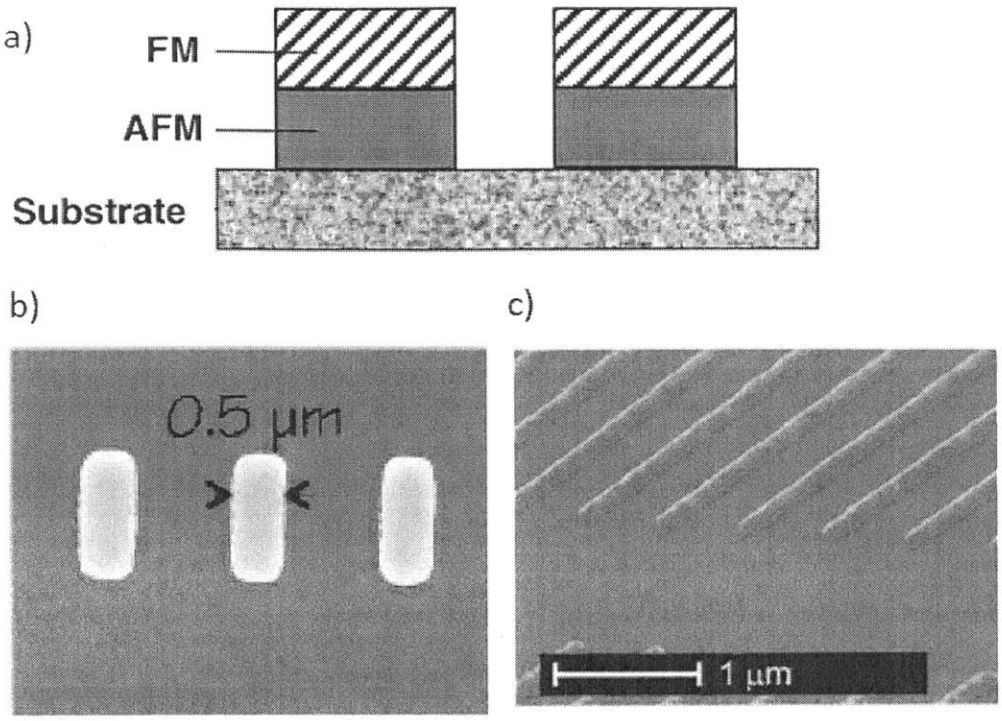

Figure 1.11: (a) Schematic of a structure in which the FM and AFM are patterned equally [12]. (b) SEM image of an example of such a structure containing IrMn-CoFe nanodots [63]. (c) Another example containing Ni-NiO lines [56].

For exchange biased dots, most studies agree that exchange bias decreases with size reduction for all sizes and AFM materials [62, 29, 63]. This is attributed to the magnetostatic energy of the dots competing with the exchange bias. As the size is reduced, shape anisotropy starts to play a major role, and without exchange bias present, vortices (or closure domains in some other shapes [52] develop. With the AFM present, a competition between the unidirectional anisotropy and the magnetostatic energy is induced.

1.4.2.2 Partial Exchange Bias

The magnetic behavior of locally-exchange biased thin films in which the FM and AFM have different dimensions and the exchange bias is limited to only part of the FM, differs qualitatively from that of the patterned FM-AFM bilayer. Unlike the bilayer, the reversal mechanism of the FM

depends on the length scales of the pinned and unpinned regions and the strength of the exchange bias in the pinned regions. For example, continuous NiFe films with overlaid FeMn stripes of micrometer-scale periodicity showed complex hysteresis loops, as shown in Fig. 1.12 [49], suggesting that the pinned and unpinned regions reverse at different fields. In other studies [64, 50], exchange bias parallel to the stripes produced switching in two steps, one for the unpinned portion, and one for the pinned portion. On the other hand, exchange bias perpendicular to the stripes produced switching in one step.

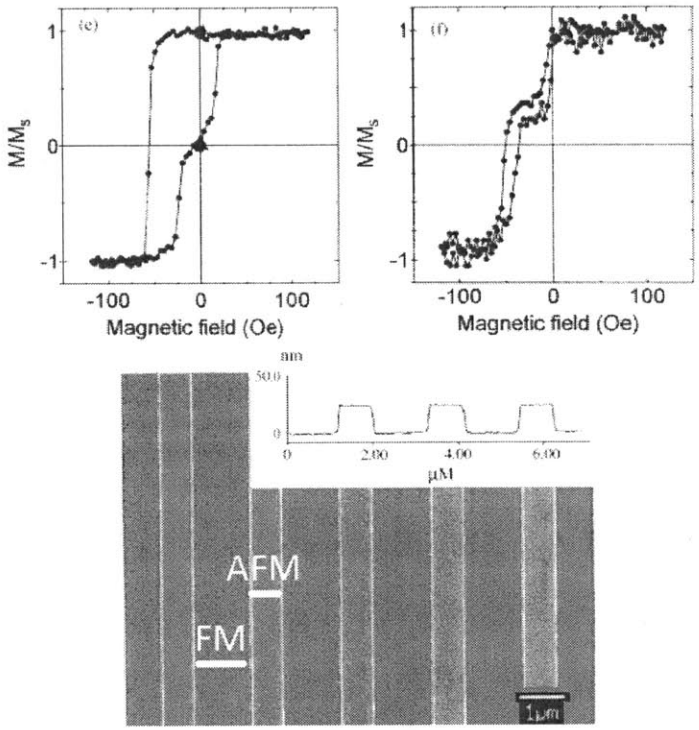

Figure 1.12: Complex asymmetrical hysteresis loops (top) generated from two magnetically different regions interacting. SEM image of the regions are shown (bottom). Figure adapted from [49].

At the time of this writing, research on nanoscale structures with partial exchange bias is extremely limited, and there is no basis to simply infer that the behavior at the nanoscale will scale similarly to that at the micrometer scale. For example, in large structures, reversal usually takes

place through the nucleation and propagation of domain walls, whereas in small nanostructures, the possible reversal modes are limited, and coherent rotation, curling, or buckling becomes more common [52], which could lead to differences in exchange bias behavior. In addition, because AFM microstructure plays an important role in exchange bias, the confinement of AFM domains in nanostructures could also drastically alter exchange bias behavior. Furthermore, uncompensated spins have been reported to play an important role in exchange bias [22]. These uncompensated spins have a very different distribution in nanoscale structures compared to micrometer-scale structures due to edges featuring more prominently in the former. Understanding and manipulating the reversal process of a magnetic film with local exchange bias is, therefore, a key part of magnetic device design, providing, for example, the ability to trap a domain wall or to initiate reversal in a magnetic nanostructures. However, despite its importance, the behavior of magnetic films patterned with nanoscale AFM features and how the regions interact at smaller dimensions has not been explored. In chapter 4, we present such a submicron pattern and investigate its switching behavior.

1.4.2.3 Training Effect and Blocking Temperature

Both the training effect and blocking temperature appear to be more pronounced for smaller exchange biased structures than they are for larger ones.

In general, the blocking temperature decreases with the reduction of feature size. For example, square dots based on IrMn showed a blocking temperature reduction with respect to continuous films of more than 30 K [29]. A similar effect was observed in CoO-based structures [65]. In certain AFM systems in which the blocking temperature is close to room temperature, this reduction can potentially be a limiting factor in device design. The reduction in blocking

temperature was observed for all samples described in chapters 3, 4, and 5, but in all cases, the blocking temperature remained well above room temperature.

As mentioned in section 1.3.1, the training effect is more pronounced for systems with thin AFM layers (i.e. small AFM domains), or small AFM grains [66, 67]. In addition, the training effect has been suggested to originate from the reconfiguration of AFM moments to a low-energy stable state during each reversal. Thus, the training effect is generally enhanced in nanostructure systems compared to continuous films [66, 68].

Chapter 2

Experimental and Modelling Methods

In this chapter, we describe procedures for fabricating samples, methods of introducing exchange bias into the samples, ways of characterizing samples, and tools for micromagnetic modelling.

2.1 Fabrication

All samples were fabricated on top of Si wafers with native oxide.

2.1.1 Interference Lithography

Samples with arrays of repeating nanostructures were fabricated using the Lloyd's Mirror interference lithography system. A schematic of the system is shown in Fig. 2.1, along with a photograph of the laser and mirrors.

With interference lithography, period gratings are generated with two mutually coherent beams of light, which form a standing wave pattern that exposes the resist in the region where the two beams overlap. Because beams of light from different sources cannot be expected to be mutually coherent, the two beams come from the same source. The mirror next to the substrate divides the source beam into two overlapping beams that form the standing wave pattern. To avoid distortions, the beam is spatially filtered through a 5 μm pinhole before expanding to a diameter of about 20 cm at the mirror and sample.

The periodicity of the wave pattern depends on the incident angle of the beam, and is related by $p = \lambda/2\sin(\theta)$, where λ is the wavelength of the laser (the Lloyd's Mirror uses a 325 nm HeCd

laser), and θ is half the angle between the two beams. The angle is computed and then set by rotating the stage holding the mirror and sample. Exposure time varies depending on the power of the laser at the center of the stage. Typically, we extract an exposure time from the archives for the periodicity of interest, and multiply that recorded exposure time by the ratio of the current power to the power recorded in the archives for that exposure.

The samples were prepared using AZ BARLI antireflective coating (ARC), and OHKA THMR-iN PS4 negative photoresist (PS4). The ARC was spin coated and baked at 180° C for 90 s, while the PS4 was spin coated and baked at 90° C for 90 s. An interlayer of SiO_2 (20 nm) was applied by electron beam evaporation in between the ARC and PS4. Because PS4 has adhesion problems with SiO_2, an adhesion promoter such as hexamethyl disilazane (HMDS) was used.

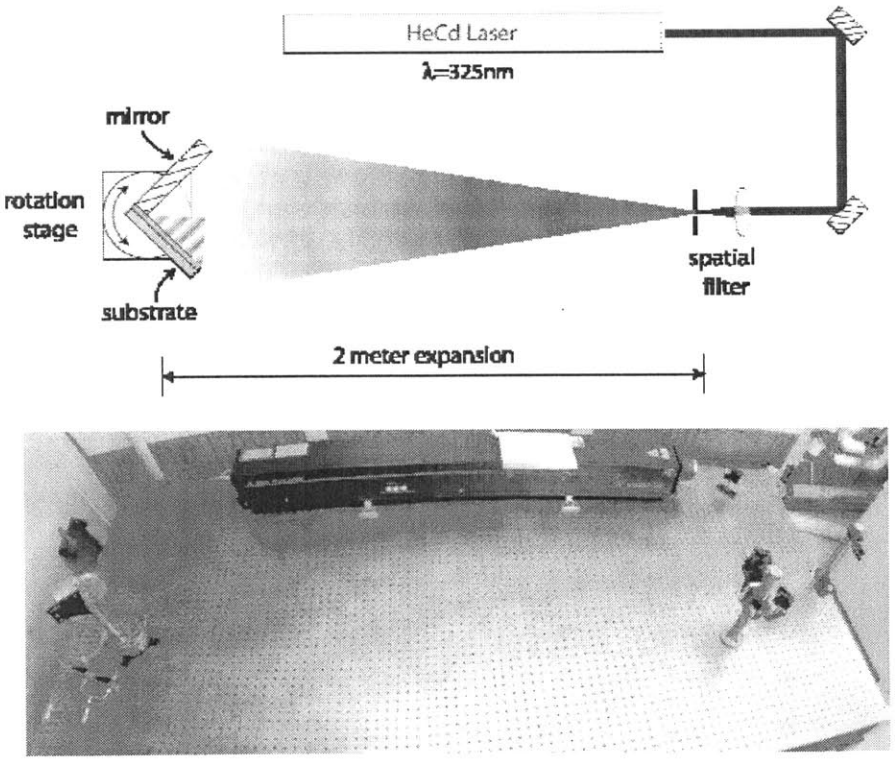

Figure 2.1: Top: Schematic of the Lloyd's Mirror interference lithography system. Bottom: Photograph of the Lloyd's Mirror with the protective covers removed, showing the laser and mirrors. Figure adapted from [69].

After the exposure, the PS4 was baked again at 110° C for 90 s and developed in CD-26 for 60 s, then rinsed in DI water and spin-dried. The resist pattern was then transferred into the interlayer using reactive ion etching (RIE), which was done using the Plasmatherm RIE system. First, CF_4 plasma was used to etch through the SiO_2, but not the ARC. Then, the pattern is transferred through the ARC layer, using a He/O_2 plasma, which etches ARC but not SiO_2.

The thicknesses of the trilayer resist stack depends on reflectivity. The purpose of the ARC is to reduce the amount of light reflected back into the resist. To calculate the thickness of the ARC, the thicknesses of the other layers were entered into a program provided by the NanoStructures Laboratory, and a reflectivity curve is generated. For the example in Fig. 2.2, it can be seen that the optimal ARC thickness is between 200 nm and 250 nm. For the samples used in this study, the ARC thicknesses typically ranged from 200 to 300 nm for a PS4 thickness of 210 nm.

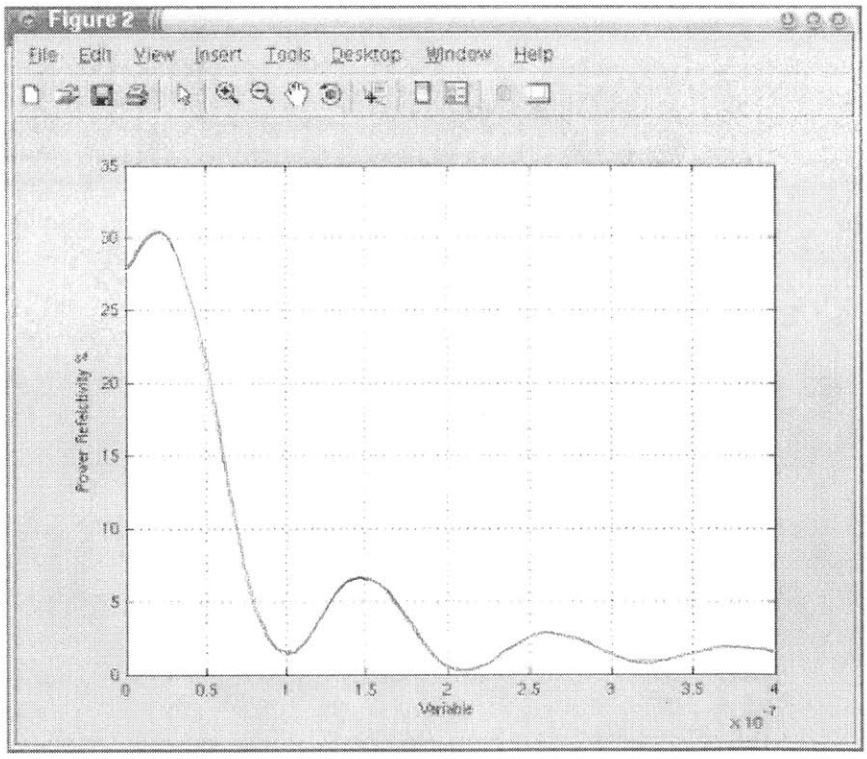

Figure 2.2: MATLAB output graph of reflectivity versus ARC thickness. Typically, a less than 1% reflectivity is desired. Figure from [69]

2.1.2 Electron Beam Lithography

Small non-repeating structures were fabricated using electron beam lithography. Poly methyl methacrylate (PMMA) positive resist was spun at 3.5 kRPM for 60 s to give a thickness of 150 nm, then baked on a hot plate at 110° C. Afterwards, the samples were exposed using the Raith 150 electron beam lithography system at 10 kV, 7 mm working distance, 20 μm aperture size, and a dose factor of 1.5. For samples with multiple layers with different patterning, three alignment marks were used.

After exposure, the samples were developed in a solution of 3:1 isopropanol:methyl isobutyl ketone by volume for 90 seconds and rinsed with isopropanol and either spin-dried or dried with nitrogen gas. This produced a resist mask pattern ready for deposition.

2.1.3 Deposition

The FM and AFM layers of all samples were deposited using DC magnetron sputtering. Ion beam etching of the FM occurred in the same sputtering chamber. The SiO_2 used in the interference lithography resist mask preparation was deposited by Jim Daley in the MIT NanoStructures Laboratory using electron beam evaporation.

2.1.3.1 DC Magnetron Sputtering

Sputtering involves ejecting atoms from a target and transferring them onto a substrate. A small fraction of the ejected atoms are ionized, fly from the target, and bombard the substrate. In magnetron sputtering, strong electric and magnetic fields are used to trap electrons close to the surface of the target. The electrons follow a helical path based on the magnetic field lines, and they collide with more gas atoms than usual, creating more ionization and a higher deposition rate. In

addition, the plasma is also self-sustaining at a lower pressure. A schematic of the process is shown in Fig. 2.3

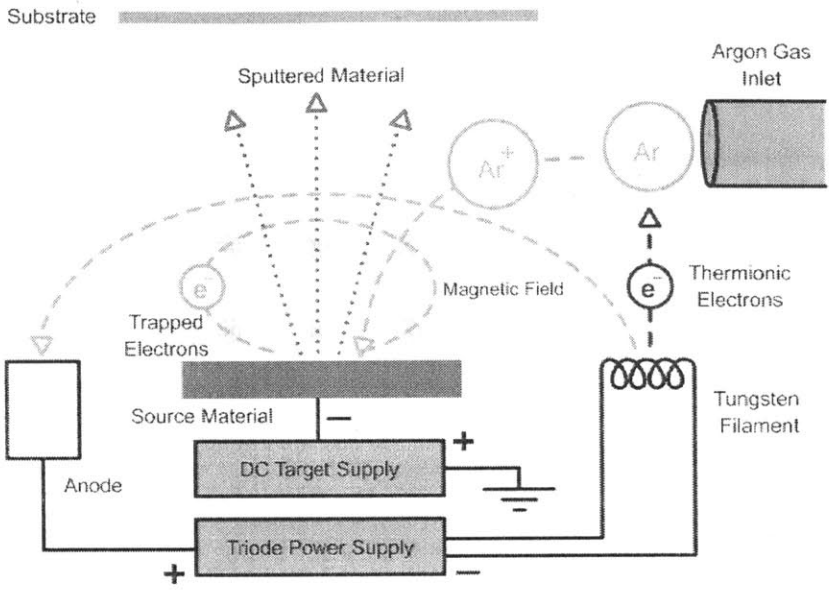

Figure 2.3: A schematic of a DC magnetron sputtering system. Figure from [70].

NiFe, IrMn, Ti, Ta, and CoCrPt films in patterned samples were deposited using DC magnetron sputtering using argon plasma with a triode power supply. The main chamber's base pressure typically ranged from 1×10^{-8} Torr and 5×10^{-8} Torr. An argon pressure of 5 mTorr was used to ignite the plasma, but was lowered to 1 mTorr for deposition. Plasma voltage was typically 60V, and plasma current ranged from 1.5 A to 2 A. The DC magnetron's power supply was fixed at 100 W, and each target was presputtered for five minutes prior to deposition to remove any impurities on the surface.

Deposition rates of magnetic materials were monitored using vibrating sample magnetometry on a prime Si wafer exposed for a fixed period of time. Deposition rates of non-magnetic materials were measured using atomic force microscopy or profilometry on a sample with a well-defined

edge of material produced with liftoff. Typical deposition rates ranged from 0.1 to 1 nm per second, and the deposition rates were re-measured every time the main chamber was vented and pumped down for maintenance.

2.1.3.2 Ion Beam Etching

Ion beam etching, also known as ion milling, is a dry etching technique in which gaseous ions are accelerated into the surface of the sample to remove the atoms at the surface. It can be visualized as a nanoscale form of sandblasting.

Ion beam etching in our samples took place in the same chamber as DC magnetron sputtering. Argon gas was used at a pressure of 2×10^{-4} Torr, and the ion beam etching was carried out under an ion beam voltage of 500 V and current of 5.5 mA to produce an etch rate in the NiFe ranging from 0.17 nm/s to 0.26 nm/s. Because the etch rate changes slightly every time the main chamber was vented and pumped down for maintenance, the etch rate was re-measured accordingly. Samples were typically ion beam etched for around 3 s to remove the oxide layer and slightly back etch into the bulk NiFe.

2.1.3.3 Electron Beam Evaporation

Electron beam evaporation is a vapor deposition technique in which an electron beam is generated and guided by electric and magnetic fields onto a target. The beam vaporizes the target material, leaves the surface, and travels across the vacuum chamber, coating the sample. A schematic of an electron beam evaporation setup is shown in Fig. 2.4

The SiO_2 used to prepare the trilayer resist for interference lithography was deposited by the NanoStructures Laboratory using electron beam evaporation. After the antireflective coating was spun, 20 nm of SiO_2 was evaporated.

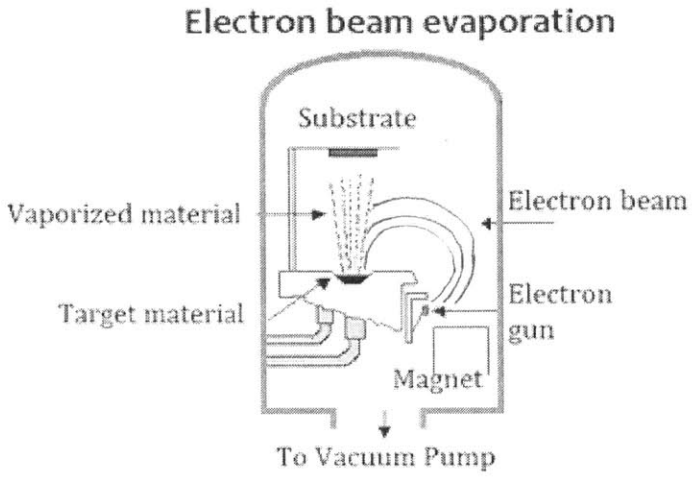

Figure 2.4: A schematic of an electron beam evaporation setup. Figure from [25].

2.1.4 Liftoff

Liftoff was performed in N-methyl-2-pyrrolidinone (NMP) for samples that were used in chapter 3. Samples were heated at 135° C in a small container of NMP on a hot plate for varying lengths of time depending on the resist. PMMA was immersed for five minutes, whereas the ARC required two to four hours. On the other hand, for samples that were used in chapters 4 and 5, the 1165 solution, which contains mostly NMP, was used because the NanoStructures Laboratory begun stocking 1165 rather than NMP. When lifting off samples with ARC, the 1165 was heated to 80°C for four hours. Usually, sonication was performed for a few seconds after immersion, after which samples were immersed in fresh NMP for an additional few minutes. Sonication and immersion were repeated again if necessary. Afterwards, samples were rinsed in isopropanol and dried in nitrogen gas.

2.1.5 Setting Exchange Bias

Exchange bias was set using two methods: by using an in-situ magnetic field during deposition, and by field-cooling the sample after deposition.

For the in-situ magnetic field, a sample holder with two permanent bar magnets attached was used. The bar magnets produced a field of 400 Oe—more than enough to fully saturate NiFe, which has a coercivity of a few Oersteds. With the NiFe saturated, the AFM is deposited under the same magnetic field. The first layer of AFM spins align ferromagnetically to that of the saturated FM. Then, the other spin planes in the AFM follow the order of the first layer to produce zero net magnetization. After the sample is removed from the magnetic field, the FM layer at the interface is still aligned with the AFM layer at the interface. However, the in-situ field method is less reliable than the field-cooling method, because there are intrinsic magnetic fields in the DC magnetron sputter system, and as a result, the strength and direction of the net magnetic field at the sample may not be exactly what is expected.

For field-cooling, the sample was heated under a field of 1 kOe to a temperature range of 460 K to 520 K depending on the size of the features. The temperature was chosen to be greater than the blocking temperature of the AFM-FM system, but lower than the Curie temperature of the FM. Therefore, under the magnetic field, the FM spins line up with the field, and the AFM spins remain random. After being held in this state for 10 min, the sample was allowed to cool to room temperature under the same field for 30 minutes. Due to the interaction at the interface, when the sample is cooled below the Néel temperature, the AFM spins at the interface align ferromagnetically with the FM spins at the interface, and the other layers follow to produce a zero net magnetization. After the magnetic field is removed, the FM is still aligned with the AFM at the interface, and exchange bias is produced.

There was no significant difference between the hysteresis loops of samples that were prepared by field-cooling and samples that showed as-grown exchange bias. Field-cooling the samples that showed as-grown exchange bias did not change the hysteresis loop either. However, as some of the as-grown samples did not show exchange bias, field-cooling was used prior to the majority of measurements.

2.1.6 Hybrid Fabrication Method for Partial Exchange Bias

In section 1.4.1, commonly used fabrication methods for patterning small exchange-biased structures were described, as well as their advantages and disadvantages. Here, we present a two-step hybrid fabrication method that combines the scalability and flexibility from the additive methods, and the clean interface from the subtractive methods. A general schematic of the procedure is shown in Fig. 2.5. After the resist mask pattern for the FM is processed, a seed layer of Ta (5 nm) is deposited for all samples, and the FM is deposited via DC magnetron sputtering (Fig. 2.5, step 2). The sample is then removed from vacuum and lifted off, in preparation for the next processing step and as a result, oxide and other impurities build up (step 3). The oxidized sample is then processed again to create a resist mask patterning for the AFM (step 4). However, before the AFM is actually deposited, the sample is subject to a 3 second ion beam etch (step 5) to remove the oxide (etch duration depends on the etch rate of the material), then redeposited with 1 nm of the FM (step 6). Finally, the AFM is deposited, and the sample is lifted off (steps 7, 8). Steps 5 through 7 are performed without breaking vacuum, preserving the high-quality interface necessary for exchange bias. The pattern processing used to make each type of sample will be covered in more detail in the relevant sections.

Fig. 2.6 demonstrates that the bulk FM properly exchange couples with the redeposited FM as if it were a continuously deposited film. The hysteresis loop of the NiFe that has been subject to the 3 second etch and 1 nm redeposition is that of a typical continuous NiFe film.

This fabrication method not only produces a clean FM-AFM interface, but it also can be scaled down as far as lithography can go.

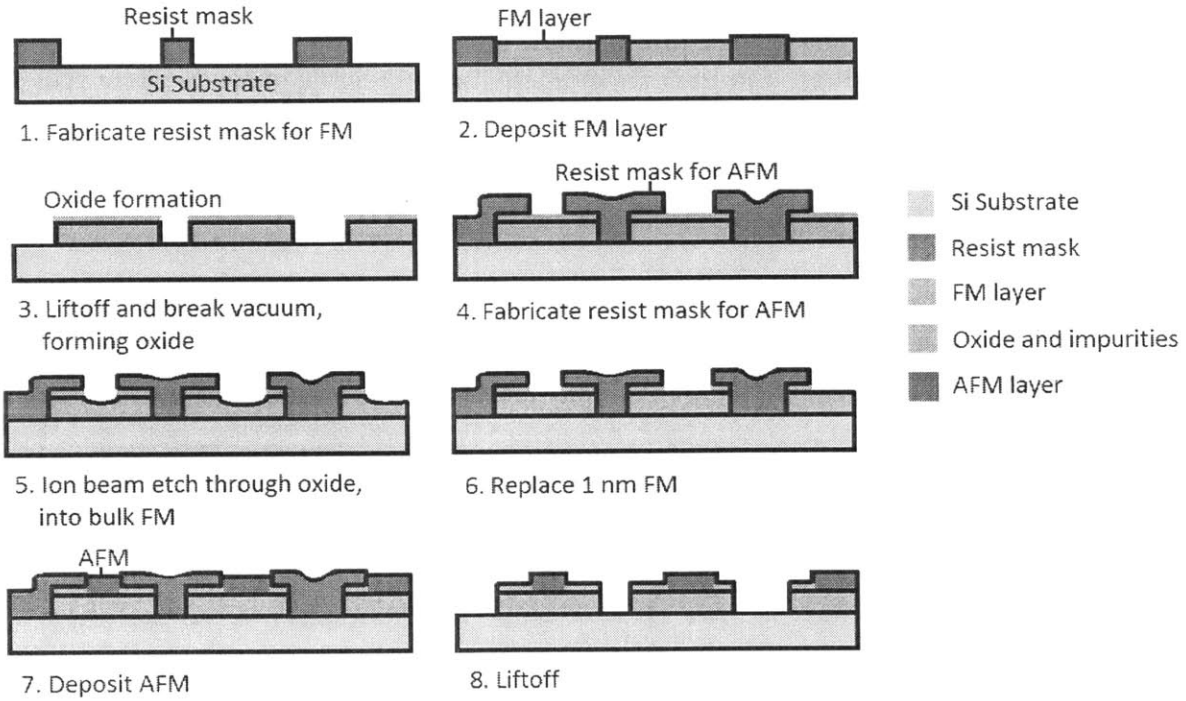

Figure 2.5: Schematic of the two-step hybrid fabrication procedure. Even though vacuum is broken in between the first and second processing steps, a high-quality interface is produced by back etch and redeposition.

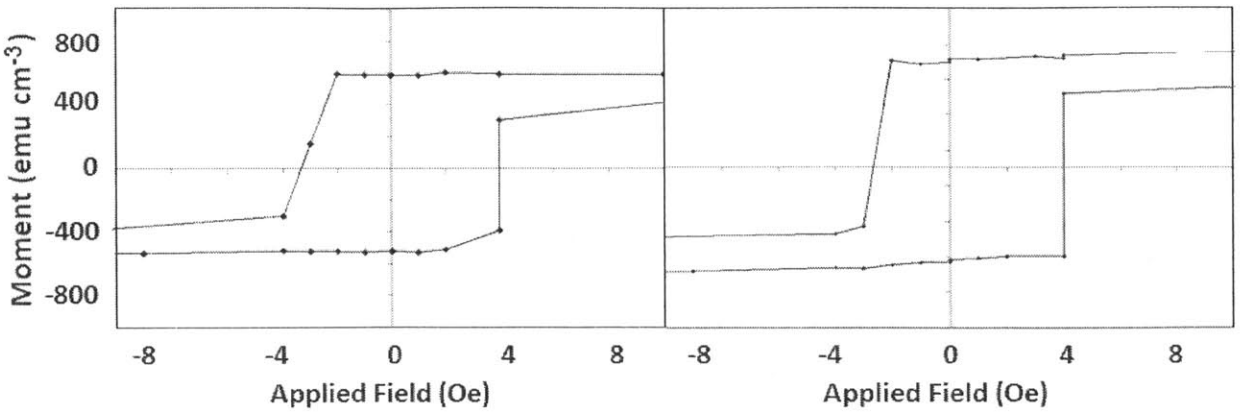

Figure 2.6: The effect of ion beam etching and redeposition process on a NiFe continuous film. Left: a continuously grown NiFe film without any patterning. Right: a NiFe film after ion beam etch and redeposition. Similarities indicate that 3 seconds of ion beam etching has little effect on the magnetic properties.

2.2 Characterization

Because interference lithography allows patterning of a large area, samples had enough magnetic moment for measurement using vibrating sample magnetometry (VSM), which was used to produce hysteresis loops of the majority of samples. Scanning electron microscopy (SEM) was used to view the surface of the samples.

2.2.1 SEM

Scanning electron microscopy was performed on the ZEISS 982. A SEM produces images by raster scanning a sample with a focused electron beam. The electrons interact with the sample to produce low-energy secondary electrons and high-energy backscattered electrons, both of which are sent to detectors and combined with the beam's position to produce a topographical image. The SEM images taken during this study were typically taken under 100,000x magnification.

2.2.2 VSM

Vibrating sample magnetometry was performed on an ADE Technologies VSM Model 1660. VSM operates based on Faraday's law to measure a sample's magnetization under an applied magnetic field. Faraday's law of induction states that the induced electromotive force in a coil is equal to the negative rate of change of the magnetic flux enclosed by the coils. In other words, $Emf = -N\, d\Phi/dt$, where N = number of turns in a coil, $\Phi = BA$ = magnetic flux, B = magnetic field, and A = area of the coil. A schematic of a VSM is shown in Fig. 2.7. The sample is loaded onto a quartz sample holder and vibrated along the z-direction. At the same time, a magnetic field is applied along the x-direction. As the sample vibrates, magnetic flux is generated and the voltage is picked up from the coils. The voltage is then converted to a magnetization value after being compared to that of a previously tested standard reference sample.

The VSM can measure magnetization down to 10^{-6} emu. As a result, individual nanostructures cannot be characterized using VSM. However, arrays of nanostructures made using interference lithography cover a wide area, and samples measuring 0.5 cm × 0.5 cm easily produce a large enough signal. The VSM is also equipped with a coil heater for high temperature measurements of up to 700° C. The Field-cooling procedure described in section 2.1.5 makes use of this heater.

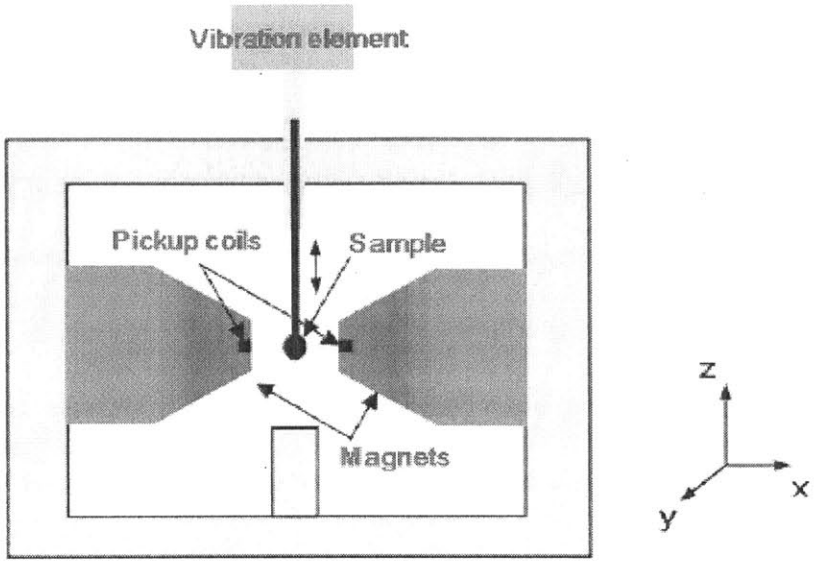

Figure 2.7: Schematic of a VSM setup. Figure from [72]

2.2.3 AFM and MFM

Atomic force microscopy (AFM) and magnetic force microscopy (MFM) were performed on a Veeco/Digital Instruments atomic force microscope. For AFM, atomic and electrostatic forces between the tip and the sample deflect a flexible cantilever, and a height profile is calculated. Similarly, in MFM, a magnetic tip scans a magnetic sample. Magnetic interactions between the tip and sample are measured, and a magnetic structure profile of the sample is mapped out. To avoid topographical interference, the magnetic signal is extracted by performing a close scan, a far scan, and subtracting topological influence.

Because NiFe is extremely soft, with a coercivity of a few Oersteds when not pinned and about a hundred Oersteds when exchange biased, low-moment MFM tips were used to minimize the accidental switch of magnetization by the tip's stray field.

2.3 Micromagnetic Simulation

The Object Oriented MicroMagnetic Framework (OOMMF) package, created and developed by the National Institute of Standards and Technology (NIST) [73], was used for micromagnetic simulations. The OOMMF time driver is based on the Landau-Lifshitz-Gilbert equation, $dM/dt = -\gamma[M \times H_{eff}] - \alpha(M/M_s) \times (dM/dt)$ [74] where γ is the electron gyromagnetic ratio, M is the magnetization, H_{eff} is the effective field which includes the external magnetic field and the demagnetizing field, and α is the damping parameter.

A rectangular mesh was used with cell sizes chosen such that the cell length of each dimension was smaller than the exchange length of the magnetic material. For simulations involving an infinite array, the mesh was subject to periodic boundary conditions in one direction, while the other direction was set to 2μm to minimize the influence of edge effects. At the time of this work, there had not yet been an OOMMF add-on that allowed periodic boundary conditions in two dimensions.

For quasistatic simulations, in which the relaxed state is more important than the dynamic states, the damping parameter α was set to 0.5. For dynamic simulations, the damping parameter was set to 0.01. Usually, a random anisotropy direction was used per mesh cell to simulate the polycrystalline samples. For NiFe, the anisotropy is negligible to begin with; however, a small random anisotropy was set to help break symmetry inside the sample. Materials parameters for the materials used in simulations are shown in Table 2.1.

Parameter	Permalloy		Yttrium Iron Garnet	
Saturation Magnetization M_s	$800 \times 10^3\ A/m$	$800\ emu/cm^3$	$175 \times 10^3\ A/m$	$175\ emu/cm^3$
Anisotropy Constant K	$800\ J/m^3$	$8000\ erg/cm^3$	$2500\ J/m^3$	$25000\ erg/cm^3$
Exchange Stiffness (with self) A	$13 \times 10^{-12}\ J/m$	$13 \times 10^{-7}\ erg/cm$	$13 \times 10^{-12}\ J/m$	$13 \times 10^{-7}\ erg/cm$

Table 2.1: Materials parameters for Permalloy and YIG. Both mks and cgs units are provided.

To simulate hysteresis loops, each data point on the loop is a measured magnetization along the applied field direction calculated after initializing the moments to random directions, then allowing the system to relax inside that applied field. This is different from how hysteresis loops are measured experimentally, but is necessary because stepping the magnetic field without reinitializing each step leads to extremely high and unrealistic switching fields due to the high symmetry and periodic boundary conditions in an ideal material trapping metastable states. This behavior is seen even when symmetry-breaking features such as notches, field offsets, and anisotropy distributions are introduced.

Exchange bias was modeled as a fixed external field present in the regions of FM covered with the AFM. This is a simplification, as exchange bias is an interface phenomenon and only affects the FM at the FM/AFM interface. However, it is justified in all simulations performed in this study because the FM film thickness of 10 nm used in all simulations corresponds to only two layers of cells which have almost identical magnetization directions.

Data collection and organization was facilitated with OOMMFTools [70]

Chapter 3

Arrays of Exchange Biased Nanodots

We first discuss applying the fabrication method presented in section 2.1.6 to a system of NiFe/IrMn nanodots. A modification of the hybrid fabrication procedure is shown as a schematic in Fig. 3.1(a), and a SEM image after step 3 and step 7 are shown in Fig. 3.1(b) and Fig. 3.1(c) respectively. During the exposure step, the samples were exposed twice, with the second exposure rotated 90° from the first in order to create an array of dots. The dot diameters ranged from 100 nm to 500 nm, and both a NiFe and IrMn thickness of 10 nm was used. The FM thickness was chosen to be large enough such that the ion beam etch and redeposition does not affect a significant portion of the bulk, and small enough to induce a large exchange bias into the system based on the $1/t_{FM}$ relation described in section 1.3. The AFM thickness is less important, as it has no impact on exchange bias in small features [41].

Although only one patterning step was required, the samples were removed from vacuum after FM deposition in order to produce some oxidation of the NiFe, modeling the conditions of a sample patterned in a two-step process. For comparison, unpatterned films of the same composition and thickness were also deposited, as well as patterned and unpatterned samples that had not been subject to any vacuum break or ion beam etching.

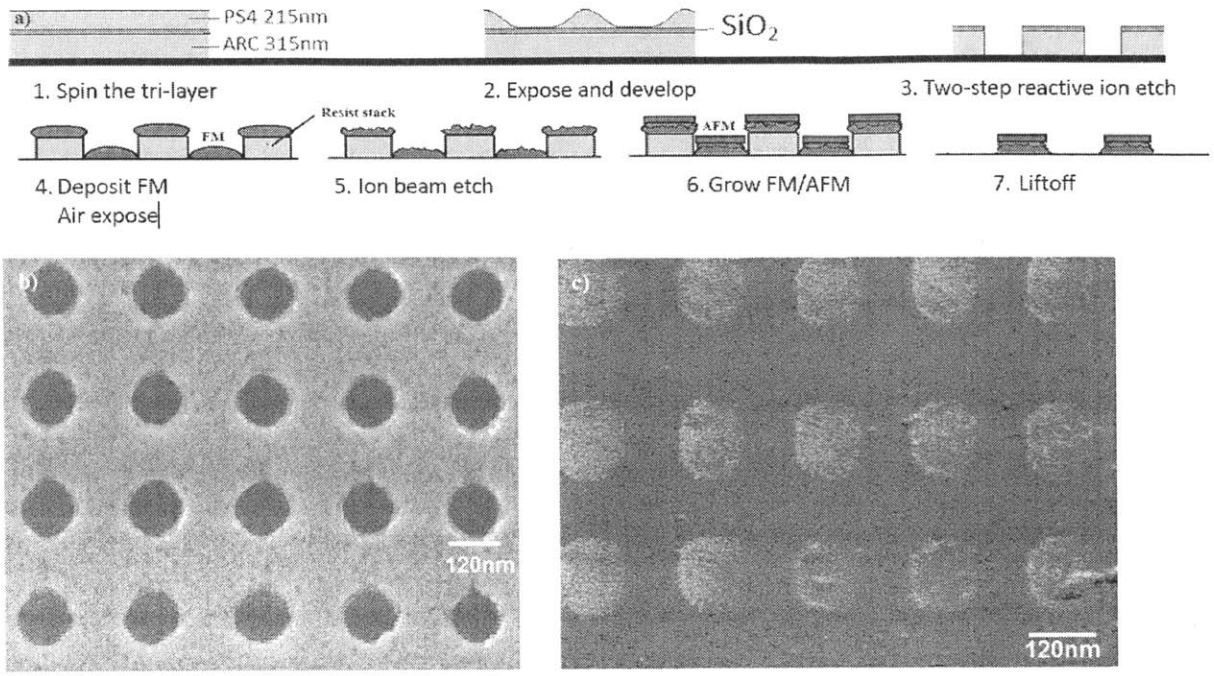

Figure 3.1: Method used to make nanodots samples. (a) Steps 1-3: Schematic of the resist mask fabrication. Steps 4-7: Schematic of the deposition process. (b) SEM image of a resist mask with period 200 nm before metal deposition. (c) SEM image of a NiFe/IrMn sample with period 200 nm. Small regions of residual ARC are visible but have no impact on magnetic measurements.

3.1 The IrMn / $Ni_{80}Fe_{20}$ System

Although one of the most studied and commercially used AFM has been $Fe_{50}Mn_{50}$ [22], IrMn was chosen for this study. Like FeMn, IrMn has good structural and chemical compatibility with NiFe. However, IrMn has a higher Néel temperature, as mentioned in section 1.3.1, and a larger magnetocrystalline anisotropy.

Historically, NiFe has been one of the most useful and thoroughly investigated FMs both scientifically and industrially. There are a few specific NiFe compositions that are of technical interest. $Ni_{50}Fe_{50}$ has a high flux density, giving very square hysteresis loops [30], and $Ni_{65}Fe_{35}$ maintains zero magnetocrystalline anisotropy. However, $Ni_{80}Fe_{20}$ was chosen because its

magnetostriction is zero at this composition, and its magnetocrystalline anisotropy is still extremely low. From Fig. 3.2, it can be seen that K_1 and λ_s cannot both be zero simultaneously. However, keeping $\lambda_s = 0$ takes priority because of the importance of structural compatibility with IrMn (111).

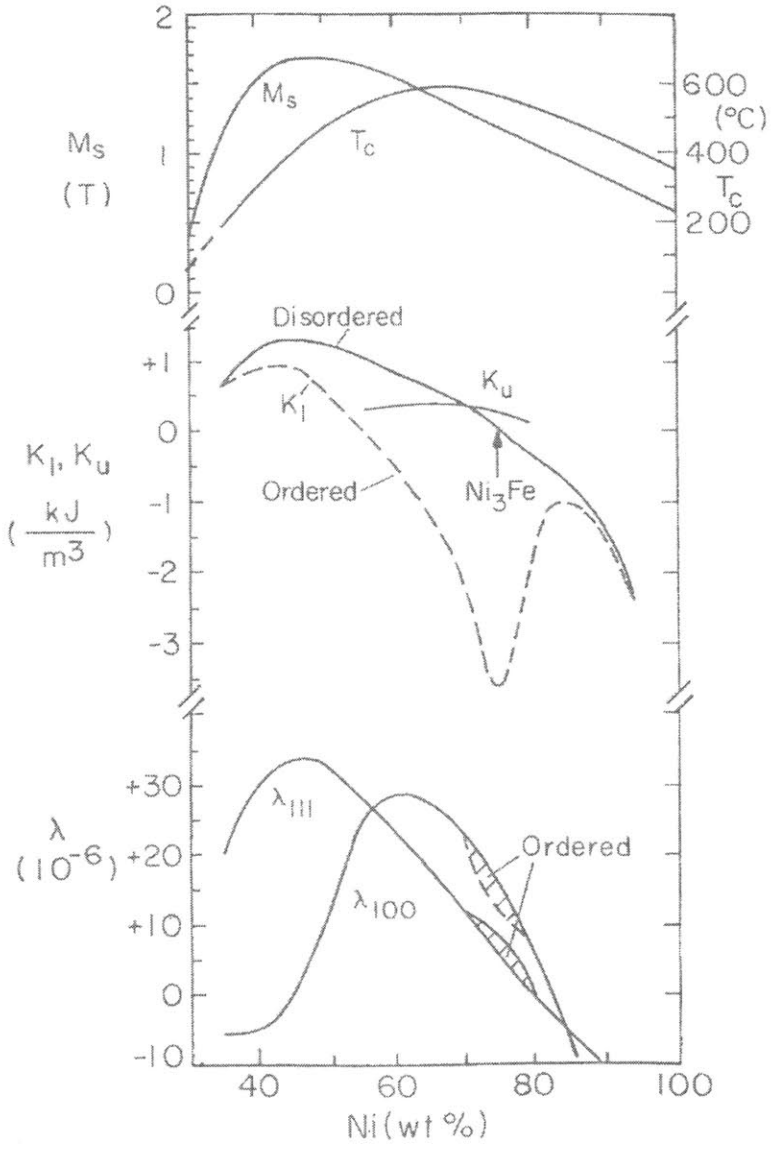

Figure 3.2: Variation of magnetocrystalline anisotropy and magnetostriction coefficients with Ni content by % weight in FCC NiFe alloys. Figure adapted from [30].

Although the NiFe/IrMn system has been thoroughly investigated both in literature and in industry for micron spin valve systems [22], the exchange bias behavior at the nanoscale has been far less studied. In particular, the impact that fabrication has on nanoscale systems is unknown. In the remainder of this chapter, we first discuss the effects of ion beam etching, a key part of the fabrication procedure, on exchange bias properties in both nanostructures and continuous films. Second, we discuss the effect of lateral size reduction on exchange bias and relate the effects with some common models. We then consider additional effects of size reduction, including the disappearance of vortex states and a change in the blocking temperature.

3.2 Effect of Ion Beam Etching on Magnetic Properties

It has been demonstrated that ion beam etching can severely damage surfaces [45]. Fig 3.3 shows what the surface of Si can look like after being subject to a two-minute Ar ion beam etch. It is also well known that exchange bias is an interface phenomenon. However, there have been no investigation of the effects of ion milling on magnetic properties at the nanoscale. For example, the damage caused by the bombardment may penetrate the surface and affect the bulk FM. More importantly, after a certain amount of ion beam etching, the switching behavior may drastically change, and exchange bias may disappear altogether.

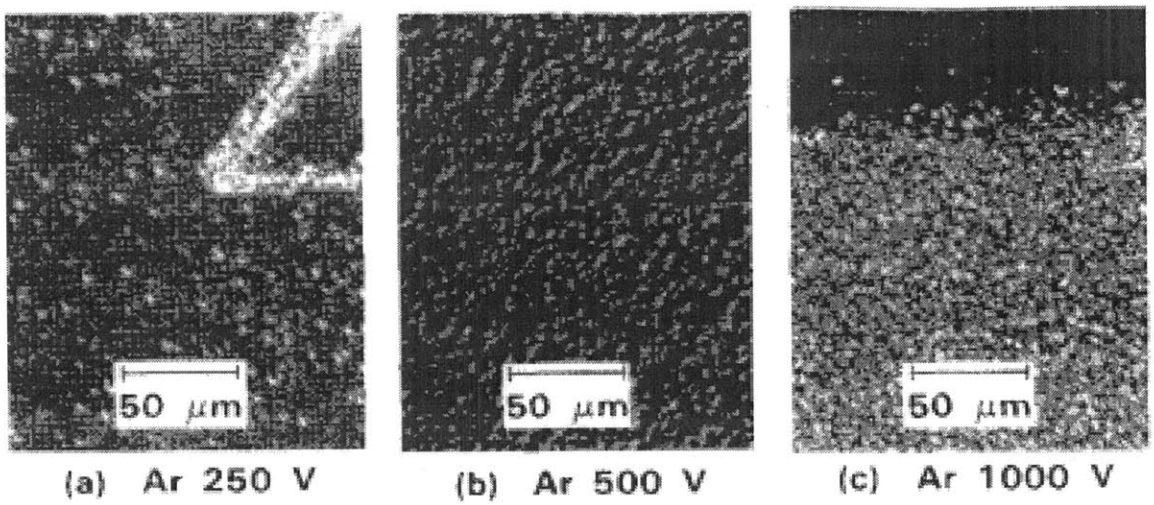

Figure 3.3: Optical microscope images showing oxidation-induced stacking faults in samples that were etched with Argon ion milling at (a) 250 V, (b) 500 V, and (c) 1000 V. Figure adapted from [45].

Fig. 3.4(a) shows the effect of ion beam etching on an exchange-biased unpatterned film made by the two step process, i.e., the 5 nm Ta/10 nm NiFe film was deposited, exposed to air to cause oxidation, then ion beam etched for various times before depositing 1 nm NiFe/10 nm IrMn. As expected, increasing the ion beam etching time lowered the magnetic moment because of the partial removal of the 10 nm NiFe layer. The moment decreased linearly until it reached approximately zero at 75 s, corresponding to the removal of NiFe at 0.14 nm/s. As the NiFe was etched, its coercivity increased as the surface roughened and impeded domain wall motion, followed by a decrease as its thickness fell below 5 nm and it presumably started to become discontinuous and vulnerable to thermally induced reversal. For ion beam etch times below 30 s, the exchange bias was consistent with the expected $H_E \sim 1/t_F$ law. However, beyond 30 s, exchange bias dropped, attributed to the damage to the NiFe caused by ion beam etching. This may be compared with the etching behavior of an exchange biased field-cooled dot array in Fig.

3.4(b). This data were only collected for etch times up to 40 s. The magnetic moment decreased at approximately the same rate as in the unpatterned film, though the initial decrease was faster, possibly due to the topography of the sample, in which the edges of the patterned Ta/NiFe film etched faster. The coercivity showed little variation with etch time.

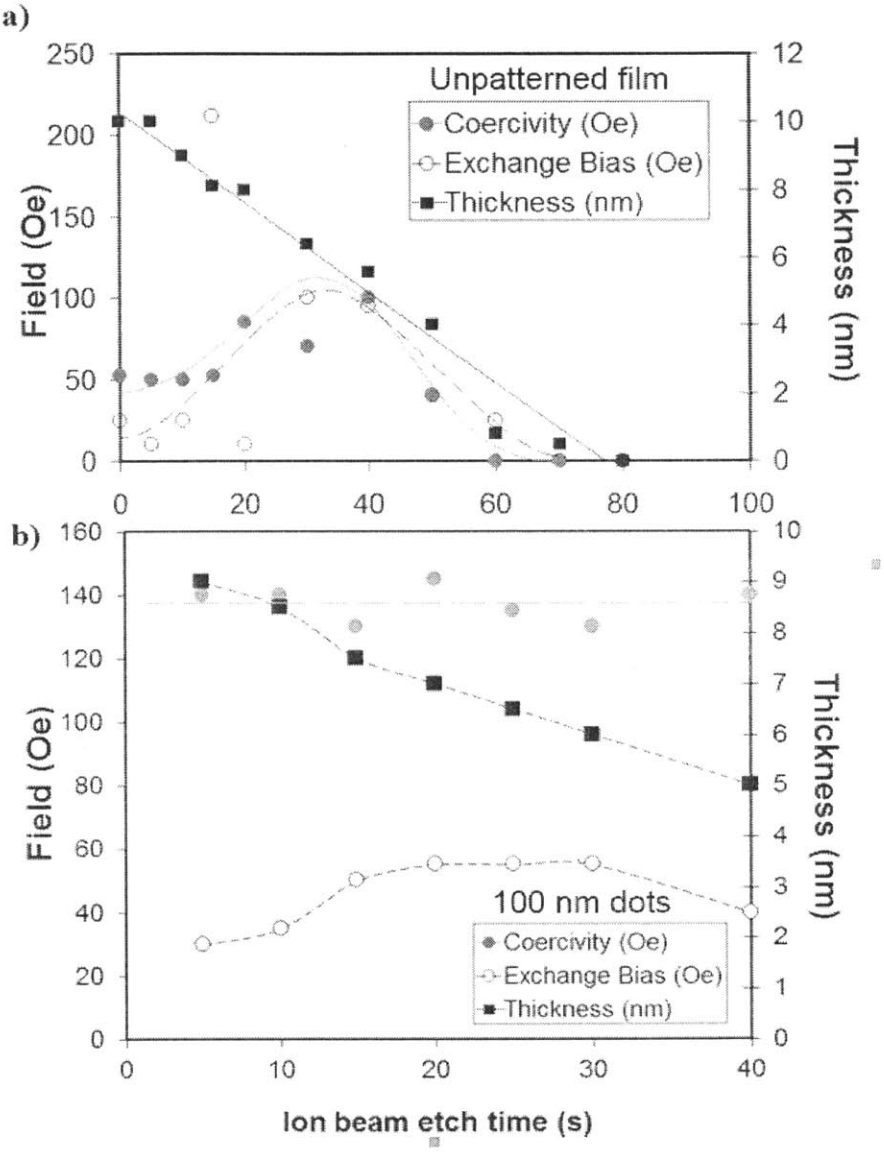

Figure 3.4: Coercivity, exchange bias, and thickness versus NiFe ion beam etching duration for (a) an unpatterned film. Ion beam etching occurred at 0.14 nm per second. The high exchange bias seen in the 15 s etched sample was not reproduced in subsequent samples processed under the same conditions. (b) Corresponding data for 100 nm diameter dots.

Fig. 3.5 compares the effect of ion beam etching on the hysteresis loops of both the unpatterned film and for a patterned field-cooled sample consisting of an array of 120 nm diameter dots. The unpatterned films showed a higher remanence, higher exchange bias, lower coercivity, and a much smaller switching field distribution than the dots. These differences are commonly seen in other samples of patterned exchange biased bilayers made without a vacuum break or etching [75]. The high switching field distribution for the patterned samples represents intrinsic variations in switching field between individual dots due to edge roughness from the liftoff process, microstructural differences, and defects introduced by the ion beam etching. Magnetostatic interactions between dots were negligible compared to the switching field, e.g., for 100 nm diameter, 10 nm thick dots with 250 nm period the nearest neighbor field based on a dipole approximation was 4 Oe. At long etch times (>40 s), the patterned and unpatterned samples showed similar switching field distributions as the NiFe layer became discontinuous. Fig. 3.6 summarizes the effects of ion beam etch duration on exchange bias for various dot sizes after field cooling. All the patterned samples showed an increase in the exchange bias in the first 40 s of ion beam etching except for the smallest diameter dots (and the continuous film), where the exchange bias peaked at 30 s etching. The etching lowered the NiFe thickness which favors higher exchange bias according to Malozemoff's model, but for longer etch times the $1/t_{FM}$ relation broke down as the ion beam etching damage increased.

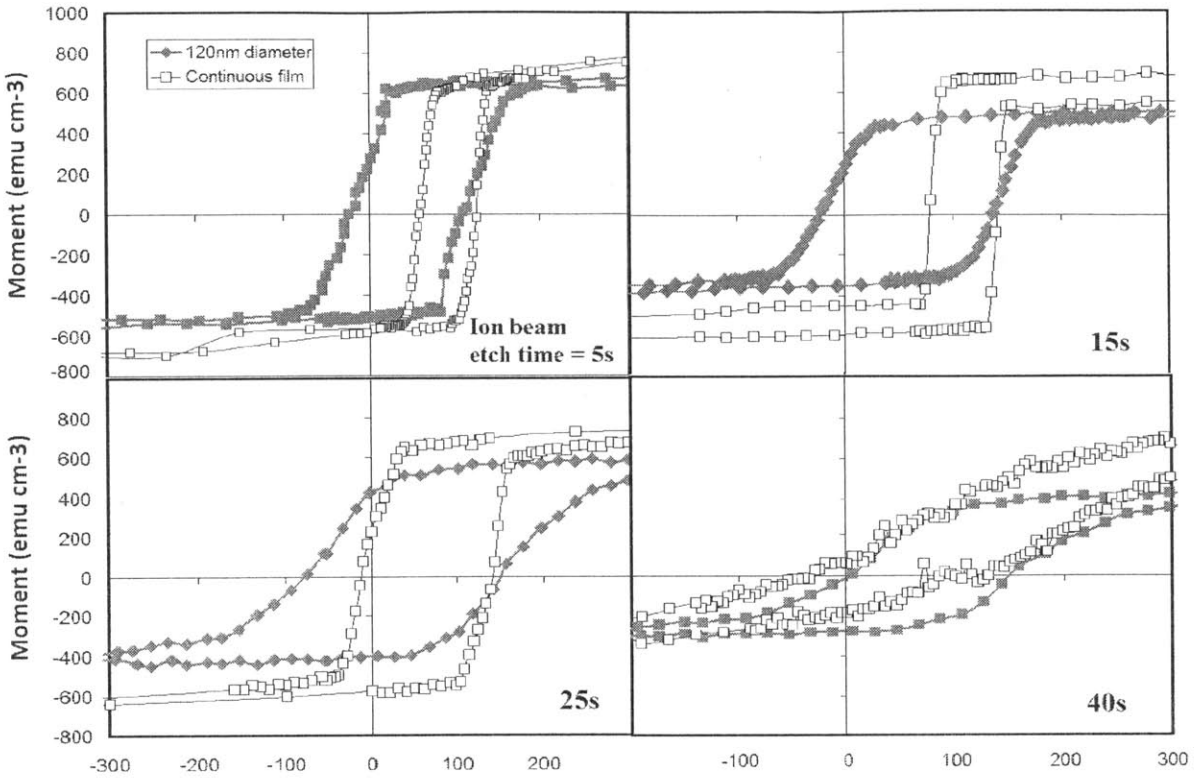

Figure 3.5: A comparison between hysteresis loops of 120 nm diameter dots and that of continuous films under different durations of ion beam etching time. The magnetization approached 800 emu cm^{-3} at saturation, above 3 kOe.

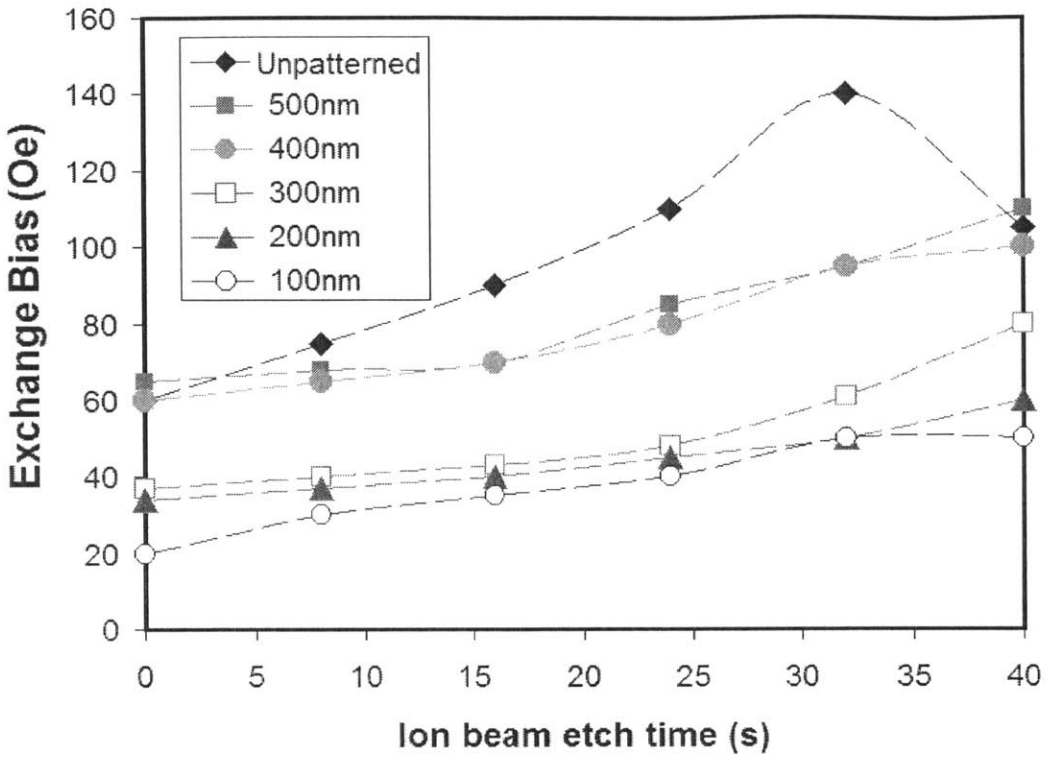

Figure 3.6: Exchange bias versus ion beam etch time for NiFe/IrMn dots of various diameters

3.3 Effect of Dot Diameter on Exchange Bias

Fig. 3.7 shows the effects of dot diameter on exchange bias. As the dot diameter decreased, exchange bias decreased for all ion beam etch times, i.e., for all NiFe thicknesses. Other studies have reported either an increase [76] or a decrease [77] in exchange bias on reducing the lateral dimensions of the nanostructures. Later on, Baltz et al. [41] showed that the size-dependent behavior of NiFe/IrMn bilayers depended on the thickness of the AF layer, which is one of the factors that determine domain size. Ultimately, the size-dependent exchange bias behavior in nanostructures is largely dependent on the AFM domain size.

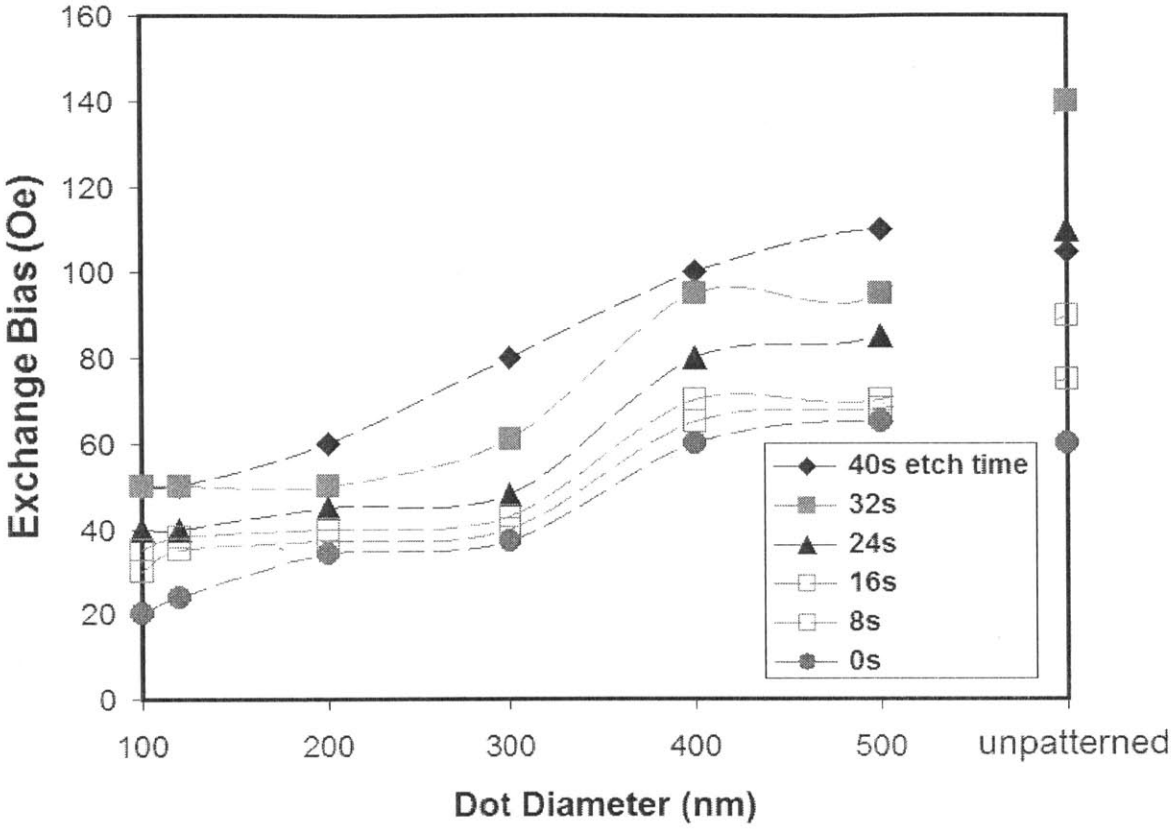

Figure 3.7: Exchange bias versus dot diameter for NiFe/IrMn dots subject to different ion beam etch times. Consistent irregularities near 300-400 nm are attributed to domain size confinement and the disappearance of vortex states.

3.3.1 Domain Size

The diameter L of the AFM domain is determined by a balance between the reduction in FM-AFM interfacial energy due to favorable local coupling between AFM and FM, and the energy penalty due to domain wall formation in the AFM. The analysis yields $L = \pi^3 J_{AF} t_{AF}/(2J_{FM-AF})$ for an unpatterned bilayer film with AFM film thickness of t_{AF}. Taking $J_{FM-AF} = 7.6 \times 10^{-15}$ erg and $J_{AF} = 16.1 \times 10^{-15}$ erg for the NiFe/IrMn system [78] gives an AFM domain size of 330 nm for $t_{AF} = 10$ nm, and a domain wall width $\delta_{IrMn} \approx \pi(A_{IrMn}/K_{IrMn})^{1/2} = 25$ nm [78]. We therefore expect that in our study, dots with diameter ~400 nm and lower are likely to have single

domain AFM layers. This would suggest that exchange bias should increase for smaller dots, according to both Malozemoff's and Mauri's models, but this was not observed, similarly to other studies [59, 12]. Reductions in exchange bias in nanoscale structures have been explained by the effect of lower coordination at the edges, or the role of defects in the AFM which weaken the pinning instead of promoting domain wall formation [41].

3.3.2 Vortex States

Next, we discuss the effect of dot size on the reversal mechanism of the FM. A transition from a remanent single domain state to a vortex state is expected as the dot diameter increases, and vortex states have also been seen in exchange biased nanostructures [77]. Reversal via a vortex state is characterized by an hour-glass shaped hysteresis loop [79]. Fig. 3.8 (square dots) shows an example of a hysteresis loop obtained from an array of 400 nm dots without exchange bias. Such loops characteristic of a vortex state were found in all sizes of dots in control samples consisting of just a FM layer. This is expected, because a circular dot with lateral size larger than the exchange length will result in a stable vortex state to minimize stray fields [80], and studies have shown that for dots of diameter 100 nm and above, the vortex state is stable.

However, the vortex state in an exchange-biased dot is destabilized by the unidirectional exchange coupling which raises the exchange energy of the vortex state. This promotes a remanent single-domain state, though an applied field can produce a vortex. In exchange biased vortex dots, the vortex core is off-centered and the net exchange bias is expected to be lower [81]. Hysteresis loops characteristic of a vortex state were found in fewer than 25% of samples of exchange biased dots with diameters 200 nm and 400 nm, and in 50% of the 300 nm dot samples. Fig 3.8 (solid curve) shows an example of a hysteresis loop from an exchange biased sample of 300 nm diameter

dots which was characteristic of a vortex-mediated reversal. This may be compared with the hysteresis loops of arrays of 120 nm dots in Fig 3.5 which indicate single domain behavior.

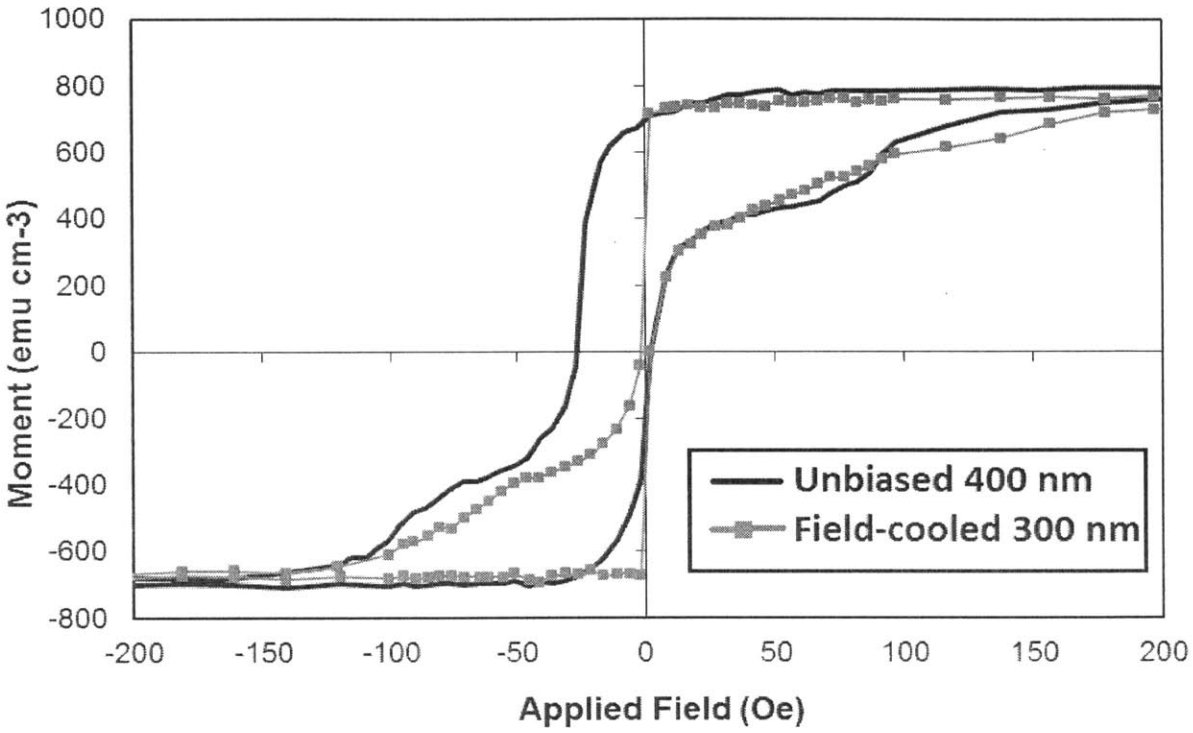

Figure 3.8: Hysteresis loop of an array of unbiased 400 nm dots with the FM layer ion beam etched for 5 s. This is compared to a hysteresis loop of an array of field-cooled 300 nm dots with the FM layer ion beam etched for 5 s. The shape of both loops is characteristic of reversal via a vortex state.

3.3.3 Training Effect and Blocking Temperature

It is also noteworthy that there was a significant training effect and reduction in exchange bias in the dots with multiple cycling, but no noticeable training effect in unpatterned films, regardless of ion beam etching. Resetting the exchange bias using field cooling restored the initial exchange bias value for all samples. The observed training effect for 100 nm dots made in a one-step process and field cooled is shown in Fig 3.9. The training effect is caused by rearrangements of interface

spins towards an equilibrium configuration, and it is known that systems with smaller AFM grains show much larger training effects [82, 83]. Thus, for dots that are small enough to limit the AFM domain size, a larger training effect is expected, which agrees with the observation that there was a more pronounced training effect for the smallest dots. In addition, the observed blocking temperature for 100 nm dots was 440 K, whereas that of the continuous film was 520 K. This reduction in blocking temperature is also consistent with the observation that the Néel temperature of an AFM decreases with decreasing lateral dimensions [30]. Furthermore, the blocking temperature reduction indicates that thermal effects are greater in nanostructures compared to continuous films and partially explains the reduction in exchange bias with decreasing feature size, even though the models predict the opposite.

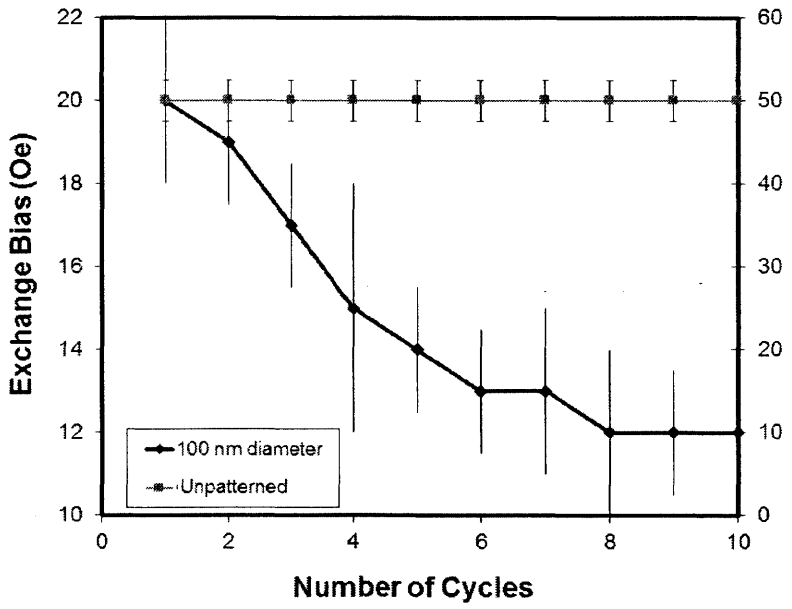

Figure 3.9: Training effect in 100 nm diameter dots made in a one-step process with no ion beam etching. There is no visible training effect in the continuous bilayer film.

3.4 Summary

A modification of the hybrid fabrication process described in section 2.1.6 was used to form large area arrays of exchange biased circular dots with diameter 100–500 nm and periodicity 2.5 times the diameter. For samples in which ion beam etching removed up to ~5 nm of NiFe, the exchange bias increased as ion beam etch duration increased in accordance with the inverse thickness relationship expected between ferromagnet thickness and exchange bias. However, longer etch times degraded the exchange bias as the film damage and roughness increased. The exchange bias decreased and coercivity increased as the feature size decreased. There was evidence of reversal via vortex nucleation and propagation in unbiased arrays and in some of the exchange biased arrays. Smaller diameter dots showed an increased training effect and lower Neel temperature. For the IrMn AFM used, the antiferromagnetic domain size was predicted to be 330 nm, but exchange bias continued to decrease as the dot diameter decreased below this value, as seen in other studies but counter to the prediction of the Malozemoff model.

The two-step deposition-etching-deposition process demonstrated here can therefore be used to produce exchange-biased nanostructures whose behavior as a function of NiFe thickness and dot diameter has close parallels with the behavior of samples produced by a single-step process. This indicates that the etch and redeposition process produces a FM-AFM interface with properties similar to those formed by a continuous deposition process. Although the method was demonstrated here for samples in which the FM and AFM layers had the same lateral dimensions, it is applicable to making structures in which biasing only part of the FM is required. For example, continuous NiFe films with stripes of IrMn show hysteresis consistent with different switching behavior of biased and unbiased regions of the NiFe, and will be described in chapter 4. In addition,

the fabrication and properties of structures resembling magnetic memory cells consisting of FM wires with exchange biased pads are described in chapter 5.

Chapter 4

AFM Stripe Grating on Continuous FM Film

In chapter 2, we presented a hybrid fabrication method that combines the benefits from all the commonly used patterning procedures. In chapter 3, we showed the effect of the ion beam etch step of the fabrication on magnetic properties of nanodots, and demonstrated that the fabrication method can be used to produce a FM-AFM interface with properties similar to those formed by a continuous deposition process. In this chapter, we once again modify the fabrication method to create an array of IrMn stripes on top of a continuous NiFe film, as shown in Fig. 4.1. This geometry is of particular interest because unlike patterns that can be made using one deposition step, there are magnetically different regions that can interact with each other, and the strength of each interaction depends on feature size differently, resulting in complex switching behavior and loop shapes [49, 64]. More importantly, read head and MRAM devices, as well as newer proposed domain logic devices [24] more closely resemble this type of structure in which bands of unpinned FM may interact with blocks of exchange biased FM. Understanding and manipulating the reversal process of a magnetic film with local exchange bias is, therefore, a key part of magnetic device design, providing, for example, the ability to trap a domain wall or to initiate reversal in a magnetic nanostructure. However, despite its importance, the behavior of magnetic films patterned with submicron antiferromagnetic features and how the regions interact at smaller dimensions has not been explored.

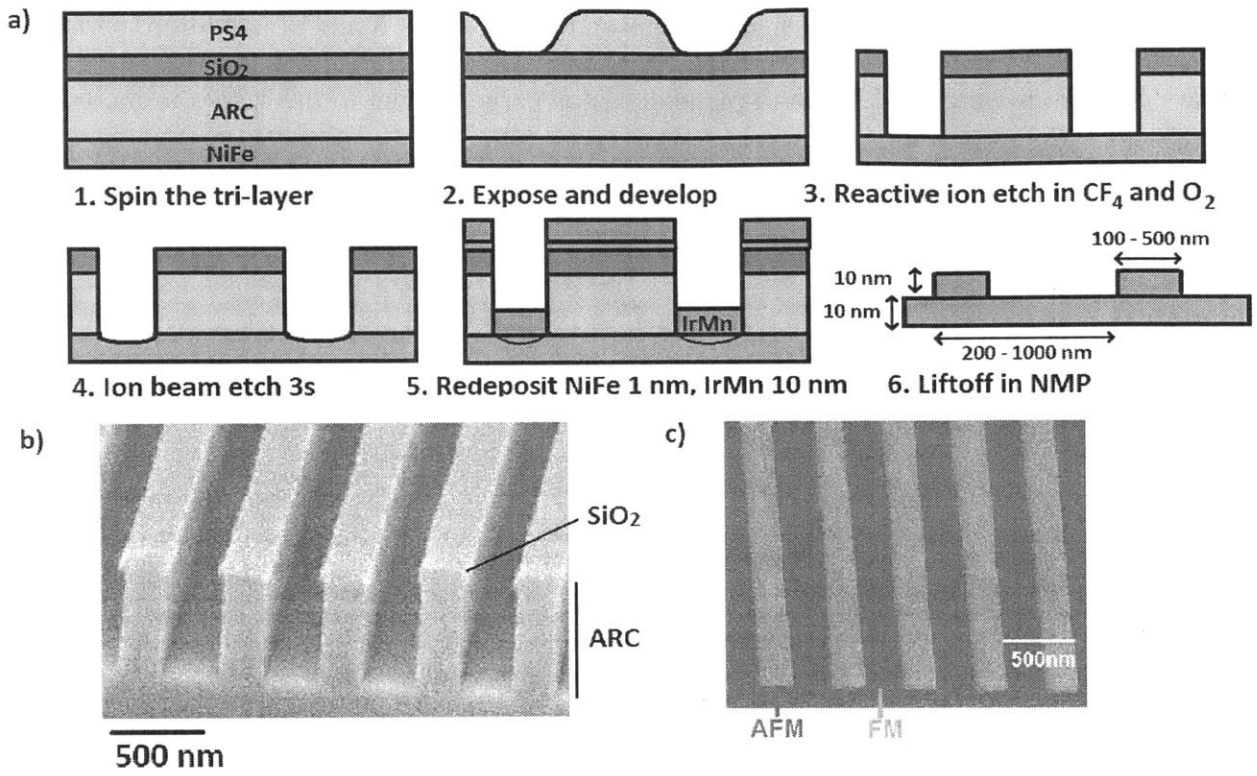

Figure 4.1: (a) Schematic of the fabrication procedure used to create AFM stripes on top of continuous FM. In steps 1-3, the resist mask is made on top of a continuous NiFe layer. In steps 4-6, the AFM is patterned. (b) SEM image of a resist mask with period 500 nm. (c) SEM image of a patterned sample with period 500 nm showing IrMn stripes of width w separated by regions of unbiased NiFe of width s.

4.1 Exchange Bias Parallel to Grating

In this section, we discuss the experimental results for samples with exchange bias and applied field parallel to the IrMn stripes, with s (the width of the unbiased regions of NiFe) and w (the width of the biased regions of NiFe) in the range of 100 to 500 nm. Then, we compare them with the corresponding micromagnetic simulations. A damping factor of 0.5 was used for fast convergence. Based on [30], a saturation magnetization, M_S, of 800 emu cm^{-3}, exchange stiffness, A, of 1.3×10^{-6} erg cm^{-1}, and an anisotropy energy of 8000 erg cm^{-1} were used. Because the exchange length of NiFe can be calculated from its other parameters: $l_{ex} =$

$\sqrt{A}/M_s\sqrt{2\pi} \approx 5.7$ nm [84], the cell size was chosen to be $5 \times 5 \times 5$ nm^3, In addition, periodic boundary conditions were used in the in-plane direction perpendicular to the stripes to model an infinite stripe array, while the simulation size in the direction parallel to the stripes was set to 2 μm to minimize the influence of edge effects.

4.1.1 Experimental Results

With both the exchange bias and applied field set parallel to the IrMn stripes, at small w and s, the hysteresis loops show a single step [Fig. 4.2(b)], but as the dimensions increase, the loops show two steps attributed to the switching of the pinned and unpinned regions of the film [Figs. 4.2(c)–(e)]. The criterion to identify a two-step reversal is the existence of a kink or plateau on at least one branch of the hysteresis loop occurring at a magnetic moment close to the value expected from the relative widths w and s of the stripes. In some cases, the plateau is only evident on one branch of the hysteresis loop, as in Fig. 4.2(c), because on the other branch, the offset of the loop due to exchange bias is counteracted by an increase in coercivity. The type of hysteresis loop of all the samples is plotted on a phase diagram, Fig. 4.2(a), showing a region of one-step reversal for values of w and s below 300 nm; i.e., for these dimensions, the pinned and unpinned regions reverse within a few Oersteds of each other. In the samples that show two-step reversal, we expect the magnetization at the plateau to be simply related to the ratio of s and w. For example, in Fig. 4.2(c), the geometry of the sample (w = 200 nm, s = 300 nm) suggests the first step of the descending branch of the hysteresis loop will correspond to 0.6 of the total change in magnetization. However, the measured step height is 0.67; i.e. the effective width of the pinned region is 167 nm. This effective width is consistent with part of the pinned region, in this case 17 nm, reversing with the unpinned region due to exchange coupling in the NiFe film. Samples with other dimensions show similar results with the effective width of the unpinned region given by the nominal width plus 15

nm ± 2 nm. The cause of this discrepancy is better explained in section 4.1.2 below using micromagnetic images.

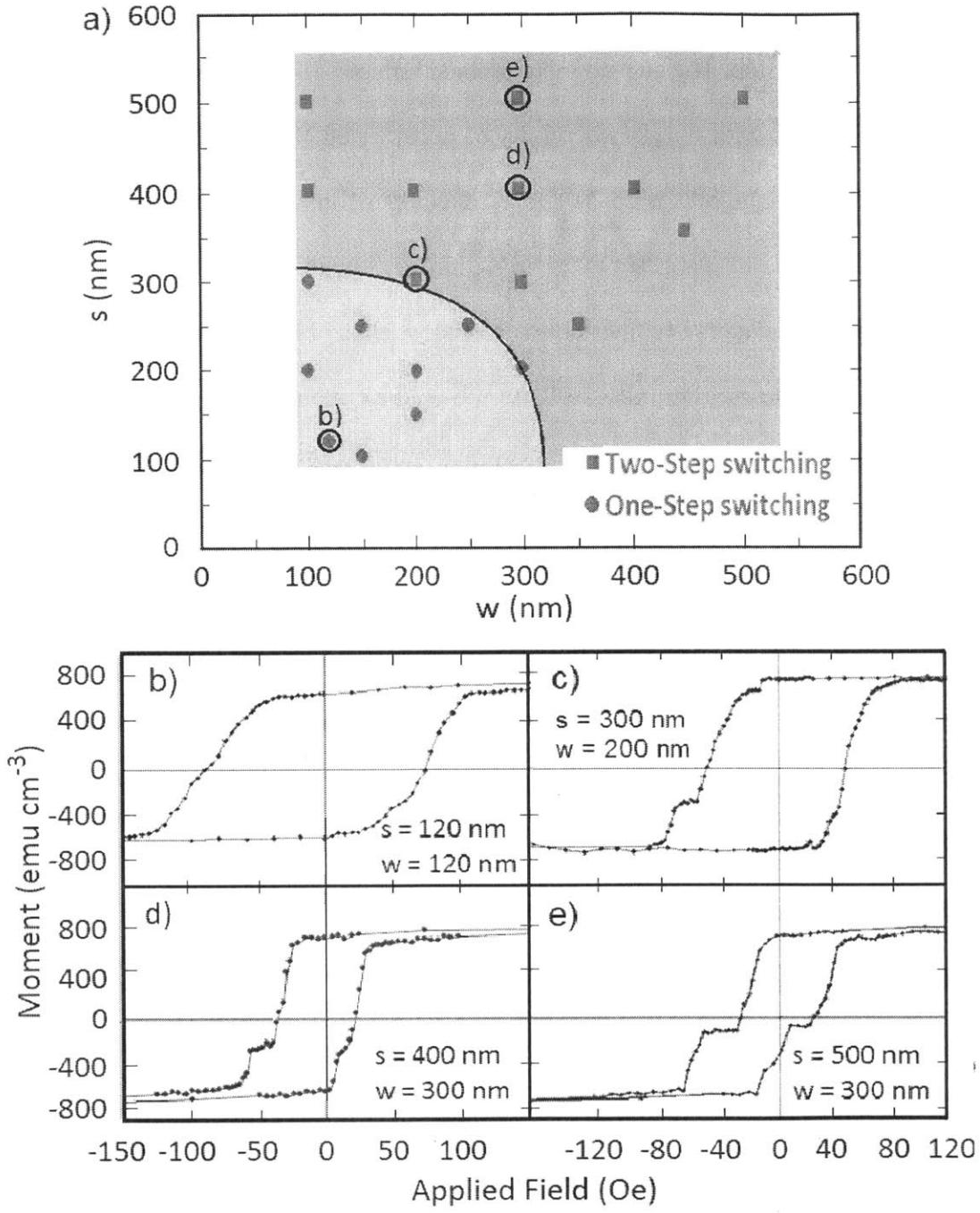

Figure 4.2: (a) Experimental phase diagram of the switching behavior. (b) An example of one-step switching, for s = w = 120 nm. Examples loops for two-step switching: (c) s = 300 nm, w = 200 nm; (d) s = 400 nm, w = 300 nm; (e) s = 500 nm, w = 300 nm.

4.1.1.1 Competing Effects of Feature Size on Exchange Bias

Fig. 4.3 shows the trends in coercivity and exchange bias with pattern dimensions. The coercivity of two-step loops is defined as the field at which the unpinned region magnetization reverses, measured halfway up the step. The coercivity increases from 60 to 150 Oe as s decreases, but there is no systematic variation with w. The coercivity of unpatterned NiFe/IrMn samples varies from 100 to 170 Oe. The exchange bias is 25–70 Oe. As a comparison, unpatterned NiFe/IrMn bilayer films show exchange bias of 80–120 Oe. A reduction of exchange bias in patterned structures compared to continuous bilayers is consistent with other studies [41]. The exchange bias increases slowly with s. It shows little variation for 100 nm $\leq$ w $\leq$ 350 nm but is larger for w = 500 nm. We discussed in section 3.3 that a reduction of feature size can cause an increase, decrease, or no change in the exchange bias and that the magnitude of the exchange bias has been associated with the AFM domain size [41], which is limited by the size of the features in patterned samples. In our system, the 10-nm-thick IrMn is expected to have a domain size of approximately 320 nm [41], wider than the narrowest values of w, suggesting that exchange bias will increase with decreasing w. In contrast, this competes with a variety of factors that lower exchange bias in nanostructures much more strongly than they do in continuous films. For example, thermal effects are greater in nanostructures, as seen by the increased blocking temperature with increasing size, ranging from 460 K for 100 nm wide lines to 520 K for 500 nm wide lines. In addition, features with narrower w are more vulnerable to thermal instability of the moments near the edges of the structures [22]. Furthermore, defects in the AFM that normally promote the formation of domain walls and serve to increase exchange bias in continuous films twist the spins in small structures in which forming a domain wall is energetically unfavorable, reducing the pinning strength instead [22].

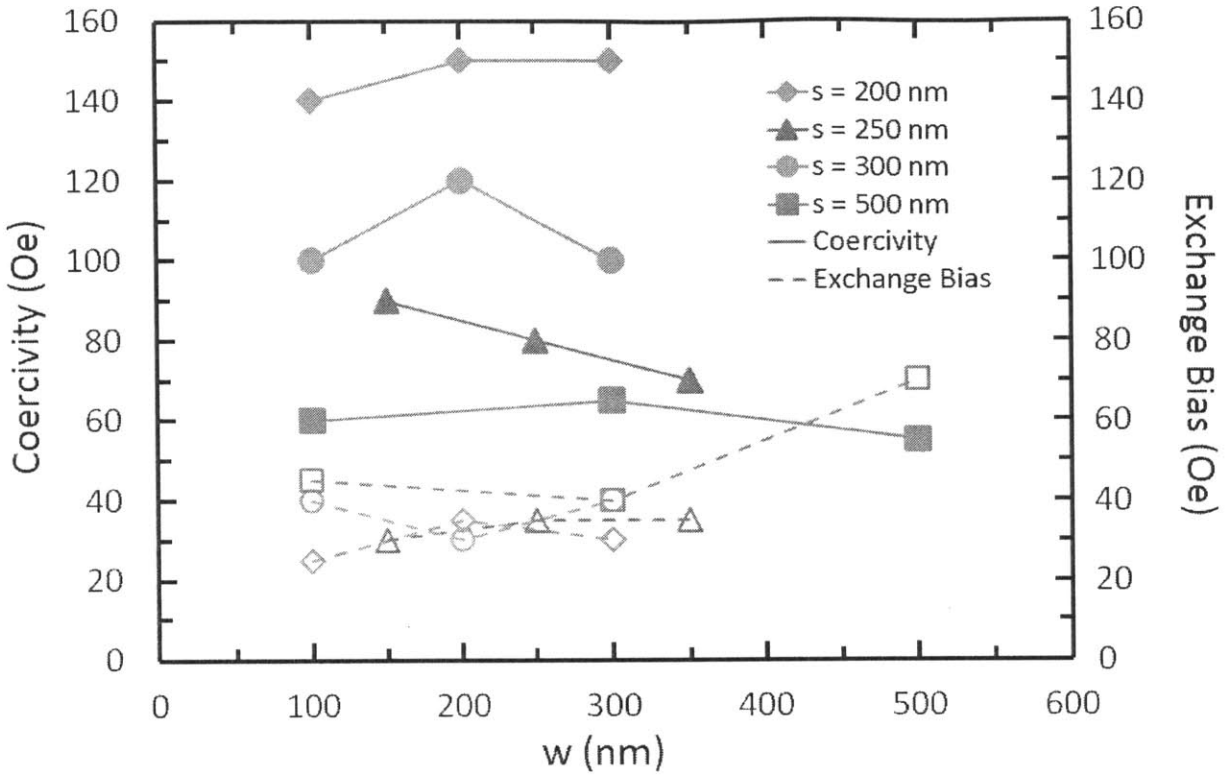

Figure 4.3: Measured exchange bias and coercivity versus IrMn stripe width *w* for four different values of *s*. For samples that show two-step switching, the coercivity is for the unpinned region.

4.1.2 Micromagnetic Simulation

To interpret the experimental results, micromagnetic simulations are performed with the magnetic field and the exchange bias of 100 Oe both parallel to the stripe length. Fig. 4.4 shows a unit cell used in the simulation. Each data point in the modeled hysteresis loops indicates the magnetization along the stripe length calculated after initializing the moments to random directions, then allowing them to relax in the corresponding applied field. This method is used to produce ground-state magnetization configurations as a function of field. Calculations in which the magnetic configuration is allowed to evolve as a function of field without reinitializing moment at each

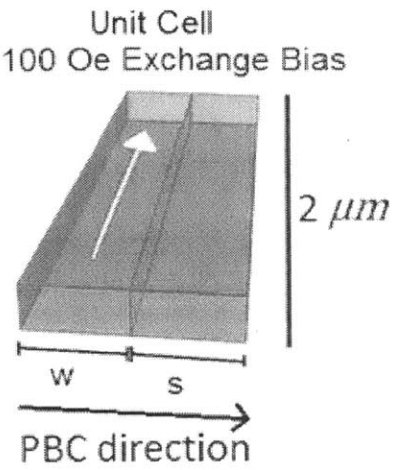

Figure 4.4: Schematic of the unit cell for the micromagnetic simulation. Exchange bias is set to 100 Oe, aligned parallel to the AFM stripes. The unit cell repeats itself in the PBC direction.

field step lead to very high switching fields due to the high symmetry and the periodic boundary conditions, trapping metastable configurations. This behavior is the case even when notches, a field offset of 2°, or a spread in magnetic anisotropy between cells is introduced. Examples are shown in Figs. 4.5(b)–(e) for several combinations of w and s. For smaller dimensions, the magnetization in the relaxed state is aligned along either +y or −y with high remanence [Fig. 4.5(b)], but for larger dimensions, a limited range of fields produces a state in which the magnetization of the pinned and unpinned regions of the NiFe is antiparallel, and the net magnetization takes an intermediate value [Figs. 4.5(c)–(e)]. These cases represent one-step and two-step reversal, respectively. Figure 4.5(a) shows a phase diagram that summarizes the results as a function of s and w. The phase boundary between one-step and two-step reversal is labeled T_1 and resembles the experimental results, Fig. 4.2(a). For two-step reversal, the value of magnetization at the plateau is field-dependent, showing that the width of the reversed region does not simply correspond to the width of the unpinned region but increases with increasing field.

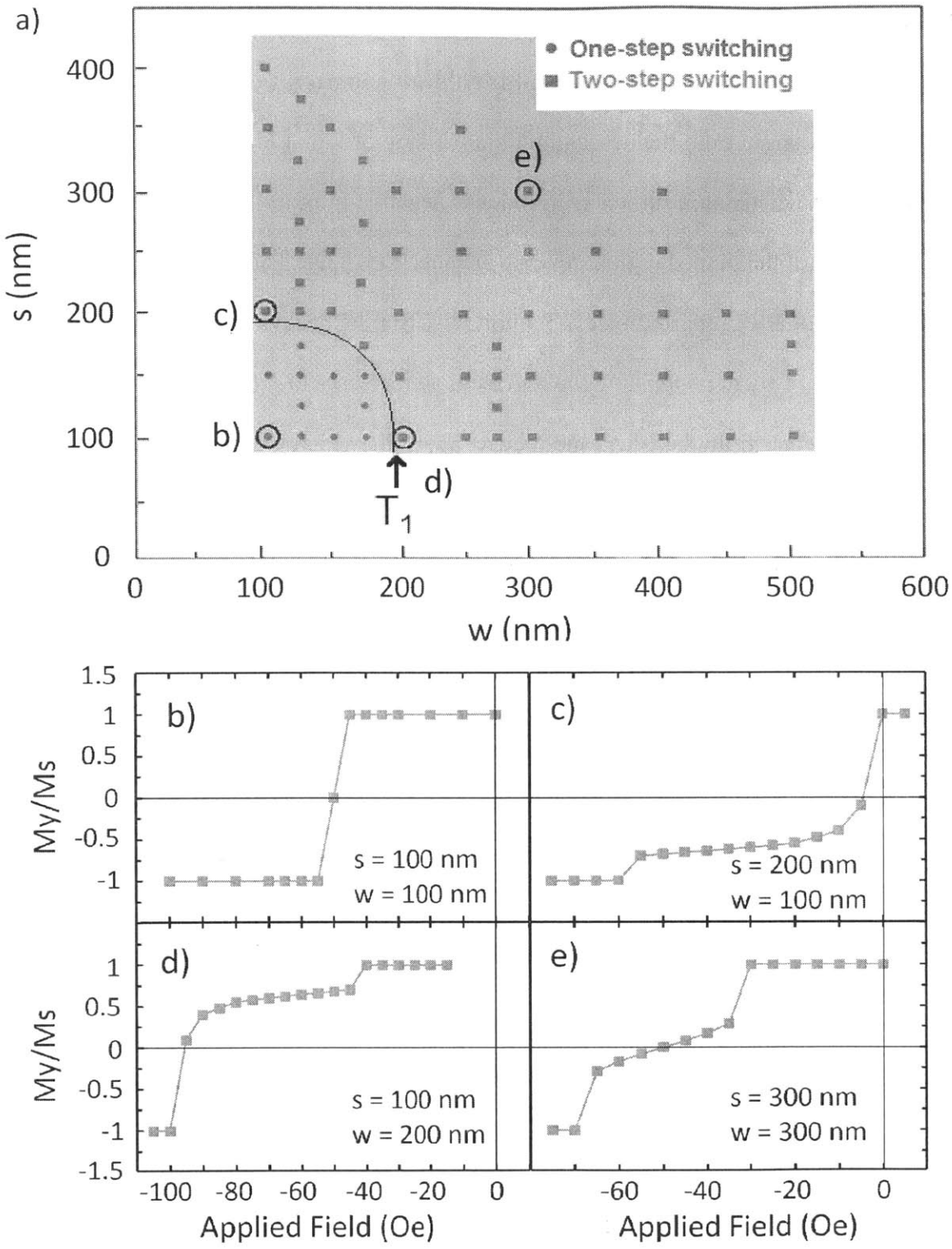

Figure 4.5: (a) Phase diagram for switching behavior of the patterned structure with both exchange bias and applied field parallel to the stripe length. T_1 indicates the phase boundary. (b) An example of one-step switching, and [(c)-(e)] examples of two-step switching. The dimensions correspond with the points labeled (b)-(e) in the phase diagram.

4.1.2.1 Switching Behavior: Competing Magnetic Interactions

The reversal process can be seen in more detail from the micromagnetic configurations vs field. Fig. 4.6 shows an example from the descending branch loop of Fig. 4.5(c) (w = 100 nm, s = 200 nm) with positive magnetization direction in red and negative in blue. The unpinned region, as well as 14 nm width of the pinned region, reverse in panel 2 at -5 Oe. This distance is about twice the exchange length of NiFe (approximately 5.7 nm) [84]. Similar behavior is seen for other model geometries exhibiting two-step loops. As the reverse field increases to -55 Oe, panel 3, the pinned region gradually reverses from the edges and reduces in width, with reversal completed at -60 Oe, panel 4. In contrast, complementary behavior is seen in simulations with w > s, as shown in Fig. 4.7 for w = 200 nm, s = 100 nm. At the switching field of -45 Oe, only the center part of the unpinned region switches. Increasing negative fields lead to a gradual expansion of the reversed region and reversal is complete at -100 Oe. The pinning is simply modeled as a region subject to a different effective field. During the reversal, exchange coupling causes part of the narrower region to switch with the wider region. In the case of w = s, increasing the negative field first reverses the center of the unpinned region which expands into the pinned region as the field increases, and the midpoint of the plateau corresponds to zero net magnetization [Figs. 4.5(b) and 4.5(e)]. In contrast, for combinations of s and w within boundary T_1, both pinned and unpinned regions reverse together without the formation of 180° walls. As the exchange bias in the model decreases, T_1 moves to larger values of w and s.

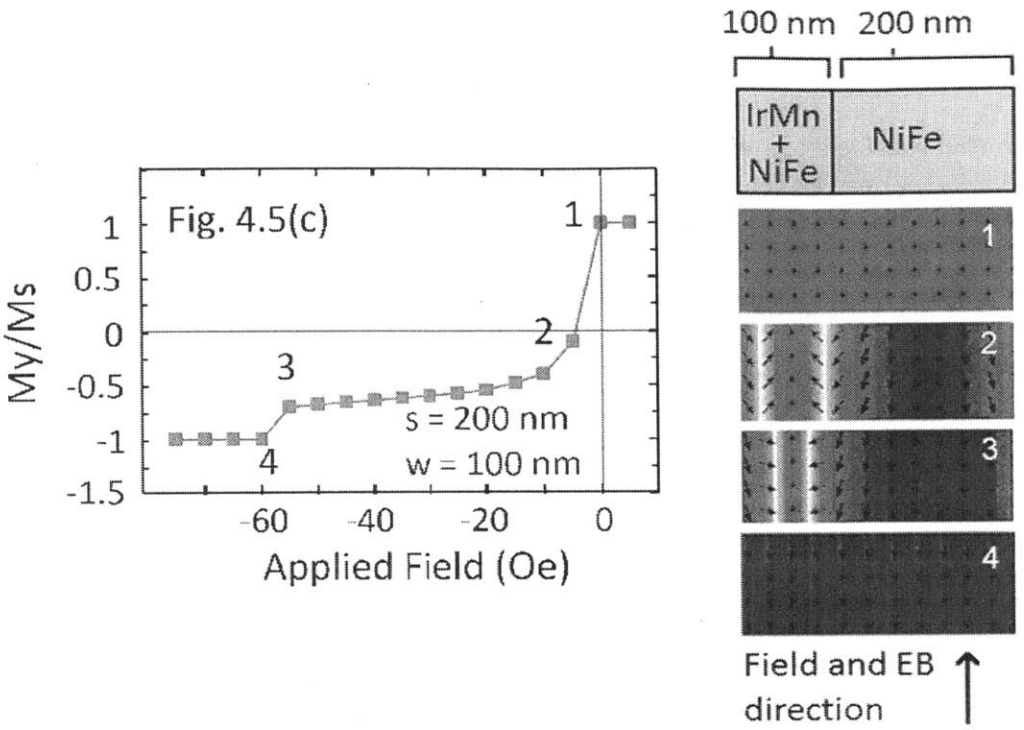

Figure 4.6: OOMMF micromagnetic images (right) under fields corresponding to Fig. 4.5(c) (repeated to the left for clarity), for s = 200 nm, w = 100 nm. Panels 1, 2, 3, 4 depict the equilibrium configuration at 0, -5, -55, and -60 Oe respectively.

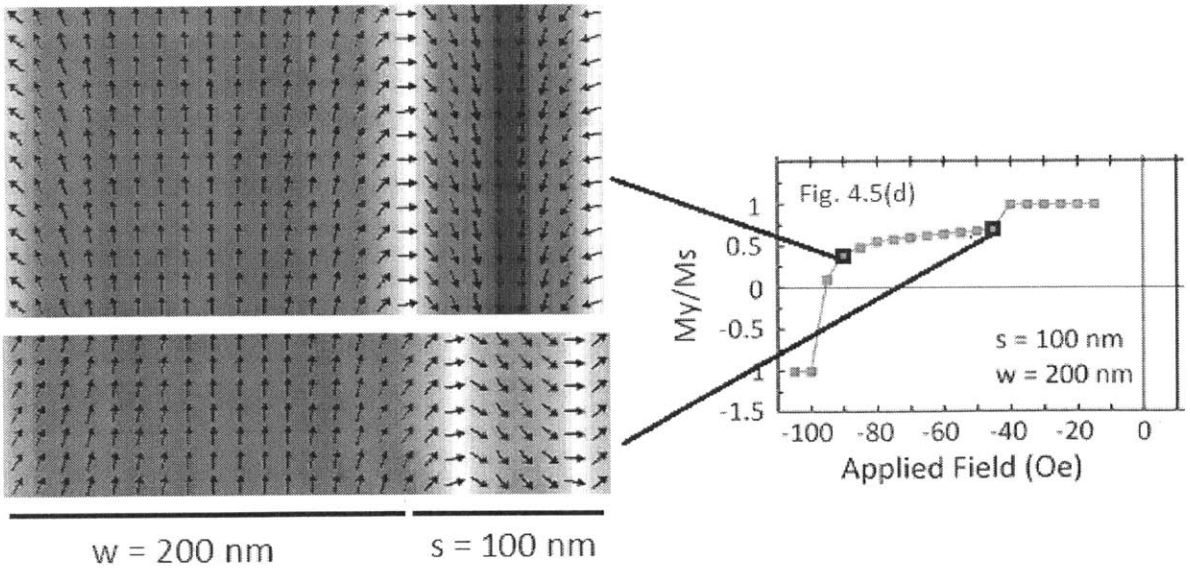

Figure 4.7: OOMMF micromagnetic images corresponding to Fig. 4.5(d) (repeated for clarity) at -90 Oe (top) and -45 Oe (bottom).

Figure 4.8 shows the change in T_1 with exchange bias. For example, when s = 200 nm, T_1 occurs at w = 100 nm for 100-Oe exchange bias and at w = 150 nm for 40-Oe exchange bias. The model, therefore, shows that one-step switching is promoted at lower stripe dimensions both by the increased energetic cost per unit area of forming the 180° domain walls and by the reduction in exchange bias in structures with lower dimensions. In contrast, at higher stripe dimensions, the Zeeman energy from the effective field during the switch wins over the lower energy cost of forming the domain wall. The agreement with the experiment is quite good considering the simplifications of the model, which include zero temperature, periodic boundary conditions in only one direction, and the treatment of exchange bias as a fixed Zeeman field in the film.

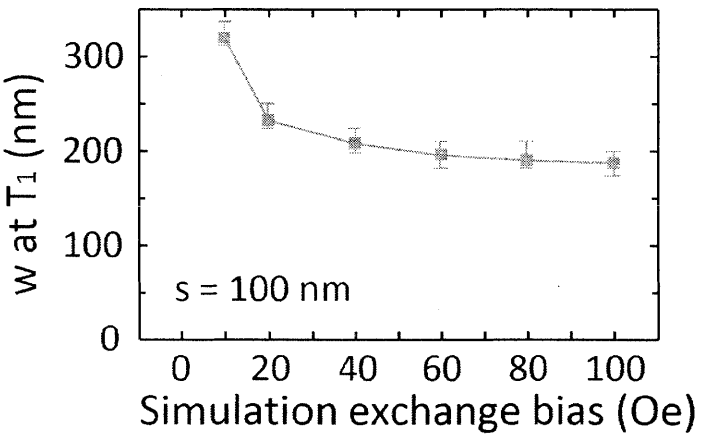

Figure 4.8: The values of *w* for *s* = 200 nm at the transition T_1 as a function of exchange bias magnitude. As exchange bias is decreased, one-step switching is more favored.

4.2 Exchange Bias Perpendicular to Grating

4.2.1 Experimental Results

When the field cooling and applied field are in plane, perpendicular to the stripe length, two-step switching is observed in samples with larger w and s, summarized in the phase diagram in Fig. 4.9(a). The boundary T_2 between one-step and two-step switching regimes occurs at higher w and s compared with T_1 described above for samples with exchange bias parallel to the lines. Moreover, the measured exchange bias in the two-step loops is 20 to 35 Oe, lower than for the parallel case (25 to 50 Oe). This result differs from a study of wider stripes [50], which observed no two-step switching, even up to 20- μm periodicity.

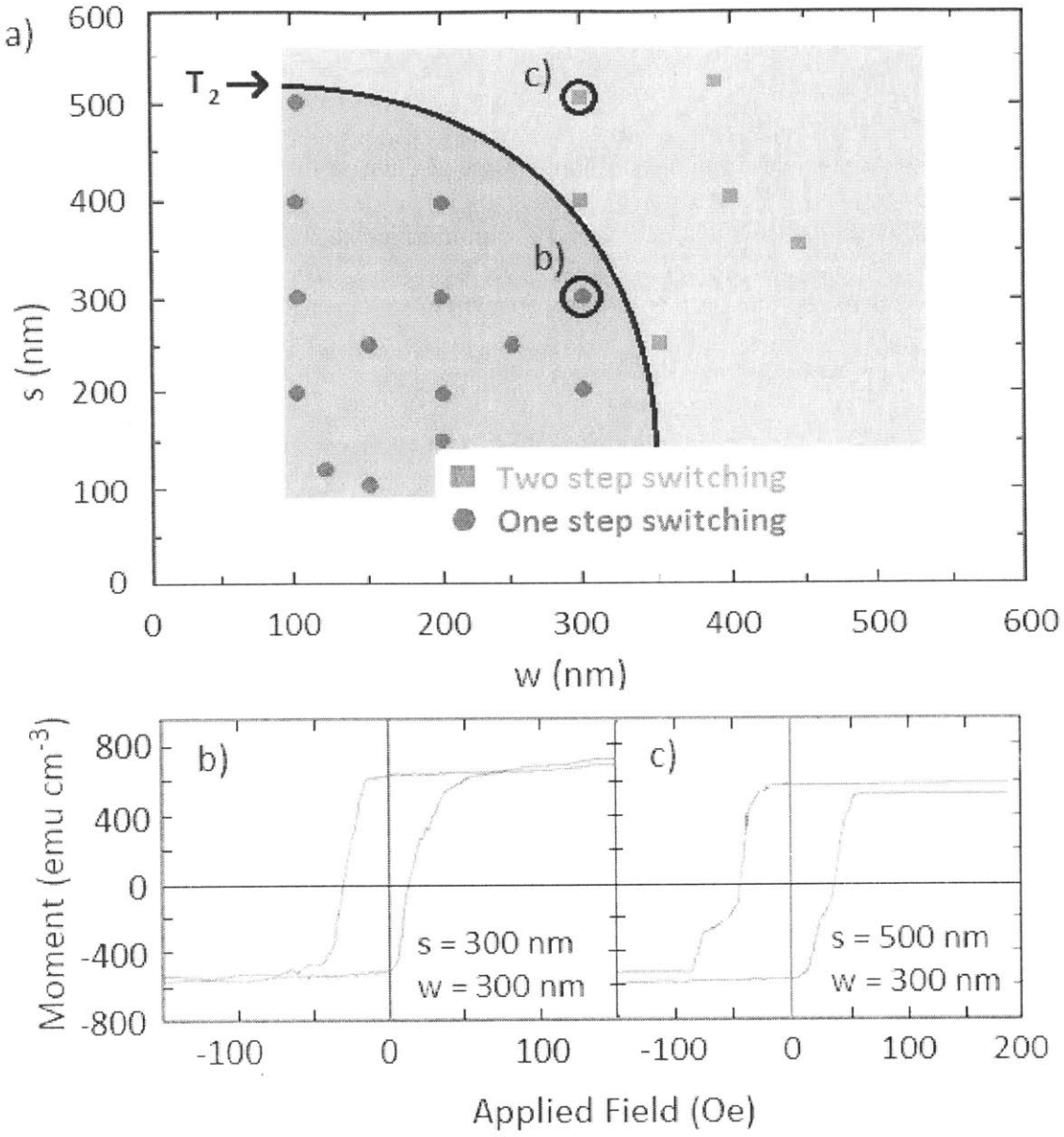

Figure 4.9: (a) Experimental phase diagram of the switching behavior in the samples exchange biased and measured perpendicular to the IrMn stripe length. (b) An example loop for one-step switching. (c) An example loop for two-step switching.

4.2.2 Micromagnetic Simulation

Unlike the experimental results, however, the simulations predict one-step switching for all combinations of w and s tested in the range of 100 to 500 nm [Fig. 4.10(a)]. This result is obtained for hysteresis loops calculated with no offset or with a 1° offset between the applied field and the direction transverse to the lines in order to break the symmetry of the simulation and also for relaxation from a random magnetization state. Images of the equilibrium magnetic configuration are shown at fields of −170 and −180 Oe, just below and just above the switching field [Figs. 4.10(c) and 4.10(d)], as well as a dynamic intermediate state calculated from the state at Fig. 4.10(c) by applying a field of −180 Oe with damping parameter $\alpha = 0.01$. The switching proceeds incoherently with the unpinned region reversing first, producing a head-to-head 180° domain wall. A larger simulation with an increased exchange bias of 1000 Oe and $s = w = 2000$ nm produces two-step switching, which shows that for sufficiently large exchange bias and wire widths, two-step switching can take place. However, for the smaller dimensions and lower exchange bias in Fig. 4.10(a), the energetic cost of the head-to-head 180° domain walls, which have greater stray field and greater width than the walls formed when the exchange bias and field are parallel to the stripes, preclude two-step reversal in the model. In comparison, 30-nm NiFe patterned with (2–20)-μm IrMn stripes [50] shows only single-step reversal for exchange bias and field perpendicular to the stripes. The lack of two-step switching is attributed to the interstripe extension of domain walls and overlapping tails of the Néel walls. Furthermore, the greater thickness of the NiFe (and, hence, the domain-wall size) and the modest exchange-bias values (a few Oersteds) will promote single-step switching behavior at much larger stripe dimensions.

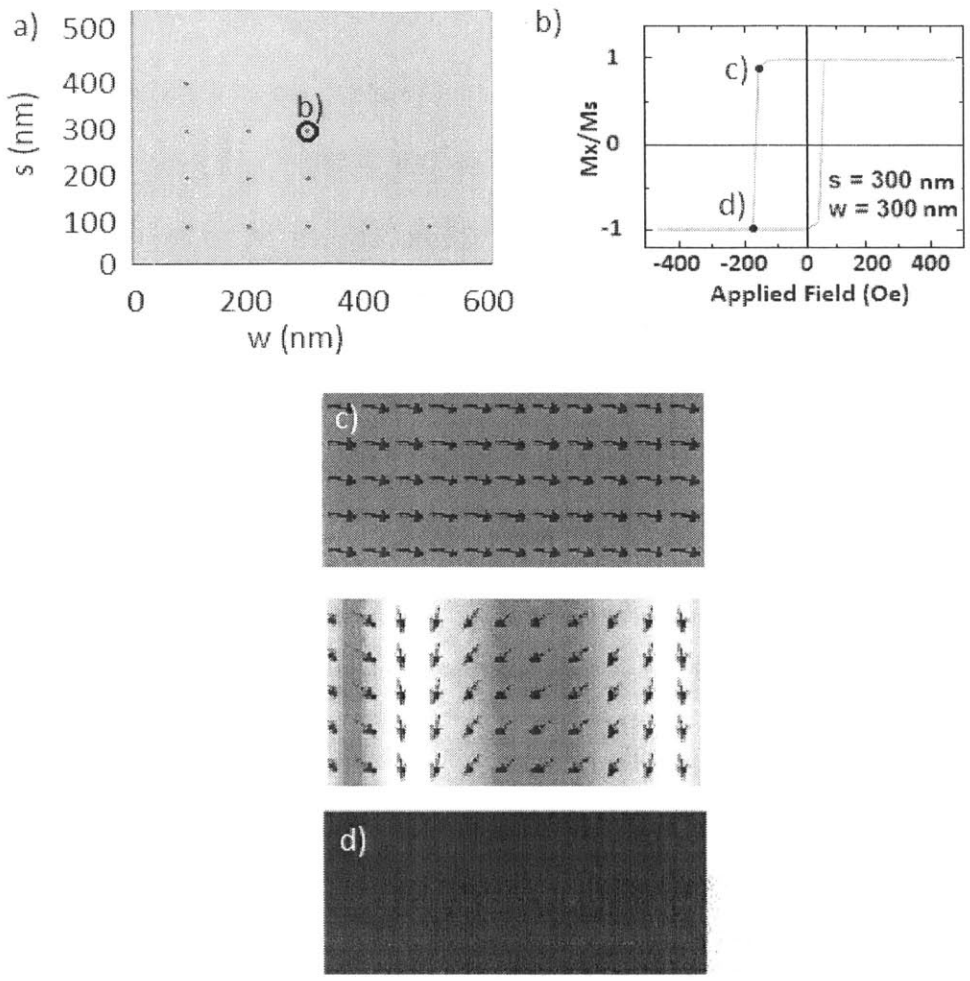

Figure 4.10: (a) Phase diagram for switching behavior of the patterned structure with exchange bias in plane along x, perpendicular to the wire length. All the modeled dimensions result in one-step switching. (b) Example of a loop showing one-step switching. magnetic configurations are shown at 170 Oe before the switch (c), and at 180 Oe after the switch (d), along with an intermediate state calculated dynamically by applying a field of 180 Oe to (c). The figures represent 600 nm period.

4.3 Summary

Local exchange bias is obtained in continuous 10-nm-thick NiFe films overlaid with arrays of 10-nm-thick IrMn stripes. The samples are fabricated using interference lithography combined with an etch and sputter deposition process to yield stripe widths of 100–500 nm and periods of 240–1000 nm. The magnetic switching behavior is mapped out as a function of dimensions both

experimentally and by micromagnetic modeling. In the patterned samples, at low wire widths and spacings, the pinned and free regions switch together, but as the width and spacing of the wires increases, the pinned and unpinned regions reverse at different fields giving a two-step loop. Micromagnetic modeling provides insight into the reversal process, reproducing the change in reversal process with stripe width for exchange bias and field parallel to the stripes. However, the simulations predict single-step reversal for exchange bias and field perpendicular to the stripes unless the exchange bias and period are large.

These results apply to the operation of read heads and other spin valve devices, as well as domain wall devices. For example, the phase maps presented in Figs. 4.2 and 4.8 may be used to manipulate the reversal of the FM layer at the nanoscale, enabling even denser magnetic media. Furthermore, in domain wall devices, domain walls are usually pinned using notches [85]. However, this may also be accomplished by tailoring the size of exchange biased pads and the soft unpinned FM region of a domain wall device [24] according to the phase maps.

Chapter 5

The Double Grating Structure

In this chapter, we further extend our fabrication procedure towards more device-like structures, in which both in-plane directions are scaled down. We have described drastic changes in exchange bias behavior in chapter 1 as one dimension is scaled down to the micron level. We have also demonstrated in chapter 4 that exchange bias behavior, as well as the relative strengths of various magnetic interactions, change even further as the first dimension is scaled down to the nanoscale. In this chapter, we apply our fabrication procedure twice to form two perpendicular gratings—one containing the FM, and one containing the AFM. Although this type of structure resembles a row of magnetic devices on a FM wire, such as spin valve read heads, there have not been any investigations of the effects of scaling down exchange biased regions on FM wires.

We first outline the fabrication procedure used to create the double grating structure. We then show the switching behavior of such a system experimentally and discuss the relative impact of scaling down the AFM versus scaling down the FM. Next, we look at micromagnetic simulations to provide more insight into the state of the system during the switch. Finally, we further extend our study into more complicated systems, such as exchange bias in a material with perpendicular magnetic anisotropy. We also consider exchange bias as an alternative method to pin domain walls in domain wall devices.

5.1 Fabrication

The fabrication of the sample closely follows the procedure used in chapter 4. The procedure is repeated twice: first, to pattern a NiFe grating, and second, to pattern a IrMn grating oriented perpendicular to the former. A schematic of the process is shown in Fig. 5.1(a), and SEM images after the NiFe and IrMn gratings are completed are shown in Fig. 5.1(b) and (c) respectively. Residual ARC can be seen in Fig. 5.1(b) even after a lengthy liftoff procedure. However, this does not affect the second layer, as the RIE step removes any residual ARC on the surface of the NiFe. A clean SEM image free of residual ARC is achieved in Fig. 5.1(c) using a slightly modified trilayer resist described in Appendix B. A side view of the completed sample is shown in Fig. 5.1(d), giving a glimpse of the relative heights of the layers.

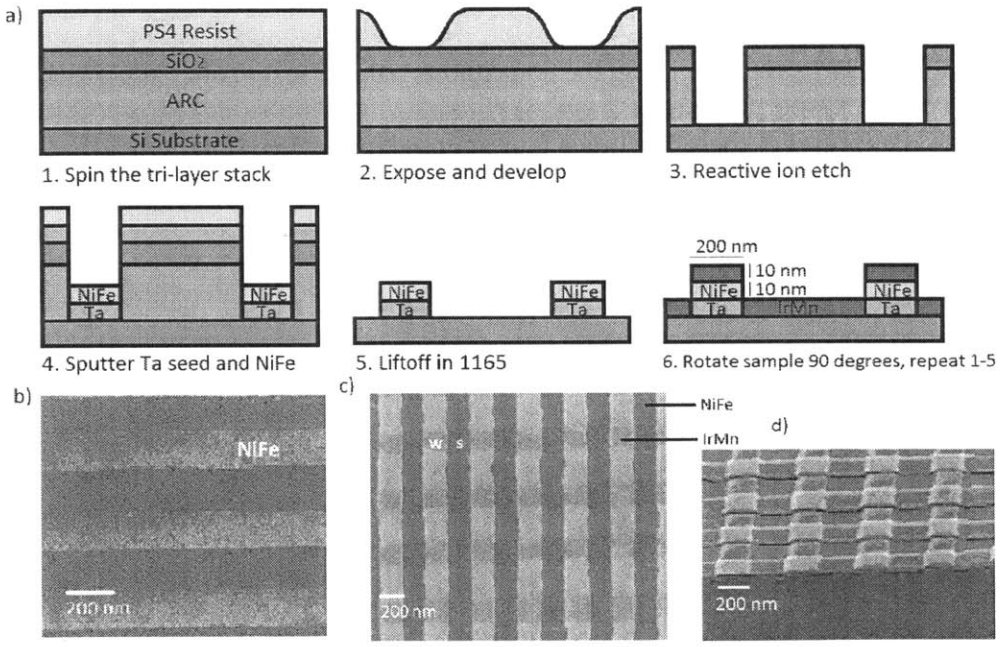

Figure 5.1: a) Schematic of the sample fabrication procedure. In steps 1-3, the tri-layer resist mask is made. In steps 4-5, the FM is patterned. In step 6, the AFM is patterned, with light ion milling and redeposition of NiFe prior to IrMn deposition. b) SEM image of a patterned FM grating with period 400 nm. c) SEM image of the patterned sample with both gratings present, showing the free regions of NiFe of width w separated by exchange-coupled regions of width s. d) Side view of the completed sample

5.2 Experimental Results

The hysteresis loops of the double grating structure for various combinations of IrMn wire width (w) and spacing in between the wires (s) are plotted in Fig. 5.2. The NiFe wires were kept at 200 nm width and 400 nm periodicity. It will be shown later that the exchange bias properties are hardly affected by the NiFe wire width and spacing. The loops were measured with the exchange bias and applied field direction set parallel to the FM stripes. In some of the loops, the exchange-biased region switches separately from the free region, whereas in other loops, both regions switch at once.

A map of the switching behavior is shown versus w and s in Fig. 5.2(a). Multiple points near the same w and s represent multiple trials on different samples with the same geometry. At large dimensions, the two regions switch separately, similar to the AFM stripes on continuous FM presented in chapter 4. However, unlike in the continuous NiFe case, the one-step switching regime is much larger, indicating that there are other interactions that make it energetically favorable for the two regions to switch together.

Fig. 5.2(e) shows an example of two-step switching for s = 540 nm, w = 460 nm. The position of the kink should geometrically be at 64 emu cm^{-3}. However, there is an offset, and the kink is actually at 105 emu cm^{-3}. This implies an apparent geometry of s = 565 nm, w = 435 nm, attributed to the same exchange-induced drag that governed the domain wall drag in the continuous FM samples. In other samples with two-step switching, this discrepancy was also found to be from 15 nm to 25 nm, which is also on the order of magnitude of the exchange length.

All of the hysteresis loops show a high switching field distribution. Usually, the larger the spacings in a sample, the less strongly the regions interact with each other, and the more switching field distribution there is [86], but this is not necessarily observed because larger dimensions are

also less prone to individual variances caused by edge effects, for example, from liftoff. The switching field distribution in these samples can sometimes make the type of switching unclear such that a sample which have separately-switching regions may appear to have one-step switching. If the exchange bias is low enough, and the switching field distribution is high enough, then the onset of the pinned region switching will overlap with the end of the free region switching, and the loop will appear to have no kink. This is seen in Fig. 2(a); at w = 460 and s = 540, two of the five samples show one-step switching.

The switching field distribution in small structures may arise from either reversible tilt from all the structures as the field decreases, or from the individual structures switching at slightly different fields due to variations from defects and other imperfections. The remanence and minor loops in Fig. 5.3 show that most of the switching field distribution is caused by the latter. In the remanence loop, when the field is allowed to return to zero, the moment is almost the same as if the field were present. Similarly, the minor loop does not return to saturation until the applied field is equal to the switching field, showing that the decrease in magnetization is due to a portion of the structures switching completely rather than all the structures having tilted spins. The spins in exchange biased structures are expected to resist tilt because the AFM provides the extra energy to the FM required to stabilize the magnetization in one direction [87].

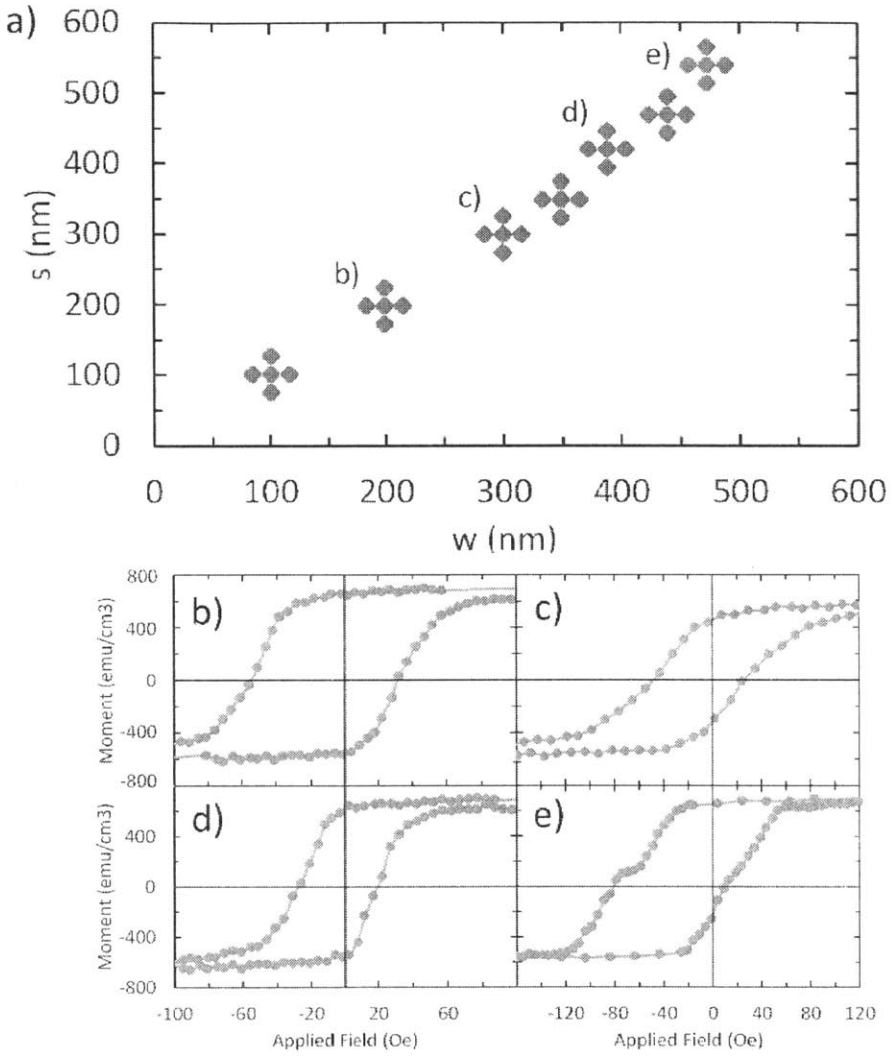

Figure 5.2: a) Experimental map of the switching behavior under various w and s. Clusters of points represent multiple samples of the same dimensions. Examples of one-step switching: b) s = w = 200 nm. c) s = w = 300 nm. d) s = 480 nm, w = 520 nm. e) An example of two-step switching for s = 540 nm, w = 460 nm.

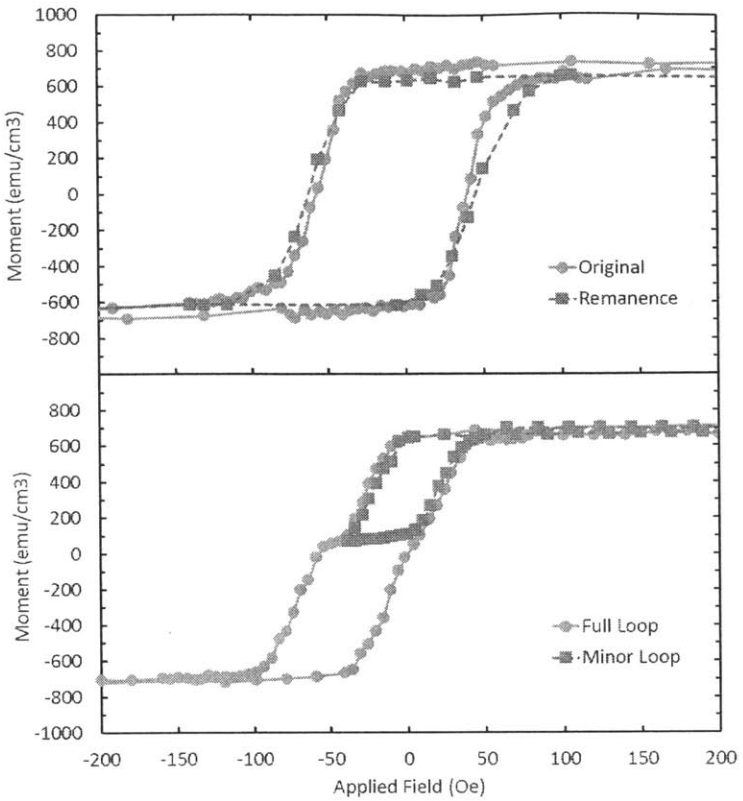

Figure 5.3: Top: Remanence loop for s = w = 200 nm. High remanence indicates that reversal is mostly irreversible, as opposed to having reversible tilt. Bottom: Minor loop for a two-step switch with s = w = 500 nm, confirming that reversal is irreversible.

5.2.1 Exchange Bias Trends

The trends in exchange bias and coercivity are plotted as a function of feature size in Fig. 5.4 for both the NiFe stripe width, and the IrMn stripe width. The exchange bias magnitude for all measured dimensions range from 10 Oe to 30 Oe, with a single outlier at 45 Oe. The exchange bias of the pinned region was calculated from one-step switching loops by assuming that the exchange bias in these loops is a geometric weighted average of the pinned and free regions, and extrapolating. These values are significantly lower than that of the continuous bilayer test sample, which showed 80-120 Oe of exchange bias. This agrees with most studies [88, 89]. There are several factors that would affect the exchange bias when dimensions are confined. If the structures

are small enough such that the AFM domain size is confined to a smaller size than is calculated from the AFM thickness, then the exchange bias should increase. For a thickness of 10 nm, the domain size is calculated to be 300 nm [41], and many of our samples were under 300 nm. However, this effect competes with various factors that lower exchange bias that affect nanostructures much more strongly than they do continuous films. As mentioned in chapter 3, thermal effects are greater in nanostructures, edges effects become prominent, and defects in the AFM that normally promote the formation of domain walls twist the spins in small structures in which forming a domain wall is unfavorable, reducing the pinning strength. However, there is an additional contribution to low exchange bias in the double grating structure. Even though the exchange biased portion of the NiFe wire is a small rectangle, the IrMn itself consists of stripes with regions of NiFe underneath. Therefore, unlike the dots from chapter 3, the AFM is allowed to have larger domain structures than the exchange biased regions. As a result, the AFM domain size is larger than they would be if they were confined rectangles, and the exchange bias is smaller.

More importantly, while the exchange bias decreases with decreasing width of the IrMn, the exchange bias shows no trend at all when the FM stripe width is changed with a fixed IrMn stripe width. This is because most of the effects mentioned that decrease exchange bias are dependent on the AFM, not the FM. Therefore, scaling down the AFM stripe width affects the exchange bias much more greatly than scaling down the FM stripe width does. This can potentially allow for extremely thin FM wires with relatively long AFM regions that show an exchange bias comparable to that of a continuous film.

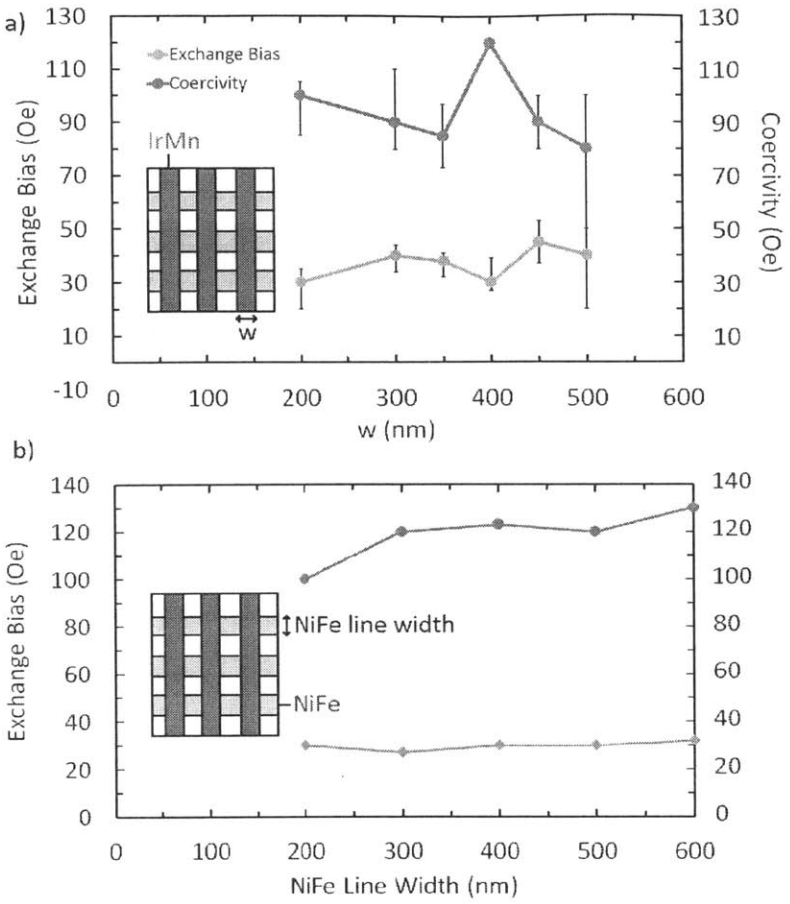

Figure 5.4: a) Measured exchange bias and coercivity versus w and s. b) Exchange bias and coercivity versus the NiFe width for w and s fixed at 200 nm. For samples in both (a) and (b) that show one-step switching, the exchange bias is extrapolated assuming the measured exchange bias is the weighted average of the two regions. The coercivity in the two-step loops is the coercivity of the pinned region.

5.3 Micromagnetic Simulation

To investigate the causes of the abnormally large one-step switching regime in Fig. 5.2(a), micromagnetic simulations were performed with the magnetic field and exchange bias direction parallel to the NiFe stripe length. The exchange bias was set to 100 Oe. Fig. 5.5(a) shows a schematic of the unit cell used, with periodic boundary conditions applied in the direction of the wire length. Fig. 5.5(b) shows a phase map that summarizes the simulated results as a function of

w and s. The phase boundary between the one-step and two-step regions is labeled T_1. At low w and s, there is one-step switching, and at higher w and s, there are stable states in the intermediate region, in agreement with the experiments.

Due to the simplicity of the exchange bias model used in the simulations, the agreement with experiment is qualitative, and the phase boundary is located at a much lower w and s. The reason can be seen in Fig. 5.5(c), which shows the boundary location with respect to w and s, as a function of exchange bias magnitude used in the simulation. As the exchange bias decreases, there is less Zeeman energy available to oppose one-step switching, and the boundary moves to larger values. Not only do the experimental samples exhibit exchange bias values much less than the 100 Oe used in the simulation, but as the dimensions decrease, the exchange bias also decreases, and if the exchange bias decreases, one-step switching is promoted based on Fig. 5.5(c). Therefore, the onset of two-step switching is expected to occur at a higher value than in the simulations.

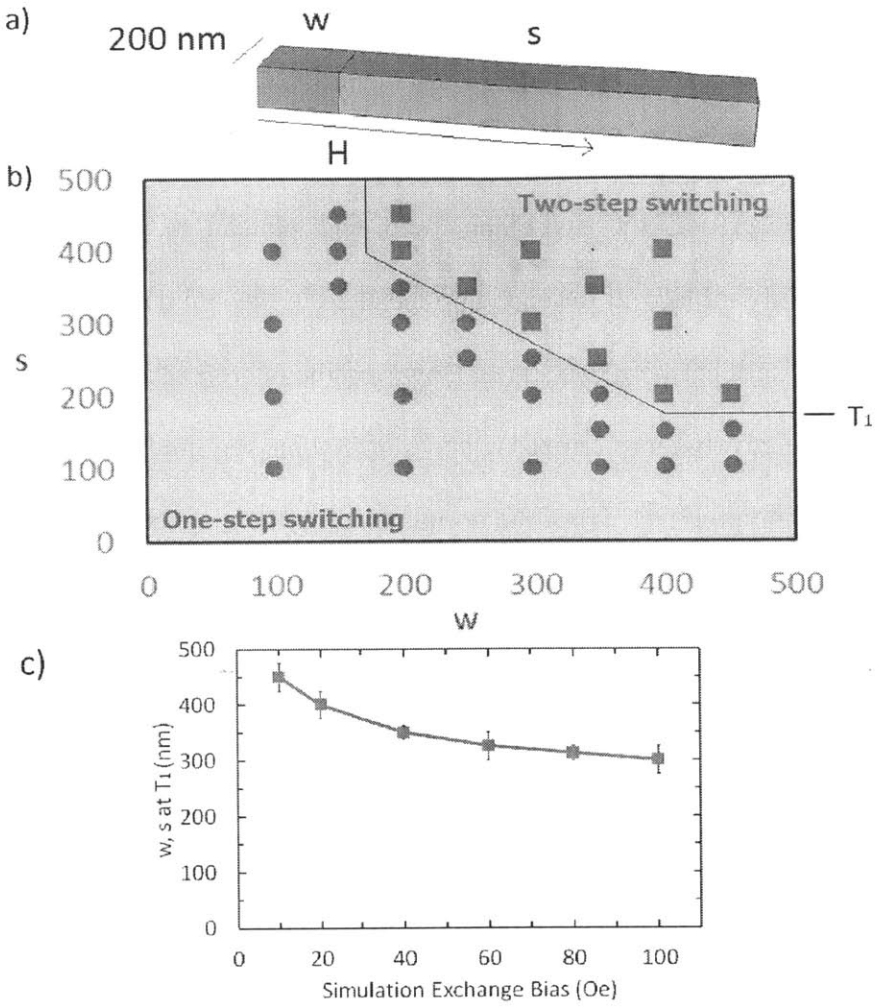

Figure 5.5: a) Schematic of the simulation. Applied field, exchange bias, and periodic boundary condition direction are all parallel to the NiFe stripes. b) Switching behavior phase map. Exchange bias and field direction parallel to NiFe stripes. T_1 indicates the phase boundary. c) Location of phase boundary T_1 as a function of simulation exchange bias for w = s.

When w and s are both above 200 nm, the condition for two-step switching appears to be that the total width of w + s must be greater than 600 nm. However, there is a minimum w below which two-step switching cannot occur, no matter how large s and exchange bias are; similarly, there is a corresponding minimum s. In the experiments, because the samples were made using interference lithography, it was extremely difficult to create a very small w while having a large s, and vice

versa. As a result, it was difficult to confirm this with experimental data. On the other hand, micromagnetic images were readily available.

Examples of a one-step switch and a two-step switch are shown in Fig. 5.6(a) and (b), along with micromagnetic images at the switching field and plateau respectively. Because the magnetization is randomly initialized for each applied field in the simulation, the stable state for the one-step switch was split between two states. However, the micromagnetic image in Fig. 5.6(b) shows why there is a relatively large critical w and s of 200 nm required for two-step switching. The full width half maximum (FWHM) of the domain wall in the magnetic stripe is calculated to be 120 nm. In contrast, the FWHM of a domain wall in a relaxed wire of the same width that is not subject to any exchange bias or Zeeman fields is 146 nm. This shows that in the exchange biased stripe that shows two-step switching, at the switching field, the domain wall contains energy due to bulk exchange in the FM. It is therefore extremely energetically unfavorable to squeeze two such domain walls into unit cells that have a small w or s. In such unit cells, even though the applied field decreases past the switching field of the free region, the Zeeman energy from the free and pinned region is not enough to overcome the energy penalty of having two domain walls inside the unit cell. In contrast, as dimensions increase, the energy penalty for having two domains walls within the unit cell decreases and the domain walls are allowed to form. Fig. 5.7 shows the progression of the two-step switching as dimensions are increased. As w and s increase, the plateau width increases because it becomes more and more energetically favorable for the domain walls to exist inside the unit cell, and the free region is allowed to switch and form the domain walls at fields closer to zero. In addition, the slope of the plateau increases slightly as well, because the total unit cell length increases at a much faster rate than the domain wall FWHM does.

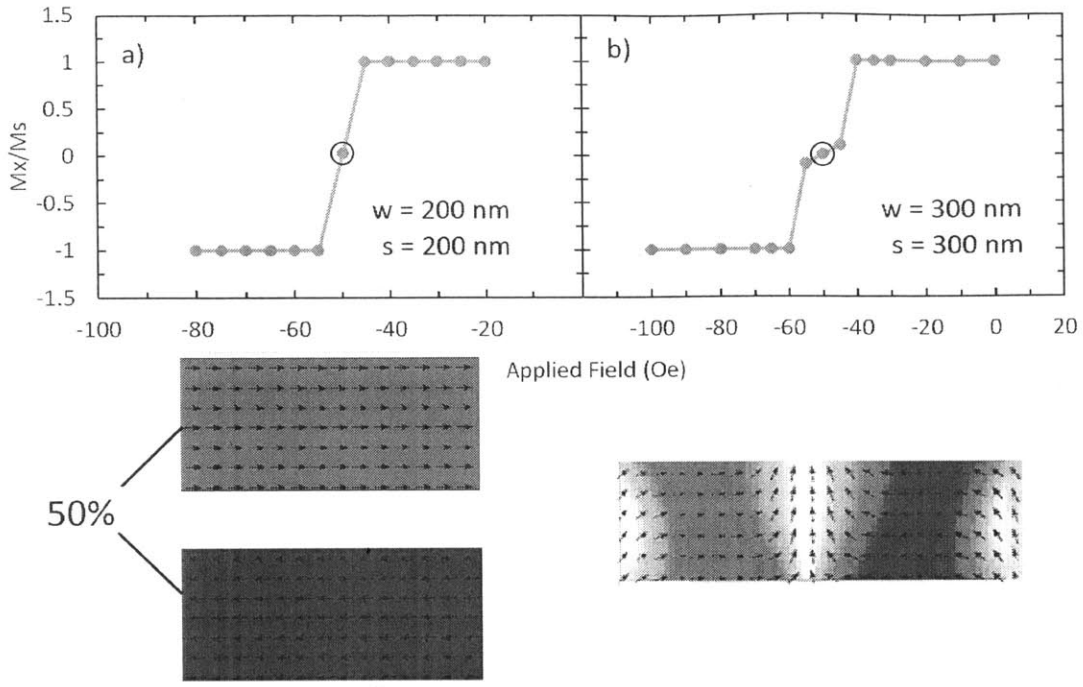

Figure 5.6: a) Example of one-step switching for w = s = 200 nm. b) Example of two-step switching for w = s = 300 nm. Micromagnetic images during the switch are shown below the plots. Because random initialization occurred at each applied field, the outcome of (a) at the switching field was split.

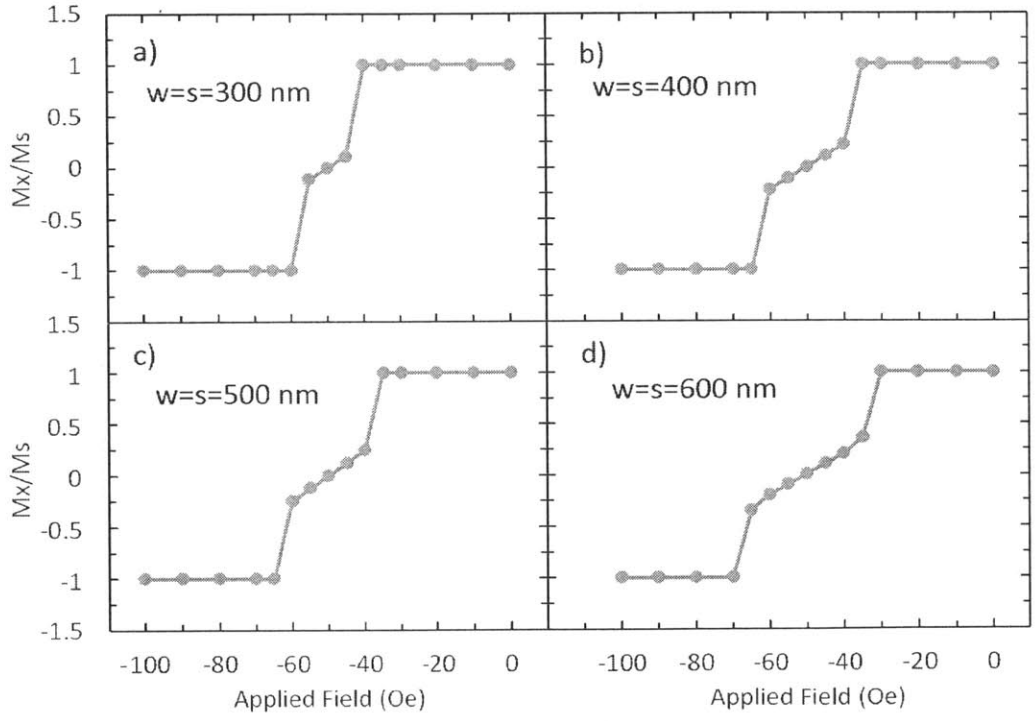

Figure 5.7: a-d) Progression of the two-step switching plateau as dimensions increase.

5.4 Exchange Bias with Perpendicular Magnetic Anisotropy

In this section, exchange bias in materials with perpendicular magnetic anisotropy will be discussed. Typically, exchange bias has been done in PMA materials using one of these multilayer structures: $[[\mathrm{FM/nonmagnetic}]_x/\mathrm{AFM}]_y$ or $[\mathrm{FM/nonmagnetic}]_x/\mathrm{FM/AFM}$, where x and y indicate a number of repetitions [90, 91]. In these structures, exchange bias depends on the interplay between the unidirectional anisotropy of the interface, the strength of the out-of-plane anisotropy of the PMA material, and the overall magnetostatic energy of the system. However, exchange bias involving a non-multilayer PMA material and a AFM has been largely unexplored.

5.4.1 Interactions between a PMA FM and an IMA FM

The magnetization behavior and magnetic anisotropy of a multilayer involving $[\mathrm{Co/Pd}]_5$ and NiFe was investigated [92]. The Co in each layer had a thickness of 0.5 nm, and the Pd had thickness of 1 nm for a total of 7.5 nm in the five multilayers. The thickness of the NiFe was varied from 0 to 80 nm in order to study the interplay between the PMA of the Co/Pd multilayer and the IMA of the NiFe film. The experimental measurements were done using magnetometry, MFM, and ferromagnetic resonance, and it was found that out-of-plane stripe domains that form in the PMA material transfer to the in-plane NiFe even for thicknesses up to 80 nm, as shown in Fig. 5.8. I performed the simulations using OOMMF to model how the NiFe, which usually has an in-plane anisotropy, behaves when exchange coupled to a PMA material such as Co/Pd.

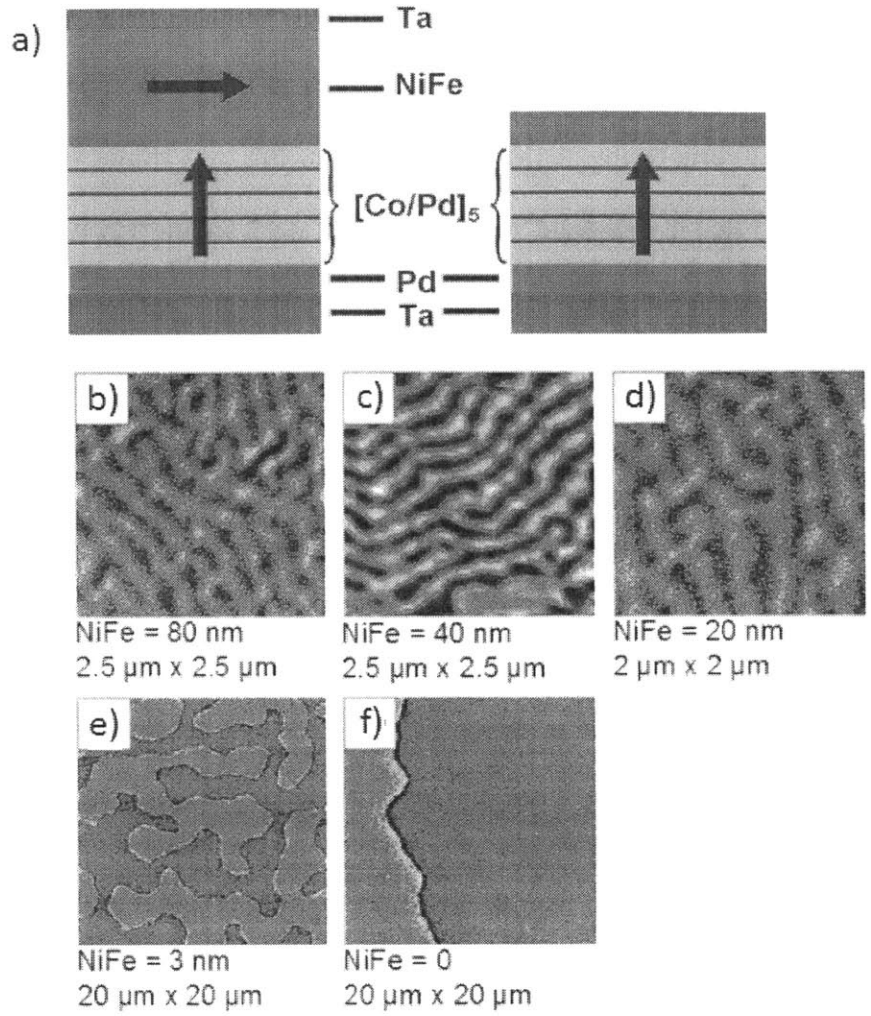

Figure 5.8: a) Schematic of the exchange-coupled multilayer structure. The film consists of in-plane NiFe and perpendicular $[Co/Pd]_5$. Figure adapted from [92]

A NiFe layer exchange-coupled to a $[Co/Pd]_5$ multilayer was modeled with NiFe thickness = 4, 20, and 80 nm, with periodic boundary conditions used in the x direction. The cell size was chosen to be 4 nm x 4 nm x 4nm, and the y-length was set to 1 μm to minimize boundary effects. The NiFe magnetization was initially randomized, and the system was allowed to equilibrate at zero applied field. Standard magnetic parameters were taken from literature [93], and the damping parameter was set to 0.5 to lead to rapid magnetic convergence.

Fig. 5.9 shows how the magnetic configuration at the top surface of the NiFe changes with increasing thickness. In the cross sections, the arrows represent the magnetization direction, and the colors represent the z-component of the magnetization. Fig. 5.9 shows out-of-plane stripe domains inside the NiFe that correspond to the domains seen in the Co/Pd multilayer. The simulations show that even for the 80-nm thick NiFe layer, there is contrast on the surface indicating presence of a domain structure, in agreement with the experiments. More importantly, for a NiFe thickness of 4 nm, the magnetic anisotropy of the NiFe layer is out-of-plane, showing that when a thin enough layer of NiFe exchange-couples with a PMA material, the NiFe becomes PMA as well.

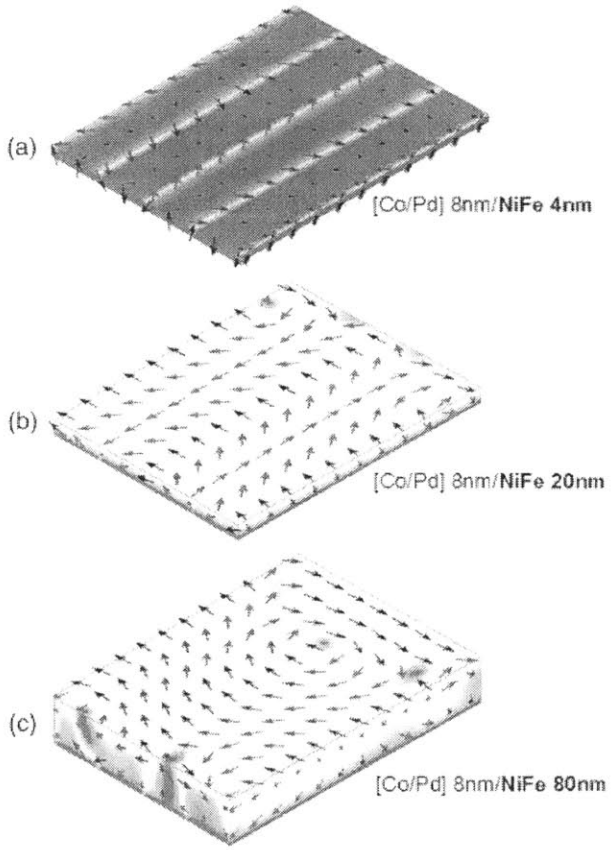

Figure 5.9: Micromagnetic simulation of a $[Co/Pd]_5$ /NiFe(x nm) multilayer, with a) x = 4 nm, b) x = 20 nm, and c) x = 80 nm. The colors represent the component of magnetization in the out-of-plane direction. Figure from [92]

5.4.1.1 Exchange Bias in CoCrPt / NiFe / IrMn

Because we have demonstrated that NiFe becomes PMA at low thicknesses when exchange-coupled with the PMA Co/Pd multilayers, NiFe became a promising candidate to serve as an intermediate layer for the exchange bias of a PMA material and an AFM. IrMn was once again used as the AFM because of good coupling with NiFe. CoCrPt was chosen as a non-multilayer PMA material for its strong perpendicular anisotropy of $8 \times 10^5\ J/m^3$ and compatibility with NiFe and IrMn. At the blocking temperature of NiFe/IrMn (520 K), CoCrPt maintains a saturation magnetization of around 75 emu cm^{-3}, based on Fig. 5.10. A hysteresis loop of a continuous film of CoCrPt is shown in Fig. 5.11, demonstrating strong perpendicular anisotropy.

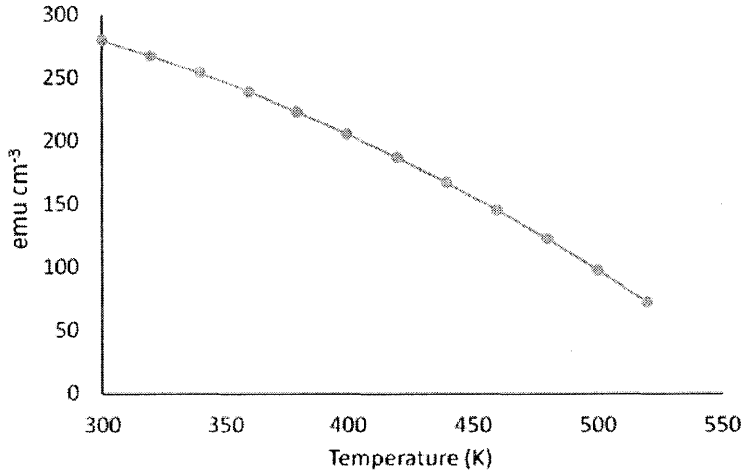

Figure 5.10: Saturation magnetization versus temperature for CoCrPt. At 520 K, CoCrPt maintains a magnetization of 75 emu cm^{-3}.

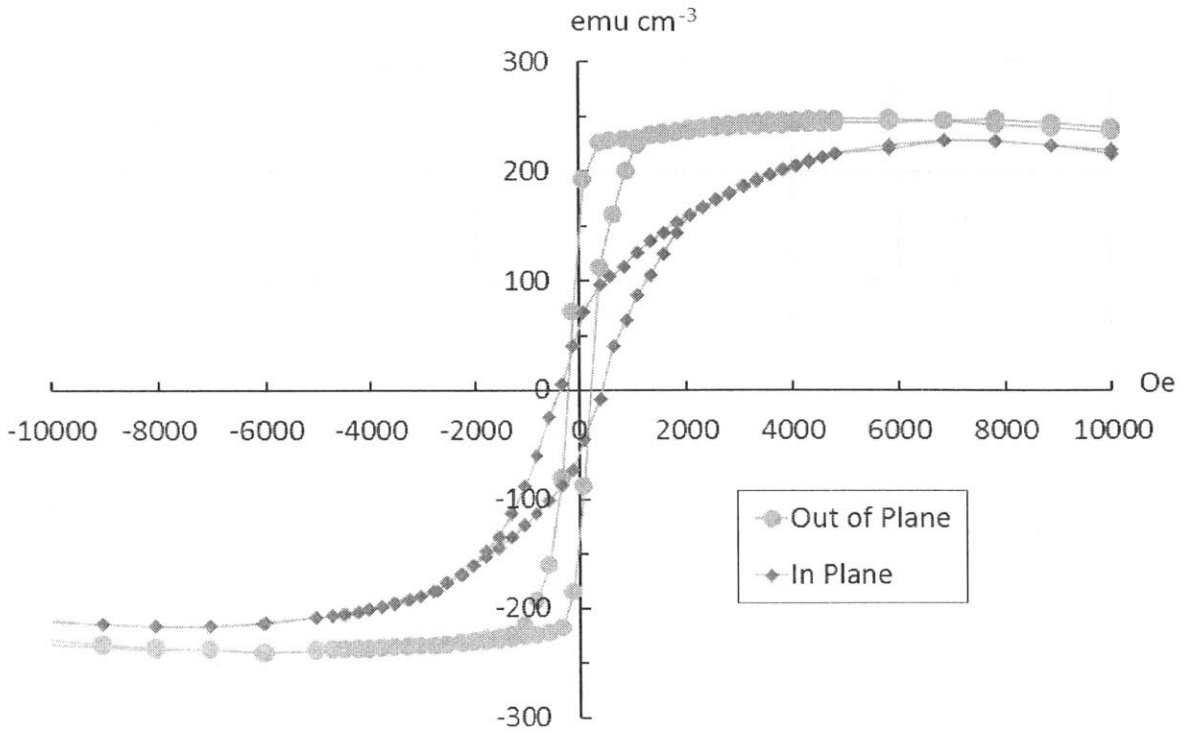

Figure 5.11: Hysteresis loop of a continuous film of Ti (10 nm) / CoCrPt (10 nm)

We applied the same fabrication method as in the previous sections on two sets of samples. In the first, before the IrMn layer is deposited, the sample is ion beam etched briefly, and the IrMn(10 nm) is deposited onto CoCrPt (10 nm). However, the loop shape remained almost the same as that of the continuous film of CoCrPt. In the second set of samples, before the IrMn layer is deposited, the sample is ion beam etched briefly, deposited with a few nanometers of NiFe as a replacement layer, and then deposited with IrMn. It is well known that NiFe couples well with IrMn, and it is also known from the simulations that thin layers of NiFe will adhere to a PMA orientation to match the PMA material underneath. Unfortunately, the magnitude of the exchange bias between NiFe and IrMn is much smaller than the coercivity. Hysteresis loops are shown in Fig. 5.11. The exchange-coupled CoCrPt/NiFe/IrMn system shows slightly less out-of-plane anisotropy than the CoCrPt does by itself.

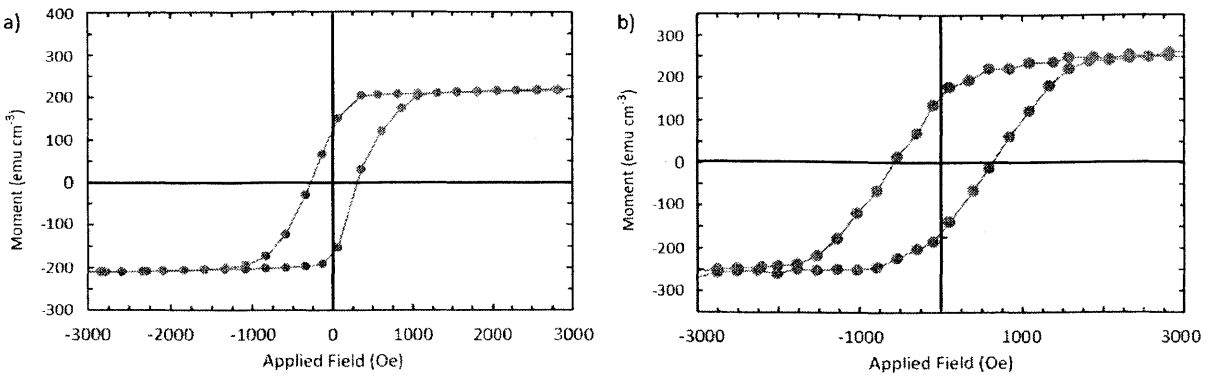

Figure 5.12: (a) Hysteresis loop of a Ti (10 nm) / CoCrPt (10 nm) / IrMn (10 nm) film. There is little difference in loop shape from that of a 10 nm CoCrPt film. (b) Hysteresis loop of a Ti (10 nm) / CoCrPt (10 nm) / NiFe (2 nm) / IrMn (10 nm) film. The loop shows a larger in-plane anisotropy component, but the exchange bias is small in comparison with the coercivity.

5.5 Summary

In this chapter, we have shown size-dependent magnetic switching behavior in 10 nm thick NiFe stripes of width 200 nm and periodicity 400 nm, underneath 10 nm thick IrMn stripes of width ranging from 200 nm to 500 nm, and periodicity ranging from 400 nm to 1μm, oriented perpendicular to the NiFe stripes. The magnetic switching behavior was mapped out as a function of the IrMn stripe width and spacing in both experiments and micromagnetic simulations. At low IrMn wire widths and spacings, the exchange-coupled region and free region switched together in both cases. Based on the simulations, the exchange bias was a weighted average of the two regions' exchange bias values. As the width and spacing increased, the free region switched separately from the pinned region, resulting in a two-step hysteresis loop. Based on the micromagnetic modeling, the critical width and spacing for two-step switching is limited by the domain wall width inside the NiFe, which in turn is dependent on the exchange length of the system, as well as the width and thickness of the NiFe wire.

We have also shown that NiFe, despite having an in-plane magnetic anisotropy, aligns its spins out of plane when exchange coupled to a thicker layer of PMA materials underneath, and that the spins tilt towards the in-plane direction as the thickness of NiFe is increased. CoCrPt with out-of-plane anisotropy was exchange-coupled with NiFe, which was in turn exchange-coupled with IrMn, but the magnitude of perpendicular exchange bias was negligible compared to the ~1 kOe coercivity of CoCrPt.

Chapter 6

Summary, Conclusions, Device Applications, and Future Work

6.1 Summary and Conclusions of Key Results

In this thesis, we have shown a two-step hybrid fabrication method to create locally exchange biased nanostructures in which the AFM is patterned differently from the FM. We have demonstrated that the ion beam etching step does not significantly affect magnetic properties, and examined exchange bias properties in a number of different nanoscale systems made using the fabrication method. We have also examined a PMA exchange bias system.

The hybrid fabrication method combines the benefits from both categories of exchange bias fabrication: the clean interface produced by the subtractive method, in which the two layers are deposited without breaking vacuum and the AFM in the unpinned region is oxidized or etched, and the scalability and flexibility of the additive method, in which the FM is deposited, pattern processing happens, and the AFM is deposited. The hybrid method does so by ion beam etching into the FM to remove impurities at the surface that would inhibit exchange bias, and redepositing a 1 nm replacement FM layer, followed by the AFM without breaking vacuum to create a good interface.

The hybrid fabrication method was used to form arrays of exchange biased dots with diameter 100–500 nm and periodicity 2.5 times the diameter, with NiFe and IrMn thicknesses of 10 nm.

The exchange bias dependence on ion beam etch duration is consistent with the inverse thickness relationship expected between FM thickness and exchange bias until the NiFe is etched past ~5 nm. Long durations of ion beam etching degraded the exchange bias due to film damage and roughness. The exchange bias ranged from 5 to 50 Oe in the dots and increased as dot size increased. The continuous films used for comparison showed exchange bias ranging from 10 to 100 Oe, though there were outliers that showed much higher exchange bias than normal. Some of the irregularities in the exchange bias trend versus dot size were attributed to reversal via vortex nucleation and propagation. This was common in the unbiased dot arrays in the larger dots, but persisted in only a small fraction of the exchange biased arrays. Scaling down the dot size also increased the training effect and lowered the blocking temperature of the system. Even though the AFM domain size was calculated to be 330 nm for a 10 nm thick IrMn film, exchange bias continued to decrease as the dot diameter decreased below this value, forcing the domain size to decrease with dot size. This was attributed to thermal effects, edge effects, and defects having more impact in small structures than in large structures.

We have also shown that the switching behavior in locally exchange biased structures, in which only a part of the FM is exchange biased, qualitatively changes when scaled down. The hybrid fabrication method was applied to make IrMn stripes of width 100-500 nm and periods of 240-1000 nm, on top of a continuous NiFe film. When the width and spacing between IrMn wires are small, the whole system switches at the reversal field. At higher dimensions, rather than switching together, the unpinned region has a different switching field than the pinned region. Micromagnetic simulations were performed and matched with the experimental data to provide insight into the experimental behavior, and micromagnetic images during the switch suggest several magnetic interactions whose relative strengths depend on dimensions:

1. The exchange energy in the bulk NiFe favors one-step switching by keeping the spins parallel. This effect becomes strong at low dimensions, and is relatively weak at higher dimensions.
2. The exchange coupling between the NiFe and IrMn favors two-step switching due to the unidirectional anisotropy at the interface of the pinned region. Because the thickness of the NiFe film is only 10 nm, the exchange coupling in the bulk NiFe transfers this unidirectional anisotropy through the material. This effect is strong at higher dimensions where the exchange bias is stronger.
3. The energy penalty of creating two domain walls in one unit cell favors one-step switching. This effect becomes extremely strong at low dimensions—in particular, dimensions around twice the FWHM of the domain wall.

All three of these effects suggest that one-step switching occurs at low dimensions, whereas two-step switching occurs at high dimensions, which was observed experimentally both when the applied field and exchange bias direction were parallel to the IrMn wires, and when the applied field and exchange bias direction were perpendicular to the IrMn wires. However, the critical dimensions required for two-step switching differed because of the difference in domain wall type. In the perpendicular case, the domain walls are head-to-head domain walls, which are much larger and have a much greater stray field. Thus, the contribution from point 3 above occurs at a much larger dimension and more strongly than in the parallel case.

A grating structure was also produced using the hybrid fabrication method. A IrMn stripe array was placed of a NiFe stripe array, rotated 90° from the former. Unsurprisingly, the same trends were present when the IrMn stripe dimensions were scaled down. The critical dimensions required for two-step switching were very large at around 500 nm, which is attributed to the large energy

penalty required to create and stabilize two head-to-head domain walls. However, more surprisingly, the exchange bias and switching properties only seemed to depend on the dimension in which the IrMn was scaled down. Changing the width and spacing of the NiFe wires did not appear to affect the exchange bias and switching when the exchange bias direction is along the NiFe wire length. We attribute this to the domain size of the AFM being larger than the exchange biased NiFe region, because the AFM is a stripe, and only a portion of the stripe contains NiFe underneath. This means that the domain size of the AFM could potentially be larger than the exchange biased region.

We have demonstrated that the in-plane magnetic anisotropy of NiFe can be reoriented out of plane if exchange-coupled with a strong PMA material such as Co/Pd multilayers. We have extended this principle to create out-of-plane exchange bias between the PMA CoCrPt, IMA NiFe, and IrMn. However, the exchange bias magnitude was orders of magnitude smaller than the coercivity of CoCrPt.

6.2 Future Works

There are two main categories of future works that could be carried out as a result of the study during this thesis:

1. The finding of more suitable perpendicular exchange bias systems, and investigation of the same magnetic interactions as in-plane systems, as well as different magnetic interactions only present in PMA systems, which govern switching behavior when scaled down.
2. Exploration of domain wall device applications using exchange bias to tailor the creation, removal, and manipulation of domain walls. Because many proposed devices use

current-driven domain wall motion, investigation of current-assisted switching of an exchange biased FM is also important.

In this section, we will discuss our future plans to implement these works, as well as their importance to device applications.

6.2.1 Experimental Demonstration of a PMA Exchange Bias System

The topic of perpendicular recording media, and perpendicular read heads and MRAMs has received much attention recently, and several out-of-plane exchange bias systems have been recorded [94]. However, there are a number of problems with many of them, such as operating temperature, scalability, and exchange bias magnitude versus coercivity. The CoCrPt/NiFe/IrMn system discussed in chapter 5 was one such system in which the coercivity was much higher than the exchange bias. A clear next step is to attempt to find a system that exhibits a significant exchange bias compared to the coercivity, while also operating at room temperature. There are several ways to go about this. Firstly, a different in-plane FM with a higher exchange bias can be considered. For example, Co and Ni are both potentially viable candidates because of their much higher exchange bias with their oxides. Secondly, a different PMA FM with a lower coercivity can be considered; for example, Fe/Pt multilayers or CoFeB, both of which show a lower coercivity than CoCrPt. The main requirement for exchange bias in each case would be that the PMA material can successfully exchange couple with the IMA material and reorient its anisotropy. In addition, the Curie temperature of the PMA material must be above the blocking temperature of the IMA FM/AFM system. Using micromagnetic simulations and MFM on the upper layer of the in-plane material would give an idea of how well the in-plane material is displaying out-of-plane anisotropy. Once a suitable system is established, it will be possible to use our hybrid fabrication method to determine the effects of scaling on perpendicular exchange bias systems. Because there are

additional parameters that govern the switching behavior in perpendicular exchange bias (for example, the strength of the PMA), exploring these systems at the nanoscale will prove to be not only scientifically interesting, but also critical in terms of integration into magnetic devices.

6.2.2 Creating and Pinning Domain Walls Using Exchange Bias

An ongoing work of ours at the time of this writing involves "horseshoe" FM structures with the ends pinned with exchange bias. A schematic of the setup, along with an electron beam lithography write pattern, is shown in Fig. 6.1. Because domain walls can be used as data tokens [70] or as a low-energy method of switching portions of FM [24], being able to control the pinning of a domain wall in a device using exchange bias may offer many advantages in domain wall devices.

6.2.2.1 Application to Domain Wall Logic Devices

From the results in chapters 4 and 5, we have established a theory that correlates dimension size of the AFM to exchange bias properties and switching behavior. We can tailor the length, L [Fig. 6.1(a)], of the exchange biased portion of the horseshoe, as well as the length of the FM arc to ensure that there will always be at least one domain wall trapped in the system, and that the domain wall may freely move and switch various portions of the arc without also switching the exchange biased region. In addition, the creation and removal of the domain wall may be tailored by altering the lengths L_1 and L_2 to ensure a different switching field for the left and right ends of the arc. For example, if L_2 were much shorter than L_1, a weak magnetic field or current may be applied to the right, followed by a weak field or current downwards to remove the domain wall. To retrieve the domain wall, the field must simply be removed, and the pinned region to the right will switch again, bringing back the domain wall. The creation, removal, and motion of domain walls can be tracked using an electrical anisotropic magnetoresistance (AMR) measurement, or using MFM.

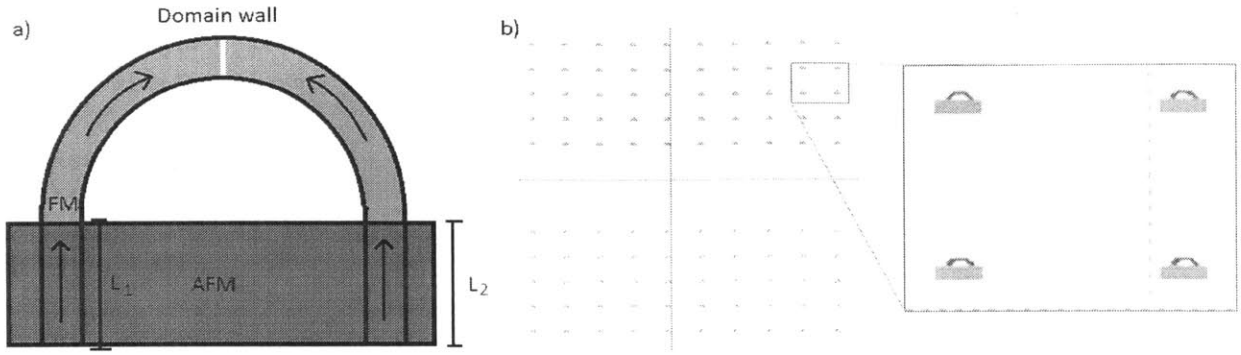

Figure 6.1: (a) Schematic of a horseshoe structure with exchange biased ends, used to trap domain walls. L_1 and L_2 indicate the lengths of the left and right sections of the exchange biased portion of the arc respectively. (b) Electron beam lithography write pattern for such a structure.

In the case of a domain wall device such as one proposed by a colleague [24], shown in Fig. 6.2, in order for the device to operate, the exchange bias must be strong enough such that applying a current moves the domain wall but does not flip the pinned portion, and weak enough such that when the current is shut off, the domain wall does not drift back into the center of the wire, unintentionally switching the device. To realize this device, the hybrid fabrication method can be used to create the FM and AFM layers. A third processing step can be made to create the magnetic tunnel junction. Electrical measurement can be carried out using waveguide electrodes.

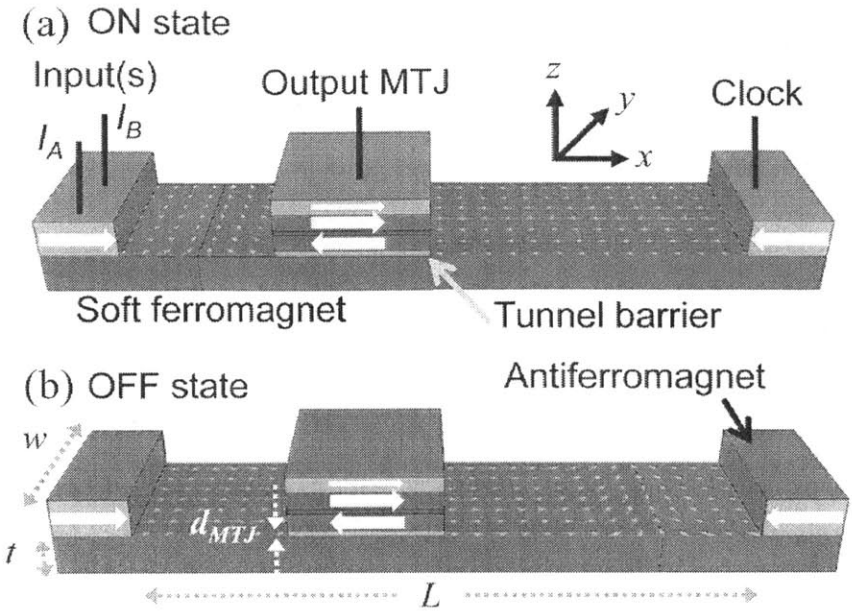

Figure 6.2: Schematic of the domain wall device [24]. An MTJ reads the magnetization state of the FM.

The creation of more complex domain walls is also possible using exchange bias. For example, based on micromagnetic simulations performed to create 360° and higher order domain walls [70], if the exchange biased pads at the ends of the arc are long enough to create exchange bias magnitudes of ~120 Oe, which was the field needed to nucleate additional domain walls into the system, it is possible to reverse the field strongly enough to create a set of two more domain walls without switching the pinned region.

6.2.2.2 Application to Pinning Sites in Magnetic Storage

A famous example of a proposed magnetic storage device is racetrack memory [95]. Racetrack memory stores data in a magnetic wire, using domain walls arbitrarily spaced as data tokens. A readback system, such as a tunnel magnetoresistance (TMR) or giant magnetoresistance (GMR) stack is placed at the center. The system reads data by pulsing DC current to shift the domain walls back and forth along the wire. A schematic of a racetrack memeory is shown in Fig. 6.3.

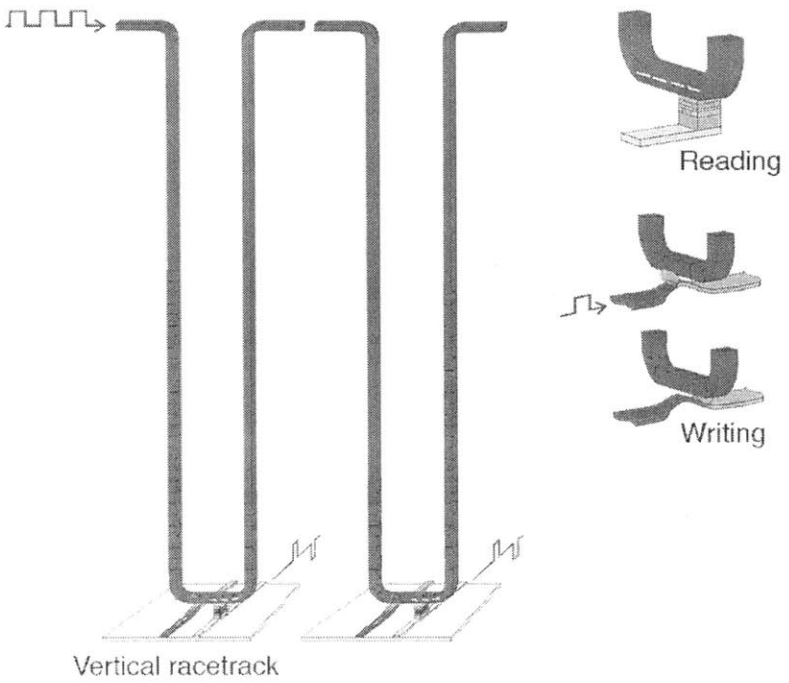

Fig. 6.3: Schematic of a racetrack memory device. Figure adapted from [95].

However, domain walls must be tightly packed to achieve good data density, and domain walls couple with each other at a distance several times their own width [70]. Because of this, racetrack memory suffers from incoherent motion of domain walls at any good data density, as the stray fields interact at close distances. Usually, the coherent motion problem is circumvented by using regularly-spaced notches in the wires [95]. However, notches not only make the system very difficult to fabricate at small scales, but are also inconsistent. It was found that even with one domain wall, the same pulse did not de-pin the domain wall consistently [95].

Exchange bias can be used instead of notches as a method for trapping the domain walls in such a device. The strength of the exchange bias can be tailored using the dimensions of the exchange-coupled region and should be strong enough to keep a domain wall from drifting due to stray field interaction with a neighboring domain wall, but also weak enough to achieve good data density.

In addition, if the need arises, a particular pinning site can be "turned off" by applying a local field to match the exchange bias magnitude at that AFM pad. The pinning behavior can also be used in the domain wall logic device described in section 6.2.2.1 to create energy wells for the domain wall to settle along either side of the wire, increasing the reliability of the device. The principle is illustrated in Fig. 6.4.

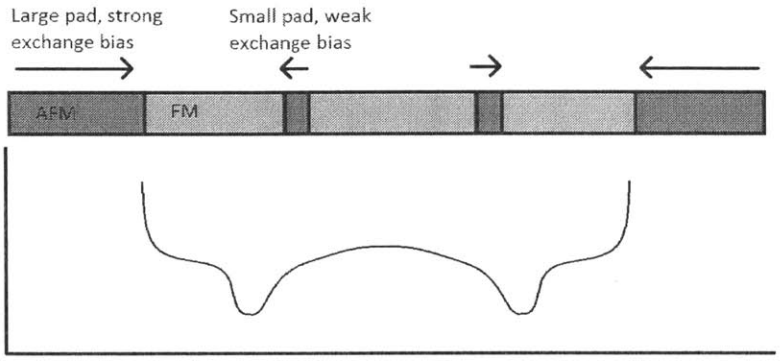

Figure 6.4: Illustration of how the energy landscape may look like for a domain wall if weak exchange bias regions were introduced on into a domain wall device, creating pinned regions for the domain wall.

References

[1] W.H. Meiklejohn, C.P. Bean, "New magnetic anisotropy," Phys. Rev. **102**, 1413 (1956).

[2] W.H Meiklejohn, C.P Bean, "New magnetic anisotropy," Phys. Rev., **105**, 904 (1957)

[3] E.P. Wohlfarth, "Hard magnetic materials," Adv. Phys. **8**, 87 (1959).

[4] H. Schmid, Cobalt **6**, 8 (1960).

[5] J.S. Kouvel, "A ferromagnetic-antiferromagnetic model for copper-manganese and related alloys," J. Phys. Chem. Sol. **24**, 795 (1963).

[6] N.H. March, P. Lambin, F. Herman, "Cooperative magnetic properties in single-and two-phase 3d metallic alloys relevant to exchange and magnetocrystalline anisotropy," J. Magn. Magn. Mater. **44**, 1 (1984)

[7] K. Fukamichi, "Close Relationship between the Physical Properties and Practical Applications of Antiferromagnets," J. Magn. Soc. Japan 21 (1997) 1062.

[8] M Takahashi, A Yanai, S Taguchi, T Suzuki, "A study of exchange anisotropy in Co-CoO evaporated thin films," Jpn. J. Appl. Phys., **19,** 1093 (1980)

[9] C. Tang, "Magnetics of small magnetoresistive sensors," J. Appl. Phys. **55,** 2226 (1984).

[10] M Ohkoshi, K Tamari, M Harada, S Honda, T Kusuda, "Microstructure and Exchange Anisotropy of Co-CoO Sputtered Films with Perpendicular Magnetization," IEEE Transl. J. Magn. Japan, **1,** 37 (1985)

[11] B. Dieny, V.S Speriosu, S.S.P Parkin, B.A Gurney, D.R Wilhoit, D Mauri, "Giant magnetoresistive in soft ferromagnetic multilayers," Phys. Rev. B, **43**, 1297 (1991)

[12] J. Nogues, J. Sort, V. Langlais, V. Skumryev, S. Surinach, J.S. Munoz, and M.D. Baro, "Exchange bias in nanostructures," Phys. Rep. 422, 65-117 (2005)

[13] L Smardz, U Köbler, W Zinn, "Temperature and thickness dependence of unidirectional magnetic anisotropy effects in Co/CoO thin films," Vacuum, **42,** 283 (1991)

[14] X Lin, A.S Murthy, G.C Hadjipanayis, C Swann, S.I Shah, "Magnetic and structural properties of Fe - FeO bilayers," J. Appl. Phys., **76**, 6543 (1994)

[15] F.B Hagedorn, "Exchange anisotropy in oxidized permalloy thin films at low temperatures," J. Appl. Phys., **38,** 3641 (1967)

[16] O Massanet, R Montmory, "Magnetic properties of multilayer films of FeNi-Mn-FeNiCo and of FeNi-Mn ," C. R. Acad. Sci. Paris, **258,** 1752 (1964)

[17] R.D Hempstead, S Krongelb, D.A Thompson, "Unidirectional anisotropy in nickel-iron films by exchange coupling with antiferromagnetic films," IEEE Trans. Magn., **14,** 521 (1978)

[18] K.T.Y Kung, L.K Louie, "MnFe structure - exchange anisotropy relation in the NiFe/MnFe/NiFe system," J. Appl. Phys., **69,** 5634 (1991)

[19] K Hoshino, S Noguchi, R Nakatani, H Hoshiya, Y Sugita, "Magnetoresistance and Interlayer Exchange Coupling between Magnetic Layers in Fe–Mn/Ni–Fe–Co/Cu/Ni–Fe–Co Multilayers," Jpn. J. Appl. Phys., **33,** 1327 (1994)

[20] A.J Devasahayam, K.R Mountfield, M.H Kryder, "Small track width MR sensors stabilized with NiMn," IEEE Trans. Magn., **33,** 2881 (1997)

[21] B.Y Wong, C Mitsumata, S Prakash, D.E Laughlin, T Kobayashi, "The interplay between NiMn/NiFe epitaxial growth and NiMn atomic ordering in NiMn/NiFe exchange biased layers: a structural perspective," IEEE Trans. Magn., **32,** 342 (1996)

[22] J. Nogues, I.K. Schuller, "Exchange Bias," J. Magn. Magn. Mater, **192**, 203-232 (1999)

[23] A.A Glazer, A.P Potapov, R.I Tagirov, "Thermographic Recording on a Manganese-permalloy Film with Exchange Anisotropy," Sov. Phys. JETP. Lett., **15,** 259 (1972)

[24] J. A. Currivan, Y. Jang, M. D. Mascaro, M. A. Baldo, and C. A. Ross, "Low energy magnetic domain wall logic in short, narrow, ferromagnetic wires," IEEE Magn. Lett. **3**, 3000104 (2012).

[25] R Jungblut, R Coehoorn, M.T Johnson, J aan de Stegge, A Reinders, "Orientational dependence of the exchange biasing in molecular - beam - epitaxy - grown Ni80Fe20/Fe50Mn50 bilayers," J. Appl. Phys., 75, 6659 (1994)

[26] A. P. Malozemoff, "Random-field model of exchange anisotropy at rough ferromagnetic-antiferromagnetic interfaces," Phys. Rev. B 35, 3679 (1987).

[27] J Nogués, D Lederman, T.J Moran, I.K Schuller, K.V Rao, "Large exchange bias and its connection to interface structure in FeF2–Fe bilayers," Appl. Phys. Lett., 68, 3186 (1996)

[28] D Lederman, J Nogués, I.K Schuller, "Exchange anisotropy and the antiferromagnetic surface order parameter," Phys. Rev. B, 56, 2332 (1997)

[29] V. Baltz, J. Sort, S. Landis, B. Rodmaq, B. Dieny, "Size effects on exchange bias in sub-100 nm ferromagnetic–antiferromagnetic dots deposited on prepatterned substrates," Appl. Phys. Lett. **84**, 4923 (2004)

[30] R.C. O'Handley, *Modern Magnetic Materials: Principles and Applications*, Wiley-Interscience, 2000.

[31] M.J Carey, A.E Berkowitz, "Exchange anisotropy in coupled films of Ni81Fe19 with NiO and CoxNi1− xO," Appl. Phys. Lett., 60, 3060 (1992)

[32] C Schlenker, D Paccard, "Couplages ferromagnétiques-antiferromagnétiques: étude des contractions de cycles d'hystérésis à l'aide d'un traceur de cycle très basses fréquences," J. de Phys. (France), 28, 611 (1967)

[33] J. Stohr and H.C. Siegmann, Magnetism From Fundamentals to Nanoscale Dynamics, Springer Series in Solid-State Sciences, 2006

[34] H. Ohldag, A. Scholl, F. Nolting, S. Anders, F.U. Hillebrecht, and J. Stöhr, "Spin Reorientation at the Antiferromagnetic NiO(001) Surface in Response to an Adjacent Ferromagnet," Phys. Rev. Lett. 86, 2878 (2001)

[35] D.E. Bürgler, P.A. Grünberg, in: R.Waser (Ed.), Nanoelectronics and Information Technology, Wiley-VCH,Weinheim, 2003

[36] J.F. Bobo, L. Gabillet, M. Bibes, "Recent advances in nanomagnetism and spin electronics," J. Phys.: Condens. Matter 16, S471 (2004).

[37] I.K. Schuller, "Unusual phenomena in exchange-biased nanostructures," MRS Bull. 29, 642 (2004).

[38] H. Ohldag, A. Scholl, F. Nolting, E. Arenholz, S. Maat, A.T. Young,, M. Carey, J. Stöhr, "Correlation between Exchange Bias and Pinned Interfacial Spins," Phys. Rev. Lett. 91, 017203 (2003)

[39] J Bransky, I Bransky, A.A Hirsch, "Exchange Anisotropy in Thin Cobalt Films Deposited on a CoO Single-Crystal Substrate," J. Appl. Phys., 41, 183 (1970)

[40] U. Nowak, A. Misra, K.D. Usadel, "Domain state model for exchange bias," J. Appl. Phys. 89, 7269 (2001).

[41] V. Baltz, J. Sort, S. Landis, B. Rodmacq, and B. Dieny, "Tailoring size effects on the exchange bias in ferromagnetic-antiferromagnetic <100 nm nanostructures," Phys. Rev. Lett. **94**, 117201 (2005)

[42] D. Mauri, H.C. Siegmann, P.S. Bagus, and E. Kay, "Simple model for thin ferromagnetic films exchange coupled to an antiferromagnetic substrate," J. Appl. Phys. 62, 3047 (1987)

[43] "Exchange bias," https://www-ssrl.slac.stanford.edu/stohr/magneticexchange.htm

[44] K.B. Jung, H. Cho, K.P. Lee, J. Marburger, F. Sharifi, R.K. Singh, D. Kumar, K.H. Dahmen, and S.J. Pearton, "Development of chemically assisted dry etching methods for magnetic device structures," J. Vac. Sci. Technol. B **17**, 3186 (1999)

[45] S.W. Pang, D.D. Rathman, D.J. Silversmith, R.W. Mountain, and P.D. DeGraff, "Damage induced in Si by ion milling or reactive ion etching," J. Appl. Phys, **54**, 3272 (1983)

[46] K.B. Jung, J. Hong, H. Cho, J.A. Caballero, J.R. Childress, S.J. Pearton, M. Jenson, and A.T. Hurst Jr, "High density plasma etching of NiFe, NiFeCo, and NiMnSb-based multilayers for magnetic storage elements," Appl. Surf. Sci. **138-139**, 111-116 (1999)

[47] G. Xiong, D.A. Allwood, M.D. Cooke, and R.P. Cowburn, "Magnetic nanoelements for magnetoelectronics made by focused-ion beam milling," Appl. Phys. Lett. **79**, 3461 (2001)

[48] R.C. Sousa and P.P. Freitas, "Influence of ion beam milling parameters on MRAM switching," IEEE Trans. Magn. **37**, 4, 1973-1975 (2001)

[49] Z.B. Guo, K.B. Li, G.C. Han, Z.Y. Liu, P. Luo, and Y.H. Wu, "Exchange bias in patterned FeMn/NiFe bilayers," J. Magn. Magn. Mater. **251**, 323-326 (2002)

[50] C. Hamann, I. Monch, R. Kaltofen, R. Schafer, T. Gemming, L. Schultz, and J. McCord, "Size effects on the magnetization reversal behavior of exchange bias modulated thin films," J. Appl. Phys. **104**, 013926 (2008)

[51] K. Liu, J. Nogues, C. Leighton, H. Masuda, K. Nishio, I. V. Roshchin, and I. K. Schuller, "Fabrication and thermal stability of arrays of Fe nanodots," Appl. Phys. Lett. **81**, 4434 (2002).

[52] J.I. Martín, J. Nogués, K. Liu, J.L. Vicent, I.K. Schuller, "Ordered magnetic nanostructures: fabrication and properties," J. Magn. Magn. Mater. **256**, 449 (2003).

[53] J. Himpsel, J.E. Ortega, G.J. Mankey, R.F.Willis, "Magnetic nanostructures," Adv. Phys. **47,** 511 (1998).

[54] Y. Otani, A. Nemoto, S.G. Kim, K. Fukamichi, O. Kitakami,Y. Shimada, "Magnetotransport properties of submicron exchange coupled Fe19Ni81/NiO wires," J. Magn. Magn. Mater. **198–199**, 434 (1999).

[55] A. Nemoto,Y. Otani, S.G. Kim, K. Fukamichi, O. Kitakami,Y. Shimada, "Magnetoresistance and planar Hall effects in submicron exchange-coupled NiO/Fe19Ni81 wires," Appl. Phys. Lett. **74**, 4026 (1999)

[56] M. Fraune, U. Rudiger, G. Guntherodt, S. Cardoso, and P. Freitas, "Size dependence of the exchange bias field in NiO/Ni nanostructures," Appl. Phys. Lett. **77**, 3815 (2000)

[57] T. Kimura, G. Mozumi, F.Wakaya, K. Gamo, "Effects of Shape Anisotropy in CoO/Co/Cu/NiFe/Cu/Co Wires," Jpn. J. Appl. Phys. **40**, 2241 (2001)

[58] S. Mao, J. Giusti, N. Amin, J. van Ek, E. Murdock, "Giant magnetoresistance properties of patterned IrMn exchange biased spin valves," J. Appl. Phys. **85,** 6112 (1999)

[59] Y. Shen, Y. Wu, H. Xie, K. Li, J. Qiu, and Z. Guo, "Exchange bias of patterned NiFe/IrMn film," J. Appl. Phys. **91**, 8001 (2002)

[60] A. Hoffmann, M. Grimsditch, J.E. Pearson, J. Nogués, W.W.A. Macedo, I.K. Schuller, "Tailoring the exchange bias via shape anisotropy in ferromagnetic/antiferromagnetic exchange-coupled systems," Phys. Rev. B **67,** 220406 (2003)

[61] S.H. Chung, A. Hoffmann, M. Grimsditch, "Interplay between exchange bias and uniaxial anisotropy in a ferromagnetic/antiferromagnetic exchange-coupled system," Phys. Rev. B 71 (2005) 214430

[62] J. Grisolia, C. Martin, L. Ressier, F. Carcenac, C. Vieu, J.F. Bobo, "Patterning of sub-micrometric Co/NiO dots by hot embossing lithography and study of their magnetic properties," J. Magn. Magn. Mater. **272–276,** e1293 (2004)

[63] J.Yu, A.D. Kent, S.S.P. Parkin, "Exchange biasing in polycrystalline thin film microstructures," J. Appl. Phys. **87,** 5049 (2000)

[64] C. Hamann, J. McCord, L. Schultz, B.P. Toperverg, K. Theis-Brohl, M. Wolff, R. Kaltofen, and I. Monch, "Competing magnetic interactions in exchange-bias-modulated films," Phys. Rev. B **81**, 024420 (2010)

[65] E. Girgis, R.D. Portugal, M.J. Van Bael, K. Temst, C. Van Haesendonck, "Asymmetric magnetization reversal in exchange-biased NiFe/CoO submicron-sized structures," J. Appl. Phys. **97,** 103911 (2005)

[66] C. Prados, E. Pina, A. Hernando, A. Montone, "Reversal of exchange bias in nanocrystalline antiferromagnetic ferromagnetic bilayers," J. Phys.: Condens. Matter **14,** 10063 (2002)

[67] M. Ali, C.H. Marrows, B.J. Hickey, "Onset of exchange bias in ultrathin antiferromagnetic layers," Phys. Rev. B **67,** 172405 (2003)

[68] W.T. Lee, S.G.E. te Velthuis, G.P. Felcher, F. Klose, T. Gredig, E.D. Dahlberg, "Ferromagnetic domain distribution in thin films during magnetization reversal," Phys. Rev. B **65**, 224417 (2002)

[69] T. O'Reilly, "Lloyd's mirror interference lithography," NanoStructures Laboratory operating procedures (2005)

[70] M. Mascaro, "Magnetic Behavior of 360° Domain Walls in Patterned Magnetic Thin Films," Doctorate thesis, Massachusetts Institute of Technology (2012)

[71] R.C. Jaeger, "Film Deposition". *Introduction to Microelectronic Fabrication (2nd ed.),* Upper Saddle River: Prentice Hall (2002)

[72] L. Bi, "Magneto-Optical Oxide Thin films and Integrated Nonreciprocal Photonic Devices," Doctorate thesis, Massachusetts Institute of Technology (2011)

[73] M.J. Donahue and D.G. Porter, "Oommf user's guide, version 1.0," Tech. Rep. Interagency Report NISTIR 6376, National Institute of Standards and Technology, 1999

[74] T.L. Gilbert, "A phenomenological theory of damping in ferromagnetic materials," IEEE Trans. Magn. **40** 3443 (2004)

[75] J.I. Matrin, J. Nogues, K. Liu, J.L. Vincent, I.K. Schuller, "Ordered magnetic nanostructures: fabrication and properties," J. Magn. Magn. Mater, **256**, 449-501 (2003)

[76] A. Nemoto, Y. Otani, S.G. Kim, K. Fukamichi, O. Kitakami, and Y. Shimada, "Magnetoresistance and planar Hall effects in submicron exchange-coupled NiO/$Fe_{19}Ni_{81}$ wires," Appl. Phys. Lett, **74**, 4026 (1999)

[77] J. Sort, H. Glaczynska, U. Ebels, B. Dieny, M. Giersig, J. Rybczynski, "Exchange bias effects in submicron antiferromagnetic-ferromagnetic dots prepared by nanosphere lithography," J. Appl. Phys. **95**, 7516 (2004)

[78] H. Xi, J. Rantschler, S. Mao, M.T. Kief, and R.M. White, "Interface coupling and magnetic properties of exchange-coupled $Ni_{81}Fe_{19}/Ir_{22}Mn_{78}$ bilayers," J. Phys. D: Appl. Phys. **36**, 1464 (2003)

[79] R.P. Cowburn, D.K. Koltsov, A.O. Adeyeye, M.E. Welland, and D.M. Tricker, "Single-Domain Circular Nanomagnets," Phys. Rev. Lett. **83**, 1042, (1999)

[80] N. Kikuchi, S. Okamoto, O. Kitakami, Y. Shimada, S.G. Kim, Y. Otani, and K. Fukamichi, "Vertical magnetization process in sub-micron permalloy dots," IEEE Trans. Magn. **37**, 2082 (2001)

[81] A.L. Dantas, G.O.G. Rebouças, and A.S. Carriço, "Vortex nucleation in exchange biased magnetic nanoelements," IEEE Trans. Magn, **46**, 2311 (2010)

[82] C. Binek, S. Polisetty, X. He, and A. Berger, "Exchange bias training effect in coupled all ferromagnetic bilayer structures," Phys. Rev. Lett. **96**, 067201 (2006)

[83] U. Welp, S.G.E. te Velthuis, G.P. Felcher, T. Gredig, and E.D. Dahlberg, "Domain formation in exchange biased Co/CoO bilayers," J. Appl. Phys. **93**, 7726 (2003)

[84] G. S. Abo, Y. Hong, J. Park, J. Lee, W. Lee, and B. Choi, "Definition of magnetic exchange length," IEEE Trans. Magn. **49**, 4937 (2013)

[85] M. Klaui, C. A. F. Vaz, J. Rothman, J. A. C. Bland, W. Wernsdorfer, G. Faini, and E. Cambril, "Domain wall pinning in narrow ferromagnetic ring structures probed by magnetoresistance measurements," Phys. Rev. Lett., **90**, 097202 (2003)

[86] E. Girgis, R.D. Portugal, M.J. Van Bael, K. Temst, C. Van Haesendonck, "Asymmetric magnetization reversal in exchange-biased NiFe/CoO submicron-sized structures," J. Appl. Phys. **97**, 103911 (2005)

[87] J. Sort, A. Hoffmann, S.H. Chung, K.S. Buchanan, M. Grimsditch, M.D. Baró, B. Dieny, J. Nogués, "Magnetization reversal in submicron disks: Exchange biased vortices," Phys. Rev. Lett. (2005) 067201

[88] Y.J. Yang, C.H. Lai, "Size and shape effects on exchange field of patterned NiO/NiFe films," J. Appl. Phys. 89, 7537 (2001)

[89] Z.P. Li, O. Petracic, J. Eisenmenger, I.K. Schuller, "Reversal behavior of exchange-biased submicron dots," Appl. Phys. Lett. 86, 072501 (2005)

[90] X. Ji and K.M. Krishnan, "Competing magnetic interactions in perpendicular exchange-biased $[Co/Pt]_y/FeMn$ multilayers," J. Appl. Phys. **99,** 08C105 (2006)

[91] N.N. Phuoc and T. Suzuki, "Perpendicular exchange bias and magnetic anisotropy in FePt/FeMn multilayers," IEEE Trans. Magn. **42**, 10, 2996 (2006)

[92] L. Tryputen, F. Guo, F. Liu, T.N. Anh Nguyen, M. S. Mohseni, S. Chung, Y. Fang, J. Akerman, R.D. McMichael, and C.A. Ross, "Magnetic structure and anisotropy of $[Co/Pd]_5/NiFe$ multilayers," Phys Rev B 91 014407 (2015)

[93] S. Tacchi, T. N. A. Nguyen, G. Carlotti, G. Gubbiotti, M. Madami, R. K. Dumas, J. W. Lau, J. Akerman, A. Rettori, and M. G. Pini, "Spin wave excitations in exchange-coupled [Co/Pd]-NiFe films with tunable tilting of the magnetization," Phys. Rev. B 87, 144426 (2013).

[94] N.H. Dung, N.P. Thuy, N.A. Tuan, N.T. Long, N.N. Phuoc, "Out-of-plane exchange bias and magnetic anisotropy in MnPd/Co multilayers," J. Magn. Magn. Mater. **320,** 3334-3340 (2008)

[95] S. S. P. Parkin, M. Hayashi, and L. Thomas, "Magnetic domain-wall racetrack memory," Science, **320**, 5873, 190-194 (2008)

[96] M. Lang, M. Montazeri, M.C. Onbasli, X. Kou, Y. Fan, P. Upadhyaya, K. Yao, F. Liu, Y. Jiang, W. Jiang, K.L. Wong, G. Yu, J. Tang, T. Nie, L. He, R.N. Schwartz, Y. Wang, C.A. Ross, and K.L. Wang, "Proximity Induced High-Temperature Magnetic Order in Topological Insulator - Ferrimagnetic Insulator Heterostructure," Nano Lett, 14 (6), 3459-3465 (2014)

Appendix A

Spintronics: Bi_2Se_3 Surface States Near YIG

Until recently, topological insulators (TI) in spintronic devices exhibited time-reversal symmetry (TRS), in which the surface state spins are pinned to the momentum [96]. However, in a collaboration between UCLA, MIT, and Zhejiang University, a method to break the time-reversal symmetry by introducing magnetic order into a TI was investigated. A 50 nm thick yttrium iron garnet (YIG) was grown by pulsed laser deposition on a paramagnetic gallium gadolinium garnet (GGG) substrate at 650 °C. YIG was chosen for its high Curie temperature and extensive study in the literature as a ferrimagnetic insulator (FMI) for spin waves [96]. Bi_2Se_3 was grown on the YIG/GGG substrate using molecular beam epitaxy (MBE) under ultrahigh vacuum (UHV) at 200 °C. A scanning transmission electron microscope (STEM) image of the interface is shown in Fig. A.1. A correlation between the magnetization state of a YIG layer and the transport properties of Bi_2Se_3 was found. Previously, such magnetic effects have only been demonstrated up to 35 K. However, ordering the surface states of Bi_2Se_3 near YIG produced a magnetic signal from the Bi_2Se_3 up to 130 K, measured using the magneto-optic Kerr effect (MOKE). The magnetic signal contained a significant out-of-plane component in the form of a butterfly-shaped hysteresis loop and was believed to originate from the YIG.

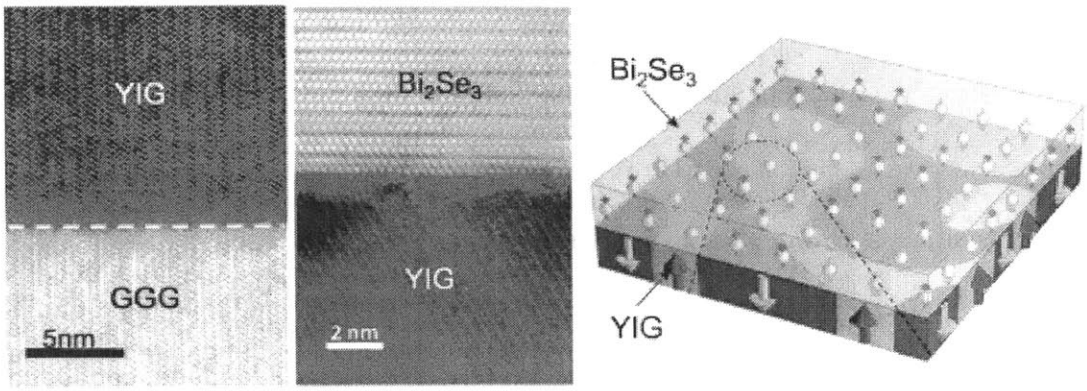

Figure A.1: A STEM image (left) of Bi_2Se_3/YIG/GGG, showing the two interfaces, along with a schematic of the Bi_2Se_3/YIG in the presence of a YIG domain structure. Figure adapted from [96]

A.1 Micromagnetic Simulations of YIG

I took part in this project by providing micromagnetic simulations of the YIG using OOMMF [73] to confirm whether or not the observed butterfly-shaped loop originated from the YIG.

A rectangular mesh was used with unit cell size 5 nm x 5 nm x 25 nm. The x and y cell sizes were chosen such that the cell size was smaller than the exchange length of the YIG. The damping parameter α was set to 0.5 due to the quasistatic nature of each relaxation measurement in the hysteresis loop. Because the YIG was grown experimentally in the (111) orientation, an anisotropy of 2500 Jm^{-3} [96] was used, with the axes rotated accordingly. The system was allowed to relax from a random initial state, and a hysteresis loop was measured from +5kOe to -5kOe.

A low-temperature polar MOKE measurement of the YIG/GGG heterostructure is shown in Fig. A.2(a), and a hysteresis loop generated by OOMMF is shown in Fig. A.2(b) along with micromagnetic images at various steps. The micromagnetic simulations showed qualitative agreement with the MOKE measurements: the magnetization was found to be primarily in-plane, with a slight out-of-plane component due to the easy axes being tilted. The net magnetic anisotropy

is a summation of the shape anisotropy and the magnetocrystalline anisotropy. The shape anisotropy favors in-plane magnetization, but the magnetocrystalline anisotropy favors magnetization along the <111> easy axes. However, the shape anisotropy becomes far greater than the magnetocrystalline anisotropy as temperature increases, as evidenced by the MOKE measurements. Magnetoelastic anisotropy, which favors out-of-plane magnetization, also contributes. However, the magnetoelastic anisotropy is weak in comparison to the other anisotropies because of the small thermal mismatch between YIG and GGG.

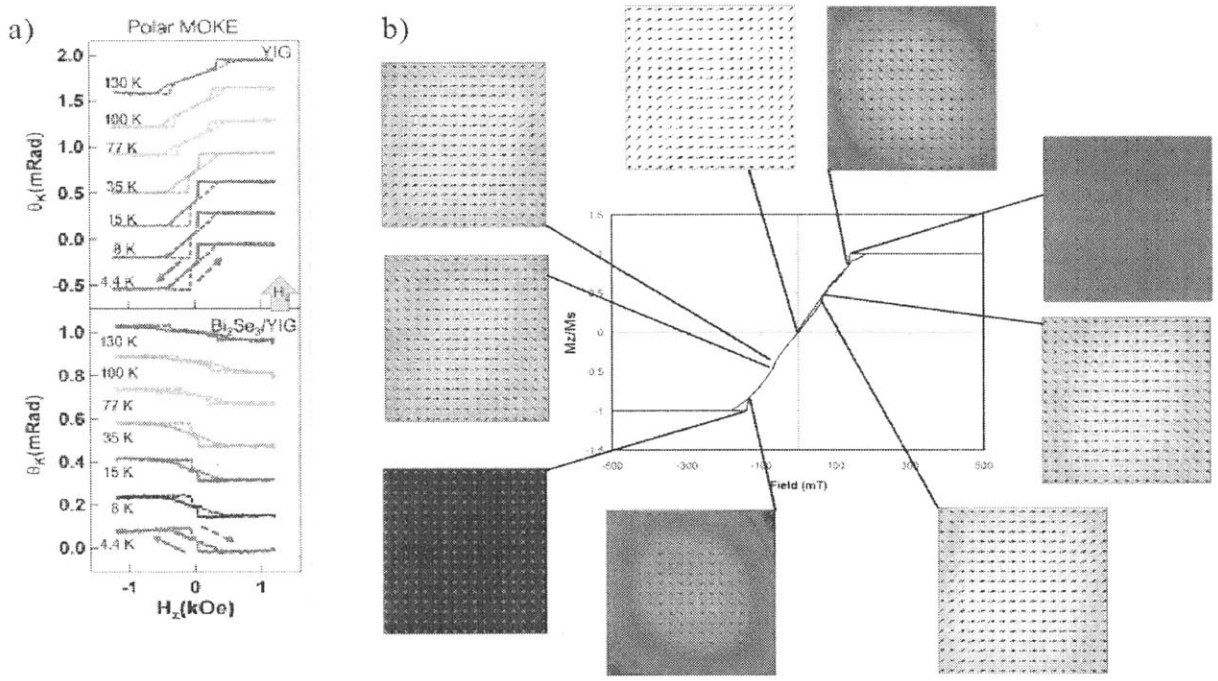

Figure A.2: a) Polar MOKE measurements of YIG (top) and Bi_2Se_3/YIG (bottom) at various low temperatures. Adapted from [96]. b) Hysteresis loop and micromagnetic images generated using OOMMF, showing qualitative agreement for the out-of-plane component of YIG.

Because a YIG film shows an out-of-plane component, it is possible to engineer a TI/FMI heterostructure to study high temperature spintronic devices. The out-of-plane anisotropy at higher temperatures could break the TRS and control the magnetic properties of the TI, even at room temperature.

Appendix B

Cleaner Liftoff Using a Modified Trilayer Resist

Typically, layers of photoresist are removed using an NMP solution or 1165. However, ARC is difficult to remove, as shown in chapter 3, Fig. 3.1(c). The residual ARC is nonmagnetic and does not affect any magnetic measurements, and the method to obtain a cleaner sample presented in this appendix was primarily used to create better SEM images.

B.1 PMMA Underneath ARC

PMMA was chosen to be the bottom layer of the modified resist stack because of several desirable properties. Firstly, O_2 etches through both ARC and PMMA, which means no extra RIE steps and interlayers are required. Secondly, PMMA is extremely easy to dissolve using NMP or 1165, only requiring a few minutes of immersion, as described in section 2.1.4. A schematic of the resist mask fabrication and deposition is provided in Fig. B.1. A comparison between a sample made using the regular trilayer resist and a sample made using the PMMA method is shown in Fig. B.2. No visible traces of residual ARC are present in the latter.

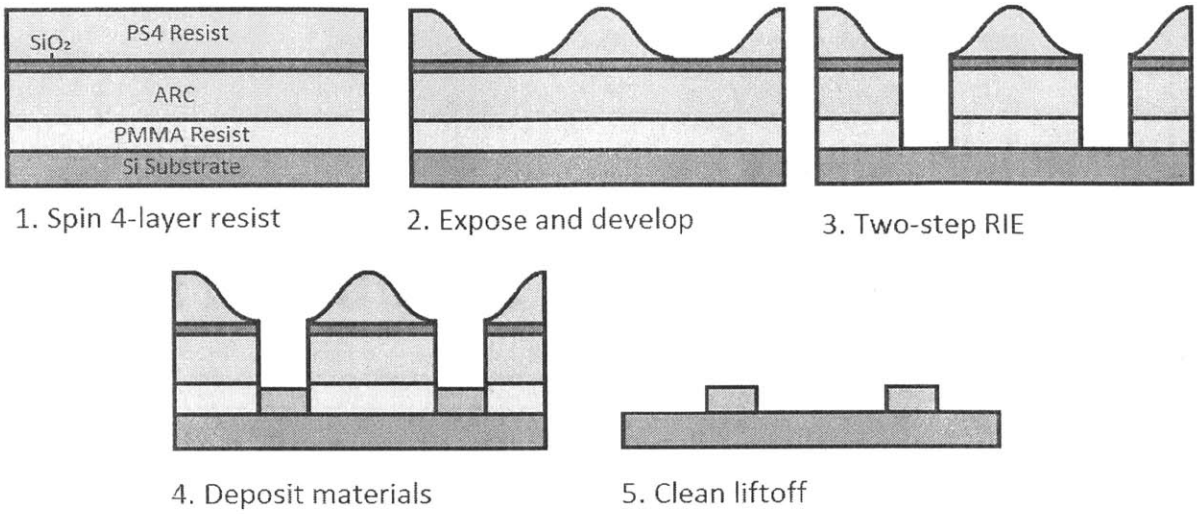

Figure B.1: Schematic of sample fabrication using the modified trilayer resist stack. PMMA dissolves readily during liftoff, unlike ARC.

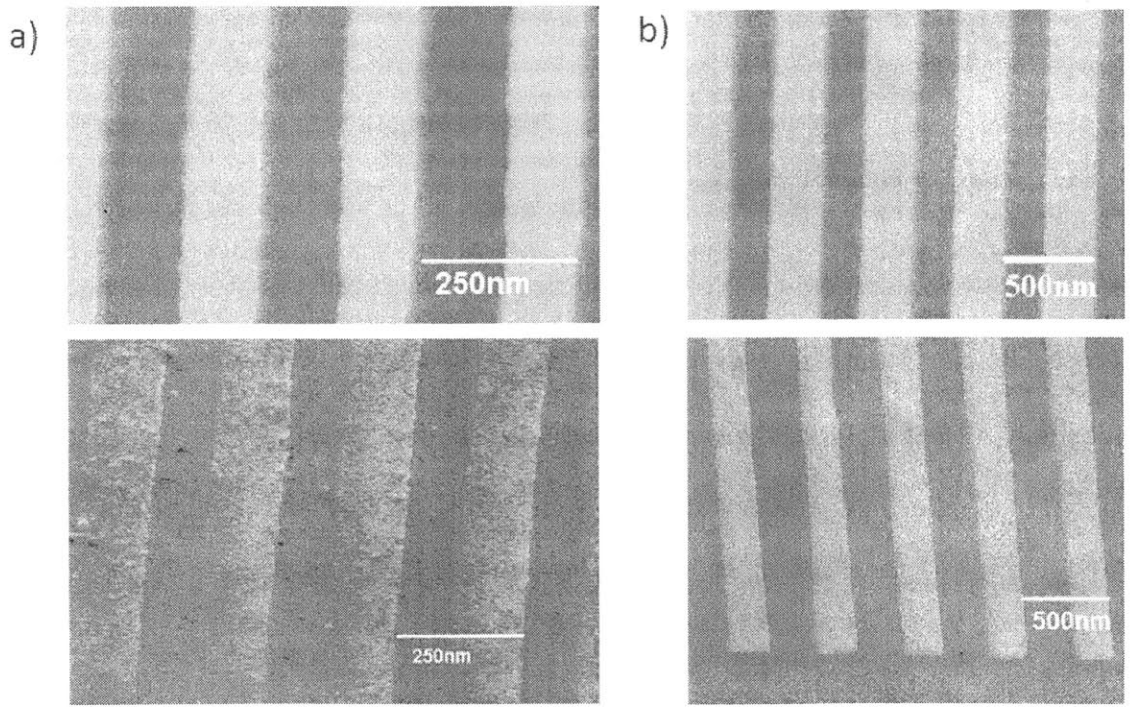

Figure B.2: (a) SEM image of the trilayer resist mask after RIE (top), along with the final sample after liftoff (bottom). (b) SEM image of the quadlayer resist mask after RIE (top), along with the final sample after liftoff (bottom).